REPORT DOCUMENTATION PAGE

Form Approved
OMB No. 0704-0188

PLEASE DO NOT RETURN YOUR FORM TO THE ABOVE ADDRESS.

1. REPORT DATE *(DD-MM-YYYY)*	2. REPORT TYPE	3. DATES COVERED *(From - To)*
27/Jul/2001	DISSERTATION	

4. TITLE AND SUBTITLE
CALIBRATION AND TESTING OF THE 6.5 M MMT ADAPTIVE OPTICS SYSTEM

5a. CONTRACT NUMBER

5b. GRANT NUMBER

5c. PROGRAM ELEMENT NUMBER

6. AUTHOR(S)
MAJ JOHNSON ROBERT L

5d. PROJECT NUMBER

5e. TASK NUMBER

5f. WORK UNIT NUMBER

7. PERFORMING ORGANIZATION NAME(S) AND ADDRESS(ES)
UNIVERSITY OF ARIZONA

8. PERFORMING ORGANIZATION REPORT NUMBER
CI01-214

9. SPONSORING/MONITORING AGENCY NAME(S) AND ADDRESS(ES)
THE DEPARTMENT OF THE AIR FORCE
AFIT/CIA, BLDG 125
2950 P STREET
WPAFB OH 45433

10. SPONSOR/MONITOR'S ACRONYM(S)

11. SPONSOR/MONITOR'S REPORT NUMBER(S)

12. DISTRIBUTION/AVAILABILITY STATEMENT
Unlimited distribution
In Accordance With AFI 35-205/AFIT Sup 1

13. SUPPLEMENTARY NOTES

14. ABSTRACT

15. SUBJECT TERMS

16. SECURITY CLASSIFICATION OF:			17. LIMITATION OF ABSTRACT	18. NUMBER OF PAGES	19a. NAME OF RESPONSIBLE PERSON
a. REPORT	b. ABSTRACT	c. THIS PAGE		210	19b. TELEPHONE NUMBER *(Include area code)*

CALIBRATION AND TESTING
OF THE
6.5 M MMT ADAPTIVE OPTICS SYSTEM

by

Robert Lee Johnson

A Dissertation Submitted to the Faculty of the

COMMITTEE ON OPTICAL SCIENCES (GRADUATE)

In Partial Fulfillment of the Requirements
For the Degree of

DOCTOR OF PHILOSOPHY

In the Graduate College

THE UNIVERSITY OF ARIZONA

2001

Statement by the Author

This dissertation has been submitted in partial fulfillment of requirements for an advanced degree at The University of Arizona and is deposited in the University Library to be made available to borrowers under rules of the Library.

Brief quotations from this dissertation are allowable without special permission, provided that accurate acknowledgment of source is made. Requests for permission for extended quotation from or reproduction of this manuscript in whole or in part may be granted by the head of the major department or the Dean of the Graduate College when in his or her judgment the proposed use of the material is in the interests of scholarship. In all other instances, however, permission must be obtained from the author.

Signed: _____

ACKNOWLEDGMENTS

In writing this dissertation, I have learned how one's work often depends on the work of others. Now is my opportunity to humbly thank those who have helped me complete this journey.

First, I must thank my family: my mother, who taught me to pay attention to the details, my father, who told me that anything worth doing is worth doing right, and my sister, who always encouraged me to do better. I especially thank Bethany, who makes me want to be better than I really am.

Next, I owe a great debt to my advisors and mentors. My hope is to repay my debt by guiding and encouraging others as my advisors have guided and encouraged me. Professor Roger Angel, you have the imagination and intelligence to solve the problems that others dare not approach. Dr. Buddy Martin, you have the courage and the conviction to confront the challenges and turn dreams into reality. Professor Jim Burge, you lead by flawless example; you care more about your students than they often care about themselves.

Dr. George Angeli, Dr. Rich Allen, Bryan Smith, and Lee Dettmann, thank you all for patiently showing me how to build it right. Dr. Michael Lloyd-Hart and Dr. François Wildi, thank you for your patient encouragement. Dr. Matthew Kenworthy and Dr. Doug Miller, thank you for making sure my attitude was properly adjusted. Guido Brusa and Armando Riccardi, thank you for being such gracious hosts when I visited your beautiful city; thank you also for making the most amazing adaptive mirror on the planet. Dr. Troy Rhoadarmer, Dr. Patrick McGuire, and Roland Sarlot, thank you for allowing me to pick up the work that you started.

I especially must thank the excellent staff of talented technicians and magicians who do the real work. Manny Montoya built the gap sensors and, together with Richard Sosa, built the top-box electronics. Richard Sosa also built the tiny gap sensor detector boards. Mario Rascon did much of the opto-mechanical design and Matt Rademacher built just about everything. I also thank the support personnel, without whom nothing would get done: Didi Lawson, Doris Tucker, Kim Chapman, and Ann Klocko. I sincerely thank my sponsor, the Air Force Institute of Technology, and my program manager, Major Luke Whitney.

Finally, I wish to thank my classmates with whom I often shared optics, lively conversation, and meals: Erin Sabatke, Derek Sabatke, Tom Roberts, Neil Beaudry, Rhonda Morgan, Brian Stamper, and Maud Langlois.

Dedication

To Bethany

Table of Contents

List of Figures

List of Tables

Abstract

This dissertation describes the development, calibration, and testing of the adaptive optics system for the 6.5 m Multiple Mirror Telescope. By employing a deformable secondary mirror, the MMT adaptive optics system uniquely solves several problems typical of astronomical adaptive optics systems. Extra components are eliminated, improving throughput and reducing emissivity. Since the adaptive secondary is integral to the telescope, a corrected beam is presented to any instrument mounted at Cassegrain focus.

The testing of an adaptive mirror, which is large and convex, poses a new and difficult problem. I present a test apparatus that allows complete calibration and operation, in closed-loop, of the entire adaptive optics system in the laboratory. The test apparatus replicates the optical path of the telescope with a wavefront error of less than 500 nm RMS. To simulate atmospheric turbulence, machined acrylic plates are included. A phase-shifting interferometer allows calibration of the Shack-Hartmann wavefront sensor and reconstruction algorithms; comparisons agree to one-third of the root-mean-square wavefront. First, techniques were developed to align the apparatus and measure residual aberration. Then, the wavefront sensor was calibrated by measuring its response to introduced tilt. Lastly, a Fourier wave-optics approach was used to produce a modal wavefront reconstructor.

The adaptive secondary mirror uses electro-magnetic force actuators. Capacitive position sensors are placed at each actuator to permit control of the mirror shape without measuring the reflected wavefront. These sensors have nanometer resolution, but require calibration. To calibrate the sensors, I developed a small optical instrument which measures the thickness of transparent films to an absolute accuracy of 5 nm with a precision of 2 nm. The device has applications far beyond

the scope of this research. Twenty-four of these optical gap sensors have been built to calibrate the 336 capacitive sensors on the adaptive secondary mirror. Mirror displacements measured using gap sensors and a phase-shifting interferometer agree to 2 percent of the displacement. The gap sensors allow for quick and accurate calibration of the capacitive sensors without the difficulty of installing an interferometer on the telescope.

CHAPTER 1

INTRODUCTION

Seeing into darkness is clarity.
Knowing how to bend is strength.
Use your own light and return to the source of the light.
This is called practicing eternity.

Lao-tzu, *Tao Te Ching*

1.1 The Role of Adaptive Optics in Astronomy

Nearly 400 years ago, Galileo pointed a small refracting telescope towards Jupiter and discovered four satellites orbiting the planet. Galileo later used his telescope to observe the varying phase and changing apparent size of Venus. With these two simple observations, the geocentric model of the universe was invalidated. Since then, astronomers have used telescopes to observe the heavens and make discoveries that change our understanding of the universe.

The past decade has seen the development of several large optical astronomical telescopes greater than 5 m in diameter. Astronomers build larger telescopes to collect more light and to improve angular resolution. Increasing the aperture diameter increases the light intensity and, ideally, increases the detail in images. Unfortunately, the angular resolution of these large telescopes is limited not by the

(a) (b)

Figure 1.1 Simulated images of stars for a 6.5 m diameter telescope at 1.62 μm wavelength. (a) Image for a perfect telescope with no atmospheric turbulence. The angular diameter is about 0.13 arcsec for this diffraction limited image. (b) Short exposure image of a star degraded by a laboratory simulation of atmospheric turbulence. The coherence length, r_0, is about 11 cm at 0.5 μm wavelength or 44 cm at 1.62 μm wavelength. This image was created using a measurement of a real wavefront which was generated with artificial turbulence in the laboratory.

diameter of their primary mirrors, but by turbulence in earth's atmosphere. Solar heating and winds cause variations in the temperature and hence the density of the air. This, combined with turbulence, causes random fluctuations in the refractive index; thus, the phase of light waves from celestial objects is disturbed.[1] The image formed in the focal plane of the telescope can be many times larger than the image size imposed by diffraction alone. This effect is illustrated in Figure 1.1, where simulated star images for a 6.5 m telescope are shown. The image on the left simulates a perfect telescope in the absence of optical aberrations and atmospheric turbulence. The image on the right is degraded by simulated atmospheric turbulence.

One solution to this problem is to put the telescope above the distorting effects

of earth's atmosphere. Indeed, it has been a common practice for over a century to place telescopes on mountain tops in hopes of improving the seeing. This is only a partial solution, for even at the best sites the angular resolution of a large telescope at visible wavelengths is typically 0.5 arc-seconds. This is equivalent to the diffraction-limited resolution of a 20 cm optical telescope. A complete solution can be had by positioning the telescope totally above the atmosphere, in space. Obviously, placing a telescope in space increases greatly the cost and complexity over ground-based telescopes. Furthermore, current launch technology limits the size, thus, the angular resolution, of space-based telescopes.

Several post-detection processing techniques exist for improving the resolution of images degraded by atmospheric turbulence.[2] These methods involve estimating, through various means, the point-spread function of the combined atmosphere and telescope. An estimate of the original object is then reconstructed through deconvolution. A problem common to these methods is they use short-exposure images with low signal-to-noise ratios; therefore, only relatively bright objects can be reconstructed.[3]

The most effective technique for overcoming the problems introduced by atmospheric turbulence employs adaptive optics. In an adaptive optics system, wavefront distortions are measured using light from a reference source, either a natural star or a laser beacon. These wavefront distortions are corrected, in real time, by either a flexible or movable mirror, or a refractive optical element whose index can be changed quickly. If the distortions are measured accurately and corrected with sufficient temporal and spatial resolution, the diffraction-limited resolution of the telescope can be nearly restored.

Adaptive optics[†] is more practical and less costly than space telescopes for solv-

[†]The distinction between *adaptive* optics and *active* optics should be made. The purpose of active optics is to correct slowly-varying distortions caused by mechanical and optical imperfections

ing the atmospheric turbulence problem. Large ground-based telescopes equipped with adaptive optics can be built for a tiny fraction of the two-billion dollar cost for the Hubble Space Telescope. Ground-based telescopes are easier to maintain and operate; their instruments are readily upgraded as technology improves. Ground-based telescopes can also be quickly reconfigured and adapted for specialized observations. At wavelengths in the near infrared, ground-based telescopes equipped with adaptive optics can achieve higher resolution while collecting more light than current space-based telescopes. In the shorter wavelength bands adaptive optics offers comparable or better performance at a much reduced cost when compared to space-based telescopes. Adaptive optics can even be used in space telescopes to correct deformation and vibration of optical surfaces, especially the thin, lightweight mirrors planned for future telescopes.

Adaptive optics also has some distinct advantages over post-detection image processing techniques. Post-detection techniques use a large series of short-exposure noisy images to reconstruct the object. In contrast, adaptive optics works in real-time by concentrating light from an unresolved star into a nearly diffraction-limited spot. This improves the ability to discriminate faint objects from the sky background. Furthermore, the utility of adaptive optics is not limited only to imaging. In spectroscopy, the spatial and spectral resolution can be improved because the peak intensity and angular resolution of the image formed at the input of the spectrometer are restored. In multiple-aperture optical interferometry, adaptive optics allows astronomers to obtain high angular resolution and enables the use of nulling interferometry to investigate circum-stellar environments.[4,5]

in the telescope itself. Active optics systems typically operate at bandwidths of less than 1 Hz; adaptive optics systems must operate at bandwidths of 10 Hz to 1 kHz to correct rapidly-changing atmospheric distortions.

1.2 Fundamentals of Adaptive Optics

The concept of improving astronomical images by correcting distortions caused by atmospheric turbulence was first suggested by Horace Babcock in 1953.[6] His initial concept included the main components of an adaptive optics system: a wavefront sensor, a wavefront corrector, and a control system that links the two. These basic components are illustrated in Figure 1.2. The wavefront sensor measures wavefront distortions using light from either the object under study or a reference source. This source can be a nearby bright star, called a *natural guide star*, or it can be generated by a laser searchlight, referred to as a *laser beacon*. The output of the wavefront sensor is passed to a control computer, where the wavefront is reconstructed.[‡] The control computer commands the wavefront corrector to apply the complement of the measured wavefront. The compensated beam is passed to the science instrument. The wavefront corrector is typically a deformable mirror whose surface can be mechanically changed. Because of limited dynamic range in the deformable mirror, many adaptive optics systems use a separate mirror to correct global tilt. Other important components include diagnostic and analysis capabilities and user-interface software.

The wavefront measurement and correction cycle must operate fast enough to track changes in the atmosphere. The atmosphere changes quickly at small spatial scales and slowly at large spatial scales. The spatial scale at which corrections must be applied depends on the strength of the turbulence and the wavelength of the light. Fried introduced a parameter called coherence length, denoted r_0, as a measure of turbulence strength.[7] For turbulence described by the Kolmogorov model, coherence length is the aperture diameter over which the mean-square phase

[‡]Because the reference source produces incoherent light, wavefront sensors do not actually measure optical phase. They measure wavefront gradients, which are used to compute variations in optical path length through the atmosphere.

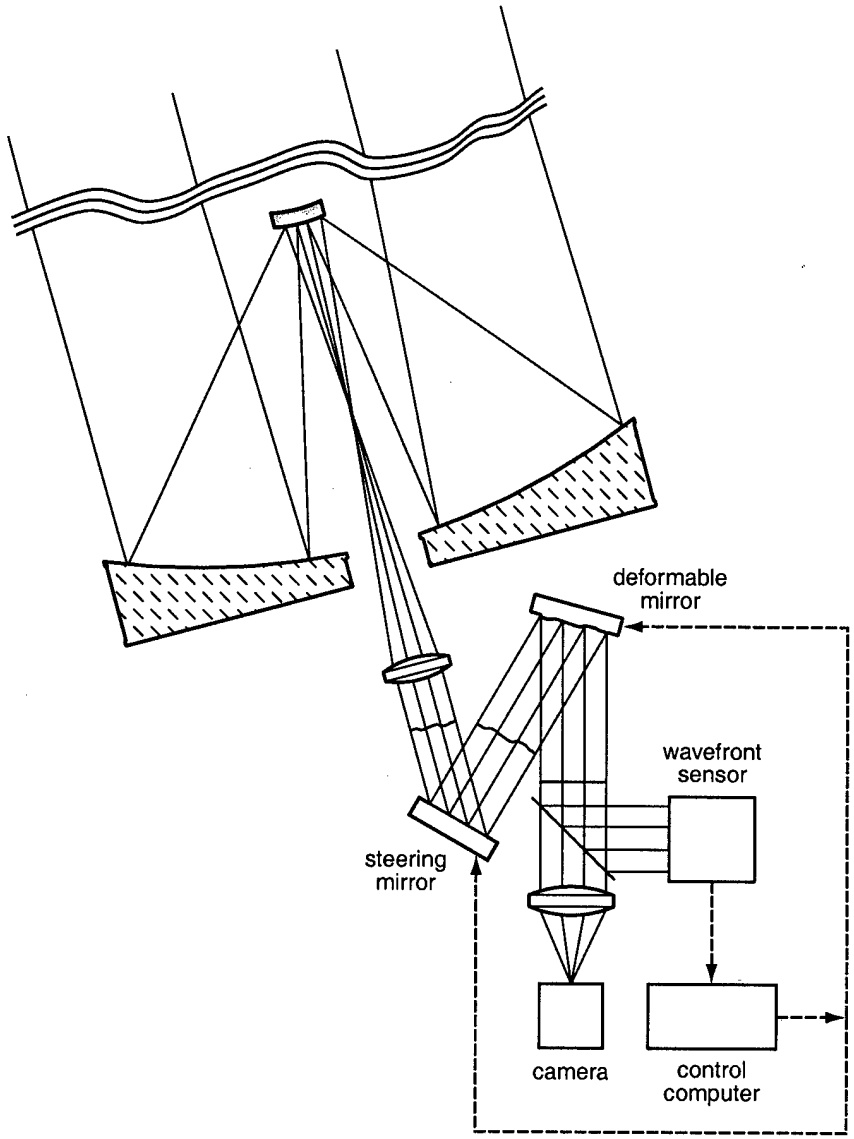

Figure 1.2 Basic components of an adaptive optics system. Light from a distant object is distorted by the atmosphere. The distorted wavefront reflects off a deformable mirror that restores the wavefront shape. It then reflects off a tilt mirror that corrects for overall image motion. The beam is then split with some of the light going to the wavefront sensor and the rest focused onto an imaging camera. A control computer uses the wavefront sensor output to control the deformable mirror and tilt mirror.

error is 1 rad^2. It varies with wavelength λ to the 6/5 power. Typical values of r_0 at 0.5 μm wavelength vary from 5 cm for strong turbulence during the day to 20 cm for good sites at night. An r_0 of 15 cm at 0.5 μm is typical for Mount Hopkins, the site of the 6.5 m Multiple Mirror Telescope (MMT).[8] For the case where the telescope diameter D is greater than r_0, the angular image size is approximately λ/r_0 instead of the diffraction limit λ/D. Greenwood introduced a parameter f_G that characterizes the frequency at which atmospheric turbulence varies.[9] For the simple case of a single layer of turbulence moving at velocity v, the Greenwood frequency is given by

$$f_G = 0.427\, v/r_0. \tag{1.1}$$

For a wind speed of 10 m/s and a coherence length of 10 cm, $f_G \approx 40$ Hz. This gives a rough idea of the closed-loop bandwidth required of the adaptive optics system.

Wavefront sensors for adaptive optics differ from the familiar laser interferometers used in testing optical components in the optical fabrication shop or the laboratory. In these instruments, temporally coherent light from a test wavefront is usually combined with a reference wavefront. This converts the test wavefront into an intensity map, called an interferogram, which is a direct measurement of the wavefront displacement. In contrast, wavefront sensors for adaptive optics must measure the wavefront by using light from a single reference source, either a guide star or laser beacon. They do this by measuring the average wavefront gradient or curvature over small areas covering the telescope pupil. These small areas are called subapertures. The gradients must then be integrated to reconstruct the optical path variations over the entire pupil. Because wavefront measurements must be made quickly and reference sources usually have low brightness, the detectors used in wavefront sensors must have high quantum efficiency and low noise. Three basic types of wavefront sensor have found practical use in adaptive optics: Shack-

Hartmann, shearing interferometer, and curvature sensor.[3] In the most common, the Shack-Hartmann, an array of small lenslets is placed at an image of the telescope pupil.[10] Each lenslet forms an image of the reference source. The position of the image depends on the average wavefront gradient over the lenslet. A detector array in the focal plane of the lenslets measures image positions, which are passed to the processor that reconstructs the wavefront. The lenslets are usually sized to match r_0 on the sky at the desired wavelength of correction.

All wavefront sensors require a reference source to measure optical path variations. There are two requirements for a suitable reference source: high brightness and small angular extent. Bright reference sources provide enough photons to measure wavefront gradients with relatively low noise. Additionally, the reference source should be smaller than the isoplanatic angle, θ_0, the angle over which the change in wavefront error over a large aperture has a variance of 1 rad^2. Also called the isoplanatic patch, θ_0 defines the angular field over which good adaptive correction can be obtained with a single reference star. This limitation is called angular anisoplanatism. For a single turbulent layer, θ_0 can be related to r_0 through the mean height $\bar{h}$ and the zenith angle ζ

$$\theta_0 = 0.314\,(\cos\zeta)\,r_0/\bar{h}. \tag{1.2}$$

The first adaptive optics systems used the objects themselves, solar illuminated satellites, as the reference source. In astronomy, however, the objects of interest are often faint extended sources. Usually, there is no natural star within an isoplanatic patch to act as a reference source. One solution to this problem is to use a laser beacon.

There are two types of laser beacons: Rayleigh scattering from molecules in the air and resonant scattering from sodium atoms in the mesosphere. Rayleigh scattering efficiency decreases with the fourth power of wavelength, λ^{-4}, and is

proportional to air density; thus, lasers with $\lambda < 0.6\,\mu$m are used low in the atmosphere, typically between 8 and 15 km above the ground. Sodium beacons are much higher in the atmosphere, since the density of mesospheric sodium atoms is greatest around 92 km altitude. The scattering mechanism is resonant fluorescence, which is more efficient than Rayleigh scattering at higher altitudes. Unfortunately, lasers that can excite the 589 nm sodium D_2 transition are not commercially available, are expensive, and are difficult to operate and maintain. Laser beacons solve only part of the reference source problem. The position of the laser beacon changes because turbulence introduces tilt to the outgoing laser beam. Thus, a natural guide star is required to correct global tilt; it must be relatively close, in angle, to the science object. Another difficulty with laser beacons is they produce a cone-shaped beam that does not sample all of the turbulent atmosphere above the telescope. The light scattered from the beacon traverses a slightly different path than light from the science object. This cone effect, called focus anisoplanatism, is worse with low-altitude Rayleigh beacons than with high-altitude sodium beacons. Using an array of multiple laser beacons may overcome this problem.[11]

Once atmospheric path distortions have been measured, they must be corrected. Since much of the wavefront correction is tilt over the entire pupil, a dedicated tilt mirror is often used. A separate optical element, with smaller dynamic range, is used to apply higher-order corrections. Two types have been used: deformable mirrors and liquid crystal correctors. By varying an applied electric field, liquid crystals can change the optical path length. Liquid crystal correctors have no moving parts and can have high spatial resolution; however, they have a slow response time and exhibit spectral dispersion. Deformable mirrors can be either segmented or continuous. Segmented mirrors consist of an array small plates, each controlled separately. The space between the segments cause diffraction and light loss; thus,

continuous faceplate mirrors are usually preferred. They consist of a thin glass sheet with push-pull actuators mounted on a rigid baseplate. Other designs include actuators, called bimorph actuators, that apply a bending moment. Actuators can be placed into two groups: displacement actuators apply a displacement that is independent of reaction forces; force actuators apply a force that is independent of displacement. Piezoelectric actuators are an example of displacement actuators; electromagnetic voice-coil actuators are an example of force actuators.

The demands placed upon an astronomical adaptive optics system by the quickly-changing atmosphere require sophisticated electro-optical and mechanical devices be developed. High-speed computers are required to control these devices. Fortunately, many of the required components and control systems have been the subject of military research efforts over many years.[12,13] Many of the requirements of adaptive optics systems that could be used for military surveillance and laser beam control coincide with the requirements of astronomical applications. The significant investment made by the defense community has been used to benefit astronomy and augment the limited budgets available to develop astronomical instruments.

1.3 Adaptive Secondary Mirror for the 6.5 m MMT

The adaptive optics system being developed for the 6.5 m MMT is unique because it employs a deformable secondary mirror of high dynamic range, as is shown in Figure 1.3. This solves several problems common to typical astronomical adaptive optics systems. First, by using an existing optical element, the extra components usually required to implement an adaptive optics system are eliminated. The only modification to the imaging path is a dichroic coating on the window to the camera dewar. Having fewer optical elements improves light throughput and reduces thermal emissivity for infrared observations; this improves the imaging of faint objects.

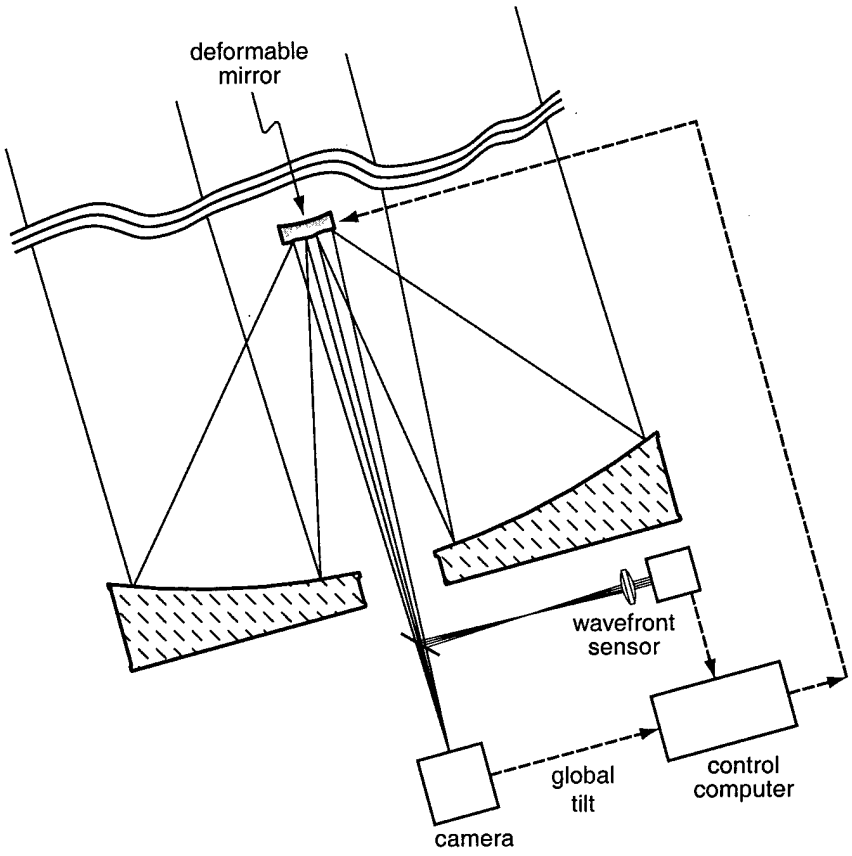

Figure 1.3 Basic components of the 6.5 m MMT adaptive optics system. The secondary mirror is the wavefront corrector. The infrared imaging camera is mounted at the Cassegrain focus. Its dewar window has a dichroic coating that reflects visible light to the wavefront sensor; infrared light is transmitted to the imaging camera. The global tilt sensor shares the infrared camera dewar.

Since the adaptive secondary mirror is an integral part of the telescope, a largely corrected beam is presented to any instrument mounted at the Cassegrain focus.

Adaptive secondary mirrors, however, pose some unique challenges. Secondary mirrors are large and curved, while standard deformable mirrors are small and flat, making the former more difficult to fabricate. The Steward Observatory Mirror Laboratory has developed techniques to accurately fabricate the thin curved aspheric faceplates required for adaptive secondary mirrors.[14,15] Adaptive secondary mir-

rors could insert considerable heat in the optical path. This heat must be removed to avoid introducing additional turbulence. Furthermore, for infrared astronomy, all of the additional components of an adaptive secondary must lie behind the secondary or its support structure, to avoid thermal emission within the telescope pupil.

The MMT adaptive secondary mirror uses electro-magnetic force actuators. Capacitive position sensors have been placed at each force actuator, to allow local control of the actuator position. Actuator position is referenced to a precisely-polished glass surface. The position sensors allow the shape of the mirror to be controlled without measuring the reflected wavefront; thus, the secondary can be set to a fixed, known shape and used for observations without requiring operation of the entire adaptive optics system.

The testing of convex secondary mirrors presents a difficult challenge. To overcome this, I use a test system which replicates the optical path of the 6.5 m MMT. It consists of a full-size doublet lens mounted directly in front of the secondary mirror to refract light rays normal to the mirror surface in a Littrow-like test setting. An computer generated hologram is used to compensate the spherical aberration from the doublet and the hyperbolic secondary. An $f/15$ focus is formed to mimic that of the telescope. This test apparatus allows calibration and operation of the entire adaptive optics system, except for the laser beacon, in the laboratory.

The 6.5 m MMT adaptive optics system uses a Shack-Hartmann wavefront sensor in visible light, while infrared light is available for imaging. This is possible because the spectral dispersion of air is very small between the visible and near infrared; therefore, optical path length variations in the atmosphere are practically independent of wavelength. Imaging in the infrared has several advantages. As wavelength increases, a given variation in optical path length corresponds to a smaller change in phase. This means atmospheric turbulence degrades infrared images less; adaptive

optics systems can be more effective.

The MMT adaptive optics system senses global tilt using infrared light from a natural guide star. In infrared light, the corrected image of the guide star is sharper than in visible light. The smaller infrared image improves the accuracy of the centroid measurement, thus the error in the global tilt measurement is decreased. The smaller infrared image means fainter stars can be used for tilt measurement. Furthermore, since the isoplanatic angle increases as $\lambda^{6/5}$, the guide star can be farther away from the science object, opening more of the sky to adaptive correction.

1.4 Calibrating and Testing the 6.5 m MMT Adaptive Optics System

This dissertation describes my work at the Steward Observatory in the developing, calibrating, and testing parts of the adaptive optics system for the 6.5 m MMT. Clearly, developing a new adaptive optics system of this complexity takes the efforts of many people, who face numerous unique challenges. I endeavor here to present my solutions to several tasks which others may encounter in pursuing similar work.

I first describe my efforts in designing, building, and aligning optical components associated with the wavefront sensor in Chapter 2. As an introduction to my work calibrating and developing diagnostic tools for the wavefront sensor, Chapter 3 discusses alignment and analysis of the apparatus used to test the adaptive optics system in the laboratory. This test system replicates the optical path of the 6.5 m MMT with a root-mean-square wavefront error of less than 450 nm. In Chapter 4, I discuss test procedures and results which compare wavefront sensor measurements to independent measurements made with a phase-shifting interferometer. These measurements will allow the calibration and testing of the wavefront sensor hardware and the wavefront reconstructor in the presence of simulated turbulence in the

laboratory. Comparison of the wavefronts measured by the two methods agree to about one-third of the root-mean-square wavefront error in the system.

In Chapter 5, I present my work in developing a small optical instrument, called a gap sensor, that allows *in situ* calibration of the capacitive position sensors used in the adaptive secondary mirror. The gap sensor measures the absolute distance between the thin mirror faceplate and the thick glass reference surface with an accuracy of a few nm and a repeatability of less than 1 nm. These gap sensors may prove useful in any application that requires an accurate measurement of a thin transparent film.

Chapter 6 discusses the manufacture of the 24 gap sensors and associated components which will be used with the adaptive secondary. Chapter 6 also describes the steps taken to fine-tune the gap sensor analysis algorithms and procedures. I also present tests to calibrate the capacitive sensors on a prototype of the adaptive secondary mirror. Small displacements of the mirror surface were measured using the gap sensors and a phase-shifting interferometer. The measurements agree to better than 2 percent of the displacement.

Chapter 2

The 6.5 m MMT Adaptive Optics System

2.1 Introduction

This chapter presents an overview of the 6.5 m MMT adaptive optics system. Particular attention is given to those components used in measuring wavefronts: the pupil relay optics and the wavefront sensor. Alignment and testing of the laboratory adaptive optics test system, the *shimulator*, are discussed in Chapter 3. The 6.5 m MMT adaptive optics system is unique in that it employs an adaptive secondary mirror. By using an existing optical element as the deformable surface, many of the extra components usually required to implement an adaptive optics system are eliminated. Having fewer optical elements improves light throughput and reduces the total thermal emissivity of the optical path. This improves performance, especially for infrared observations; integration times are much shorter and fainter objects can be imaged.[16] The adaptive optics system has been an integral part of the 6.5 m MMT, rather than a separate system to be added later, since its early design. Since the adaptive secondary is an integral part of the telescope, a largely

corrected beam is presented to any instrument mounted at the Cassegrain focus without reconfiguring the adaptive optics system.

This chapter describes the design, assembly, and alignment of the components that compose the wavefront sensing portion of the adaptive optics system. Since much of the preliminary design work had been completed, my task was to verify and refine the optical design of the wavefront sensing components. I then assembled, aligned, and evaluated the optical parts of the system. The following sections describe that work. First, mechanical structures and their assembly are explored in Section 2.2. Next, Section 2.3 describes the procedures I followed in refining and implementing the optical design. The design and assembly of some parts of the Shack-Hartmann wavefront sensor are briefly presented in Section 2.5. Finally, the system imaging performance is evaluated in Section 2.6.

2.2 Top-Box Mechanical Components

A 1.8 m diameter structure called the *top-box* contains the wavefront sensor and visible-light detector arrays. To maintain the orientation of instruments to the sky as the telescope follows the stars, an instrument derotator is provided at the Cassegrain focus of the telescope. The top-box is attached to this instrument derotator flange as illustrated in Figure 2.1. To maintain the relationship between the wavefront sensor and the deformable secondary mirror, the wavefront sensor is mounted in a rotational stage which counters the motion of the instrument derotator. Infrared detectors and science instruments mount to the underside of the top-box. The top-box itself consists of a octagonal optics bed at the bottom and a ring-shaped flange at the top. The upper surface of the optics bed, to which the top-box optical elements attach, lies 381 mm (15 inches) below the mounting flange of the instrument derotator. Eight upright posts attach the optics bed to the flange at the corners

(a)

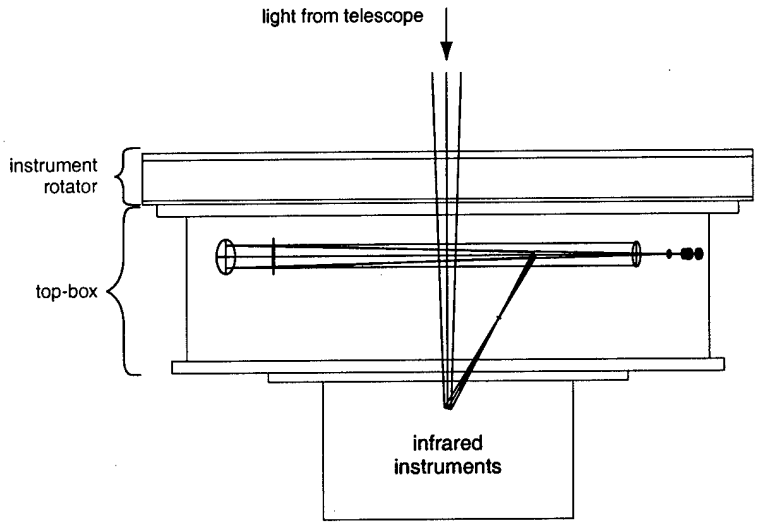

(b)

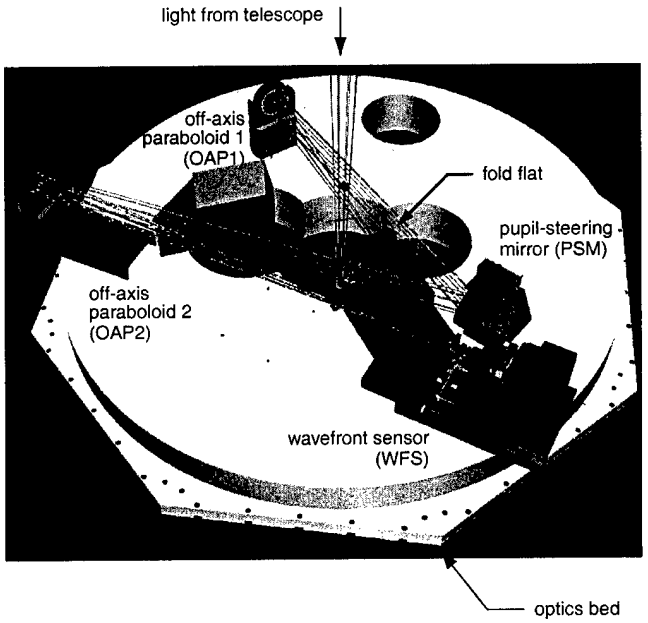

Figure 2.1 Drawing of the top-box mounted to the instrument derotator. Figure (a) is a side view showing the optical path for visible light. The wavefront sensor and visible-light detectors are contained in the top-box; infrared instruments mount to the underside of the top-box. Figure (b) is a view inside the top-box showing the optics bed, mirror mounts, and wavefront sensor.

of the octagon. Panels fill the spaces between the uprights. To give access to the top-box interior, large cutouts were made in the panels. All the components were machined from aluminum; they were attached to one another with steel bolts.

The 100 mm thick optics bed is a single casting from aluminum. Integral support structures were manufactured into the bed to minimize flexure as the telescope rotates in elevation. After the optics bed was cast, the upper mounting surfaces and outer edges were machined. The pupil imaging optics consist of four mirrors held in commercial gimbal mounts. The gimbal mounts were attached to interface plates which were then bolted to the optics bed. The interface plates raise the mirrors to the same height above the optics bed and constrain their translational position. The gimbal mounts allow the mirrors to tip and tilt, but do not allow other motion.

Except for the wavefront sensor, the translational positions of the top-box optics are determined solely by mechanical constraints. That is, no provision was made for adjusting the translational position of the mirrors after the top-box was assembled. Only the tip and tilt of the mirrors can be adjusted; thus, the mirror mounts had to be accurately attached to the optics bed. Since the top-box optical design was modified after the optics bed was manufactured, the bolt holes for the optical mounts were slightly misplaced in the optics bed. To compensate, interface plates were used to locate the optics within the tolerances of the optical design. These are the steps followed:

1. coordinates of bolt holes in optics bed were measured,
2. hole coordinates were merged with optical layout,
3. interface plates were designed and fabricated,
4. mirrors were installed in gimbal mounts,
5. gimbal mounts were attached to interface plates,
6. interface plates were positioned on optics bed using shoulder bolts.

component	precision (mm)
holes in optics bed	0.20
interface plates	0.13
mirror mounts	0.25
shoulder bolts	0.05
total	0.35

Table 2.1 Accuracy of placement of top-box optical elements. The total accuracy was estimated using the root-sum-square.

First, the hole positions in the optics bed were carefully measured to an accuracy of about 200 μm.[17] Using a computer-aided design program, the hole coordinates were then merged with the mirror coordinates from the optical design. The development of the optical design is described in Section 2.3. The interface plates were designed so the mirrors were positioned correctly, even though the bolt holes were misplaced. Next, each mirror was inserted in its gimbal mount so its optical axis intersected the gimbal axes at the mirror surface. This way, when the mirror is tilted, its optical axis is not translated relative to the axis of the incoming beam. Each gimbal mount was fastened to its interface plate. The mirror position was carefully measured and adjusted, relative to the interface plate bolt holes, to comply with the computer design. Finally, the interface plates were attached to the optics bed using shoulder bolts. The shoulder bolts and interface plate holes were manufactured to precise tolerances so the movement between the two is negligible. Table 2.1 lists the precision in each of the components which, in turn, contribute to the accuracy in positioning the top-box optics. I estimate the overall accuracy to be ± 0.35 mm.

2.3 Top-Box Optical Layout

In this section, I discuss the layout of the top-box optics. Although the design includes provisions for upgrades to the adaptive optics system and the addition of various science instruments, only the optics required for basic operations are presented here. For a brief overview of these additional instruments, I encourage the interested reader to consult M. Lloyd-Hart's paper.[18] The original 13×13 subaperture wavefront sensor design was modified to accommodate 12×12 subapertures.† This prompted changes to the original top-box optical design. In updating the top-box optical design, I followed the original design philosophy of J. C. Shelton, which is outlined below.[19]

Figure 2.2 shows an overview of the top-box optical layout. Only the components required for basic operation of the wavefront sensor are shown. Drawings of the optical path are shown in Figure 2.3; the dotted lines illustrate rays from the reference source, either a natural star or a laser beacon. In describing the top-box optical path, I define a local coordinate system where the light propagates along the z-axis and the x-axis is parallel to the plane of the optics bed.

The $f/15$ beam from the telescope enters the top-box from above. Before the light comes to a focus, it encounters a dichroic beamsplitter which transmits infrared light and reflects visible light, that is, wavelengths less than 1 μm. The beamsplitter is the dewar window of the primary science instrument, the Arizona Infrared Imager and Echelle Spectrograph or ARIES. Inside the ARIES dewar, a portion of the infrared light is picked-off by a small mirror and re-imaged onto a global tilt sensor. This tilt sensor is used only in the laser beacon mode. The pick-off mirror can be steered over a 1 arcmin radius field to select the natural star used for measuring global tilt.

†In the 13×13 subaperture configuration, the central rows and columns of detector sub-arrays are divided between different amplifiers. The amplifiers have slightly different gains, causing large offsets in the centroid measurements from the central subapertures.

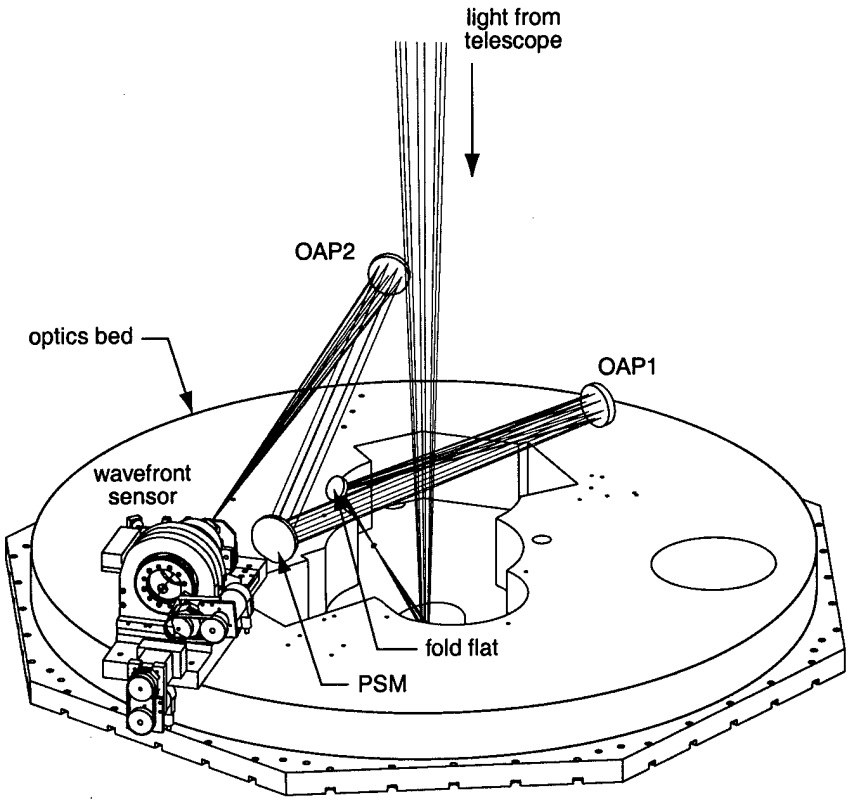

Figure 2.2 Basic top-box optical layout. Only the optical elements required for operation of the wavefront sensor are shown; the gimbal mounts have been omitted. Light from the telescope enters the top-box from above, reflects from the dichroic beamsplitter, and goes through the $f/15$ focus. It is then folded into the plane of the optics bed, collimated by OAP1, reflected by the pupil-steering mirror, and focused by OAP2 into the wavefront sensor.

(a)

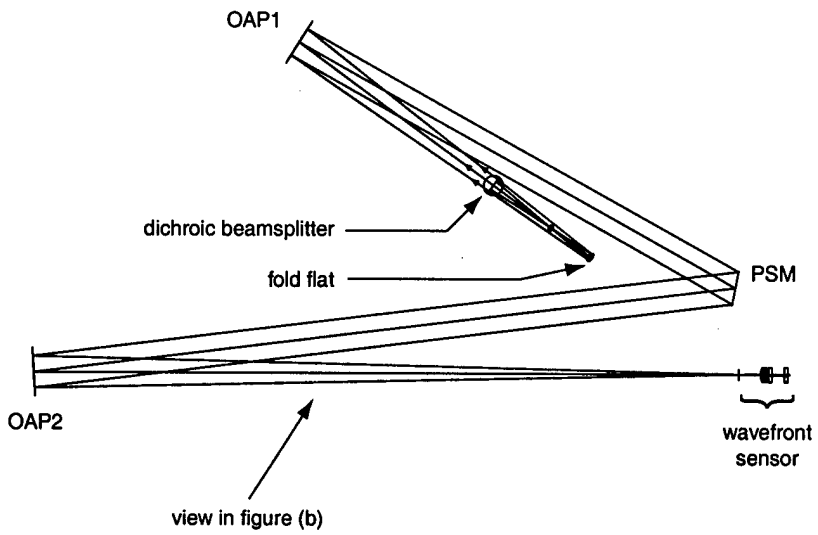

(b)

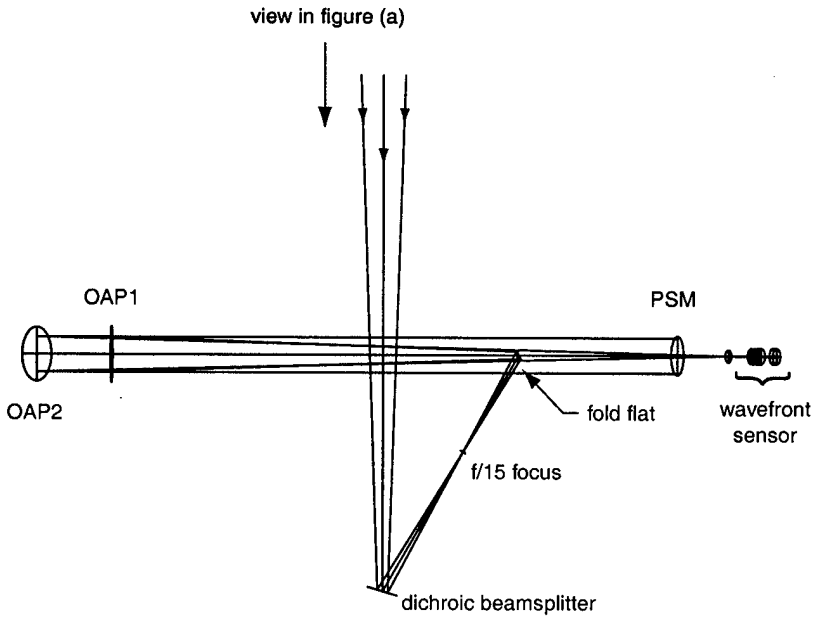

Figure 2.3 Basic top-box optical path. The rays depict light from a natural guide star. Figure (a) is a top view, looking down from the telescope; Figure (b) is a side view, looking through the sides of the top-box. The large arrow in one figure indicates the view angle for the other figure.

Visible light from the reference star is reflected upward from the dichroic beamsplitter at a 30 degree angle to the incoming beam. The light rays go through the $f/15$ focus and reflect at a 60 degree angle, from a small fold mirror, into the plane of the optics bed. The light is then collimated by an off-axis paraboloid, called OAP1, and sent to a steering mirror. OAP1 forms a real image of the entrance pupil, the secondary mirror, on the steering mirror; hence, it is called the pupil-steering mirror, or PSM.[‡] Since the PSM lies at an image of the entrance pupil, it can introduce pure tilt to the wavefront without causing the exit pupil to move. The pupil-steering mirror is used to center the natural guide star in the field of the wavefront sensor while the telescope is pointed at the science object. In laser beacon mode, the PSM is used to steer an image of the laser beacon onto a field stop in front of the wavefront sensor. The field stop is used to block laser light, scattered from lower in the atmosphere, from entering the wavefront sensor. The tip and tilt of the PSM is driven by precision linear actuators with relative position feedback.[20]

Collimated light is reflected from the PSM and is focused by a second off-axis paraboloid, OAP2, to a point in front of the wavefront sensor. OAP2 relays the intermediate image of the pupil, formed by OAP1 at the PSM, to infinity. A detailed view of the beam path near the wavefront sensor is shown in Figure 2.4. An achromatic doublet lens, mounted at the front of the wavefront sensor, collimates the light from the reference source. The collimating doublet forms an image of the pupil, which was relayed to infinity by OAP2, on the wavefront sensor lenslet array. The lenslet array forms an array of images of the reference source on the detector array. The lenslet array divides the pupil into subapertures. The wavefront slope over each subaperture is measured by observing the displacement of images of the reference star on the detector array. A calcium fluoride window sits between the collimating

[‡]Since the pupil-steering mirror does not actually steer the pupil, this is a misnomer.

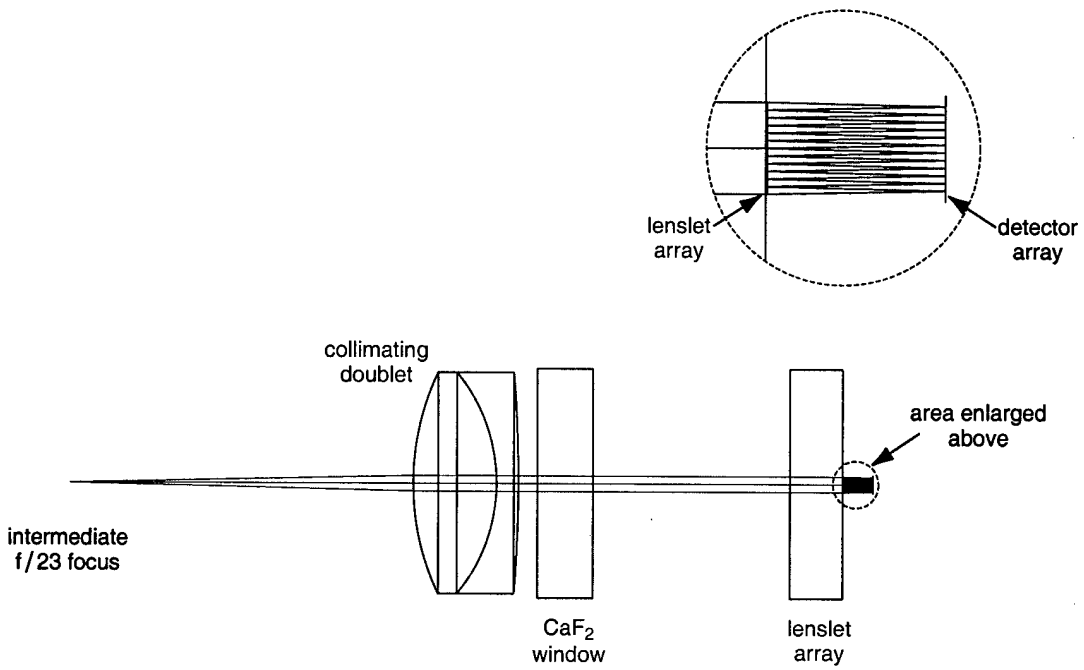

Figure 2.4 Wavefront sensor optical path. The rays depict light from the reference source diverging from the intermediate focus. The individual lenslets are omitted for clarity.

lens and the lenslet array to maintain the vacuum inside the dewar.

Note that the location of the intermediate focus in front of the wavefront sensor changes, along the z-axis, depending on the distance to the reference source. In sodium laser beacon mode, the focus is about 300 mm behind the focus for natural guide star mode. To compensate, the wavefront sensor translates along the z-axis so the doublet still collimates light from the laser beacon. Recall, the collimating doublet forms an image of the pupil on the wavefront sensor lenslet array. Since the pupil is imaged to infinity by OAP2, the collimating doublet images the pupil onto the lenslet array regardless of the wavefront sensor position along the z-axis. Thus, as the wavefront sensor is refocused, the pupil imaging onto the lenslet array remains correct.

2.4 Top-Box Optical Design

2.4.1 Top-Box First-Order Optical Design

Table 2.2 reviews the function of each top-box optical element in imaging the reference source. The table also includes imaging of the telescope pupil, that is, the secondary mirror, through the top-box. Because the initial top-box optical design failed to image the telescope pupil onto the steering mirror, I modified the optical design before assembling the top-box. Given the functions listed in Table 2.2 and the prescription for the telescope, I completed a first-order or paraxial optical design. A first-order design considers only the power and vertex separation of the elements. This preliminary design was then refined by calculating the optimum angle of the off-axis paraboloids to minimize third-order aberrations. Fold mirrors were then inserted and the design was finalized using optical analysis software. The sign conventions used in the analysis to follow are those adopted by Smith.[21] Table 2.3 lists the specifications of the 6.5 m MMT and the two off-axis paraboloids. The conic constant of the secondary is -1.409 and the separation between the primary and the secondary is 7307.5 mm.[22,23]

The first-order design for the top-box started with the elements listed in Table 2.3 and displayed in Figure 2.5. To simplify matters, the fold mirror and the dichroic beamsplitter were not considered. To make notation less cumbersome, I chose to label each mirror Mi, where i indicates its order in the beam path. Thus, R_1 is the vertex radius of curvature of M1 and f_1 is its focal length. The distance between M1 and M2 is denoted z_{12} and the index of refraction of the space between M1 and M2 is denoted n_{12}. The basic design used a natural guide star as a reference source; the wavefront sensor would be translated for laser beacon mode. The first step was locating OAP1 (M3) relative to the secondary mirror, M2. We know that OAP1 collimates light from the reference source; therefore, it lies one OAP1 focal

element	reference source imaging	pupil imaging
dichroic beamsplitter	reflects visible light $\lambda < 1$ μm	–
fold mirror	folds beam into plane of optics bed	–
OAP1 (M3)	collimates $f/15$ beam	images pupil onto PSM
PSM (M4)	offset point to put reference on WFS	–
OAP2 (M5)	focuses beam at $f/23$	images pupil to infinity
collimating lens (L1)	collimates $f/23$ beam	images pupil onto lenslets
lenslet array (L2)	focuses reference onto detector array	–

Table 2.2 Summary of top-box optical element functions. The effects of the elements in imaging the reference source and pupil are listed. Images of the pupil are formed at the PSM and the lenslet array. OAP = off-axis paraboloid, PSM = pupil-steering mirror.

element	curvature (mm)	diameter (mm)	off-axis (mm)
primary (M1)	16256.0	6502.0	0
secondary (M2)	−1794.5	642.5	0
OAP1 (M3)	1656.8	88.9	101.1
OAP2 (M5)	2538.8	85.0	151.2

Table 2.3 Prescription of optical elements.[22,23] The *curvature* is the vertex radius of curvature (denoted R_i), *off-axis* is the distance from the vertex of the parent paraboloid to the center of the segment. The conic constant of the hyperboloid secondary is −1.409; the other elements are paraboloids with a conic constant of −1.0. The separation between the primary and the secondary is nominally 7307.5 mm.

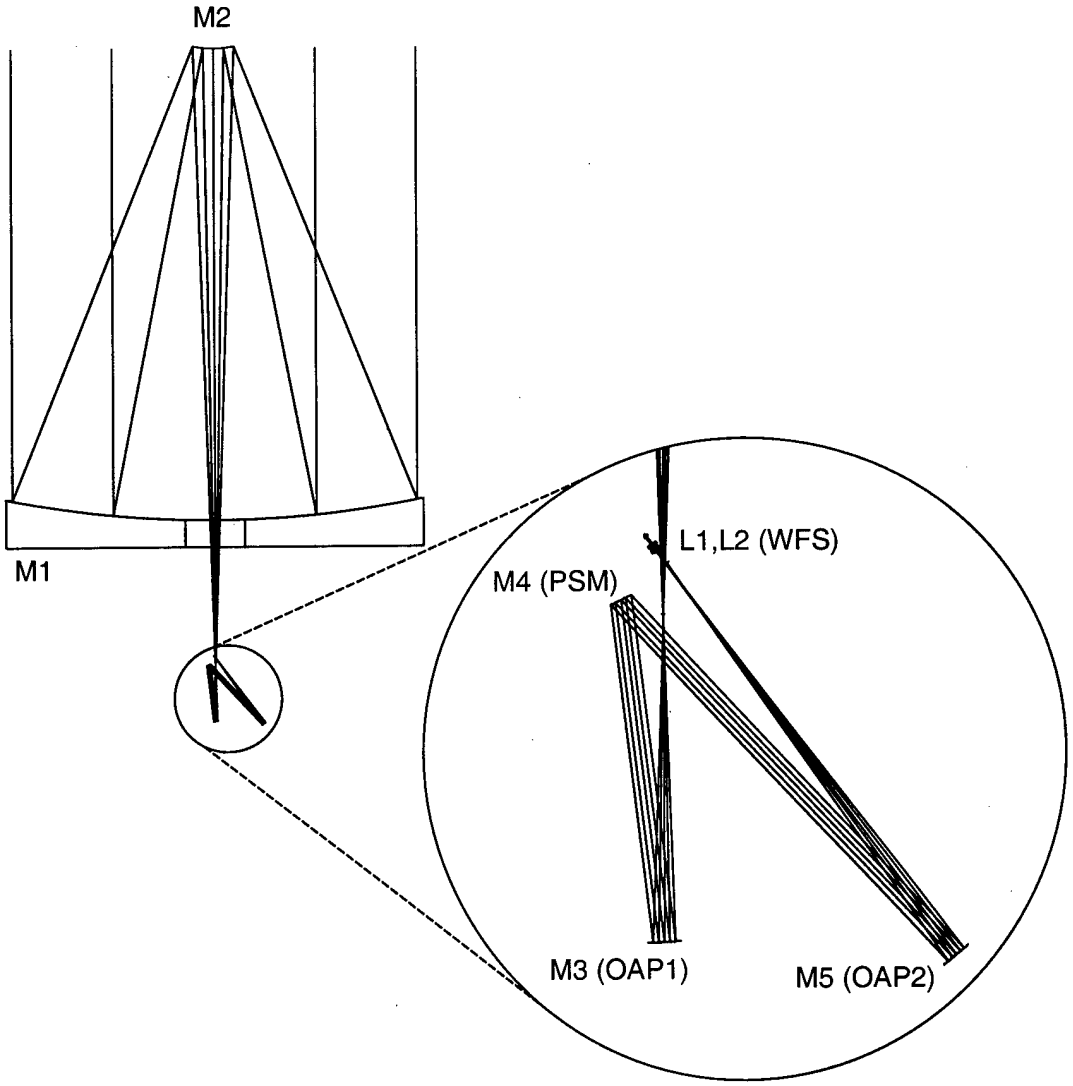

Figure 2.5 Optical elements considered in the first-order design of the top-box. The dichroic beamsplitter and fold flat have been omitted for simplicity. See Tables 2.2 and 2.3 for a description of each element and its function. M1 is the primary mirror and M2 is the secondary. M3 images M2 onto the pupil-steering mirror, M4. M5 relays the pupil image to infinity; L1 images the pupil onto the lenslet array in the wavefront sensor.

length ($f_3 = 828.4$ mm) from the $f/15$ focus. To find the distance from M2 to the $f/15$ focus, I first calculated the effective focal length, f_e, of the telescope. The f_e is the reciprocal of the effective power, ϕ_e, where

$$\phi_e = \phi_1 + \phi_1 - \phi_2\phi_2\left(\frac{z_{12}}{n_{12}}\right). \tag{2.1}$$

Now, $\phi_1 = -2/R_1$ is the power of M1, $\phi_2 = 2/R_2$ is the power of M2. By convention, the index after a reflection is negative; thus, $n_{12} = -1$ and $z_{12} = -7307.5$ mm, so, $f_e = 94991$ mm. The location of the rear principal plane was given by

$$\delta' = \frac{-\phi_1}{\phi_e}\frac{t_{12}}{n_{12}} = -85401\,\text{mm}. \tag{2.2}$$

The distance from M2 to the $f/15$ focus is $f_b = f_e + \delta' = 9590$ mm and the separation between M2 and OAP1 is $z_{23} = f_b + f_3 = 10418$ mm.

The requirement that the PSM (M4) lie at an image of M2 determined the distance from OAP1 to the PSM, z_{34}. The imaging equation gave this distance

$$z_{34} = n_{34}\left(\frac{1}{f_3} + \frac{n_{23}}{z_{23}}\right)^{-1} \tag{2.3}$$

thus $z_{34} = -900.0$ mm. The diameter of the image of the pupil at the PSM was found by calculating the magnification of OAP1 for an object distance of z_{23}

$$m_{\text{OAP1}} = \frac{z_{34}/n_{34}}{z_{23}/n_{23}} = -0.0864. \tag{2.4}$$

This gave the size of the image of the pupil at the PSM

$$d_{\text{PSM}} = d_{\text{M2}}\, m_{\text{OAP1}} = -55.5\,\text{mm} \tag{2.5}$$

where the negative sign indicates the image is inverted. The requirement that OAP2 (M5) images the pupil to infinity determined the distance from the PSM to OAP2, z_{45}. Thus, OAP2 is positioned one OAP2 focal length ($f_5 = 1269.4$ mm) from the PSM. This also gave the distance between OAP2 and the intermediate focus just

before the wavefront sensor. The light reflected from the PSM is collimated; thus, the reference source is imaged at the rear focus of OAP2.

To complete the first-order design, I determined the focal length of the wavefront sensor collimating lens, L1. The position of L1 was determined by the requirement that it collimates light leaving the intermediate focus. Thus its distance from the intermediate focus is equal to its focal length. The focal length of L1 determines the size of the image of the secondary on the lenslet array. The pitch of the lenslets is 144 μm and there are 12 lenslets across the diameter of the pupil; therefore, the pupil diameter on the lenslet array is $d_{\text{lenslet}} = (12)(144\,\mu\text{m}) = 1.728\,\text{mm}$. The required magnification of the pupil by L1 is

$$m_{\text{L1}} = \frac{d_{\text{lenslet}}}{d_{\text{PSM}}} = 0.0311. \tag{2.6}$$

The magnification is determined by the ratio of the focal lengths of L1 and OAP2. Thus, the focal length of L1 is

$$f_{\text{L1}} = m_{\text{L1}}\, f_5 = 39.5\,\text{mm}. \tag{2.7}$$

The image of the secondary is formed at the rear focus of L1; thus, the lenslet array is placed f_{L1} behind L1. The detector array lies at the rear focal plane, or $f_{\text{lenslet}} = 3.4$ mm behind the lenslet array.

Given the dimensions of the wavefront sensor detector array, the angular sampling of the wavefront sensor on the sky can be determined. The angular magnification of the telescope pupil at the lenslet array, m_{P}, is given by the ratio of the pupil diameters

$$m_{\text{P}} = \frac{d_{\text{M1}}}{d_{\text{lenslet}}} = \frac{6.5\,\text{m}}{1.728 \times 10^{-3}\,\text{m}} = 3761.6. \tag{2.8}$$

The angular field on the sky for each subaperture is found by reducing the angular

field of a subaperture by m_P

$$\alpha_{\text{subap}} = \frac{d_{\text{subap}}}{m_P \cdot f_{\text{lenslet}}} = \frac{0.144\,\text{mm}}{3761.6 \cdot 3.4\,\text{mm}} = 11.26\,\mu\text{rad} = 2.32\,\text{arcsec.} \tag{2.9}$$

Since each subaperture is 6 pixels on a side, the angular sampling on the sky at the wavefront sensor is about 0.4 arcsec.

Having calculated the power and vertex separation of the optical elements, the first-order design was complete. Since paraboloids are used in the top-box, axial imaging of the reference source is free from aberration.[21,24] However, the top-box is required to provide good imaging over a 30 arcsec radius field. In addition, the maximum distortion in the pupil images is limited to 2 mm at the secondary.[25,26] This first-order design did not consider the imaging performance as the field angle is increased. The preliminary design was refined by calculating the optimum angle of the off-axis paraboloids to minimize third-order aberrations. This refinement is discussed in the next section.

2.4.2 Top-Box Third-Order Optical Design

The next task in the design process was to determine the constraints in employing the off-axis paraboloids. The element separations calculated above applied to the vertex of the *parent* paraboloids. The distance to the vertex of the off-axis segment of the parent was required. Consider the geometry of a single parent paraboloid, with focal length f, as shown in Figure 2.6. The off-axis distance ρ is the perpendicular distance from the axis of the parent to the center of the off-axis segment. The off-axis angle α is the angle between the axis of the parent and the axis of the segment measured at the focus. The sagittal height of a paraboloid is $s = \rho^2/2R$ where R is the vertex radius of curvature, given by $R = 2f$. From the drawing, $\tan\alpha = \rho/(f - s)$. Substituting for the sagittal height yields

$$\tan\alpha = \frac{\rho}{f - \rho^2/4f}. \tag{2.10}$$

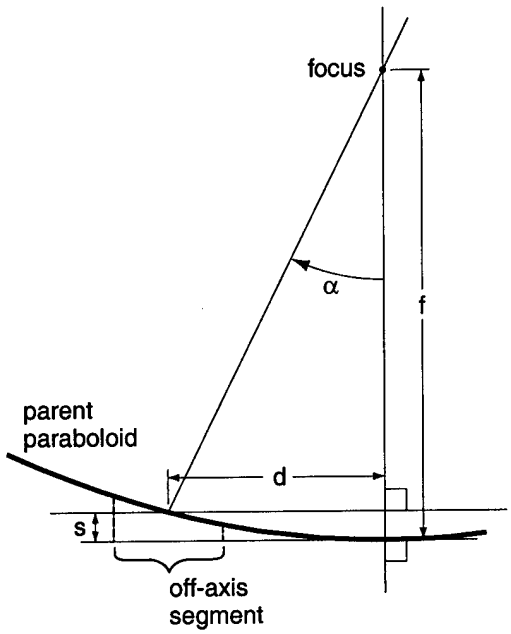

Figure 2.6 Geometry of a parent paraboloid and an off-axis segment. The focal length is f, the off-axis distance is ρ, and the off-axis angle is α. The sagittal height of a paraboloid is $s = \rho^2/2R$ where R is the vertex radius of curvature, given by $R = 2f$.

Substituting the parameters listed in Table 2.3 gives the off-axis angles, which are listed in Table 2.4.

As mentioned in Section 2.3, the pupil-steering mirror is used to center the natural guide star in the field of the wavefront sensor while the telescope is pointed at a nearby science object. When this occurs, the guide star will not be at the center of the field of the first off-axis paraboloid. When a paraboloid is used with zero field angle, the image is perfectly stigmatic; however, as the field angle increases, coma is introduced.[21,24] If two off-axis paraboloids are used to relay a magnified image, field aberrations are minimized when the ratio of their focal lengths is equal to the ratio of their off-axis angles.[19,27] If this condition is met, the third-order coma introduced by the two paraboloids can be made to cancel. For our off-axis paraboloids the ratio of the focal lengths is $f_{\mathrm{OAP2}}/f_{\mathrm{OAP1}} = 1.53$ and the ratio of

element	f, focal length (mm)	ρ, off-axis distance (mm)	s, sagittal height (mm)	α, off-axis angle (deg)
OAP1	828.4	101.1	3.085	6.98
OAP2	1269.4	151.2	4.502	6.82

Table 2.4 Off-axis angles for off-axis paraboloids calculated using Equation (2.10). The sagittal height is the sagittal height of the parent paraboloid at the center of the off-axis segment.

the off-axis angles is $\alpha_{\text{OAP2}}/\alpha_{\text{OAP1}} = 0.98$. Since the condition for minimizing field aberrations is not met, we can expect some coma as the field angle increases.

The initial third-order optical design is listed in Table 2.5. The dichroic beamsplitter and the fold mirror have been inserted. Adjustments have been made to the spacings to account for the sagittal height of the off-axis paraboloids. The spacing between OAP1 and the PSM was increased so that half of the secondary would fall on either side of best focus. These parameters, along with the mirror prescriptions listed in Table 2.3, were entered into an optical design program to model the performance and optimize the placement of the elements. The two measures of performance were pupil distortion and imaging of the reference source. The next section discusses the opto-mechanical design of the wavefront sensor collimating lens; the last section presents the predicted and the measured performance of the top-box.

2.5 Shack-Hartmann Wavefront Sensor Optics

As mentioned in Section 1.2, wavefront sensors estimate wavefront aberrations using either a guide star or laser beacon as a reference source. They measure the average wavefront gradient or curvature over small areas of the telescope pupil called subapertures. The gradients are processed to reconstruct the optical path variations over the entire pupil. In the Shack-Hartmann wavefront sensor, an array of small

element	curvature (mm)	spacing (mm)	angle (deg)
primary (M1)	16256.0	−7307.5	–
secondary (M2)	−1794.5	9335.0	–
beamsplitter(F1)	–	−258.0	15.0 x-axis
$f/15$ focus	–	−177.4	–
fold mirror (F2)	–	654.1	30.0 x-axis
OAP1 (M3)	−1656.8	−906.7	−7.0 y-axis
PSM (M4)	–	1269.4	−18.0 y-axis
OAP2 (M5)	−2538.8	−1273.9	6.8 y-axis
$f/23$ focus	–	−39.5	–

Table 2.5 Initial third-order optical design. The *spacing* is the distance to the next element. The *angle* is the rotation of the element about the axis listed; the x-axis is parallel to the optics bed and the y-axis is perpendicular to the optics bed.

lenslets is placed at an image of the telescope pupil.[10] Each lenslet forms an image of the reference source whose position depends on the average wavefront gradient over the lenslet. A detector array measures the image positions which are passed to the processor that reconstructs the wavefront. The 6.5 m MMT Shack-Hartmann wavefront sensor is unique in that the lenslet array is bonded directly to the detector package. This eliminates the need to realign the lenslet array to the detector array and eliminates additional optical elements to relay the reference source images. A thorough description of the construction and testing of the wavefront sensor was completed by T. Rhoadarmer.[28] In this section, I briefly describe the wavefront sensor optical components, I then explain my design and mounting of the collimating doublet.

2.5.1 Collimating Lens Optical Design

The optical components of the wavefront sensor are illustrated in Figure 2.4. The top-box optics place an image of the reference source just before the wavefront sensor; the collimating lens relays that image to infinity. The collimating lens also images the pupil, from infinity, onto the lenslet array. An array of images of the reference source is formed by the lenslets on the detector array. The refractive lenslets are replicated from a master, using optical epoxy, onto a 6 mm thick window of BK7 glass.[29] A broadband anti-reflection coating, optimized for visible wavelengths, is applied to the opposite side of the window. The vertex-to-vertex lenslet spacing is 144 μm and the focal length was measured as 3.429 μm.[30] The lenslet array and detector package are installed in a dewar and are cooled to $-70°$C using a thermo-electric device. To separate the vacuum of the dewar from the atmosphere, a 6.35 mm thick calcium fluoride window was placed between the collimating lens and the lenslet array. Calcium fluoride was chosen over BK7 because of its ability to withstand relatively large amounts of stress. The window is coated on both sides

with a broadband anti-reflection coating, optimized for the visible.

The focal length of the collimating doublet (L1) was chosen, according to equation (2.7), to image the pupil from infinity onto the lenslet array. After optimizing and modeling the top-box, the best focal length for L1 was determined to be 39.74 ± 0.45 mm. The range of focal lengths was set using the pupil image distortion criterion of ± 2 mm on the secondary mirror. A commercially-available achromatic doublet with a focal length of 40 ± 0.8 mm was selected.[§] Ten doublets were purchased and the focal lengths were carefully measured by T. Roberts, using a method he developed involving transmission gratings, to a precision better than 0.1 mm.[31] A doublet with a focal length of 39.74 mm was selected from the ten lenses.

Choosing the proper orientation of the collimating doublet required careful thought. I have summarized the discussion that follows in Table 2.6. Let us call the arrangement in Figure 2.4 orientation A; we call the arrangement where the lens is flipped, so the more steeply curved side faces the lenslet array, orientation B. The doublet relays the $f/23$ reference source image to infinity. To minimize spherical aberration and coma in this situation, the more steeply curved side faces the infinite conjugate.[21,32] This is orientation B. In imaging the reference source, however, the wavefront sensor is always on-axis, thanks to the pupil-steering mirror. This means the field aberrations, such as coma and transverse chromatic aberration, are absent. Furthermore, when relaying the reference source image, orientation B yields about twice the longitudinal chromatic aberration (425 μm versus 210 μm for $\lambda = 0.4$–1.0 μm). Figure 2.7 illustrates this point with spot diagrams for both orientations, on-axis and at full-field. Thus, orientation A is preferred for relaying the reference source image.

The collimating lens serves another function: it images the virtual pupil, which is

[§]Edmund Industrial Optics part no. K32-321; manufacturing tolerance of focal length is $\pm 2\%$.

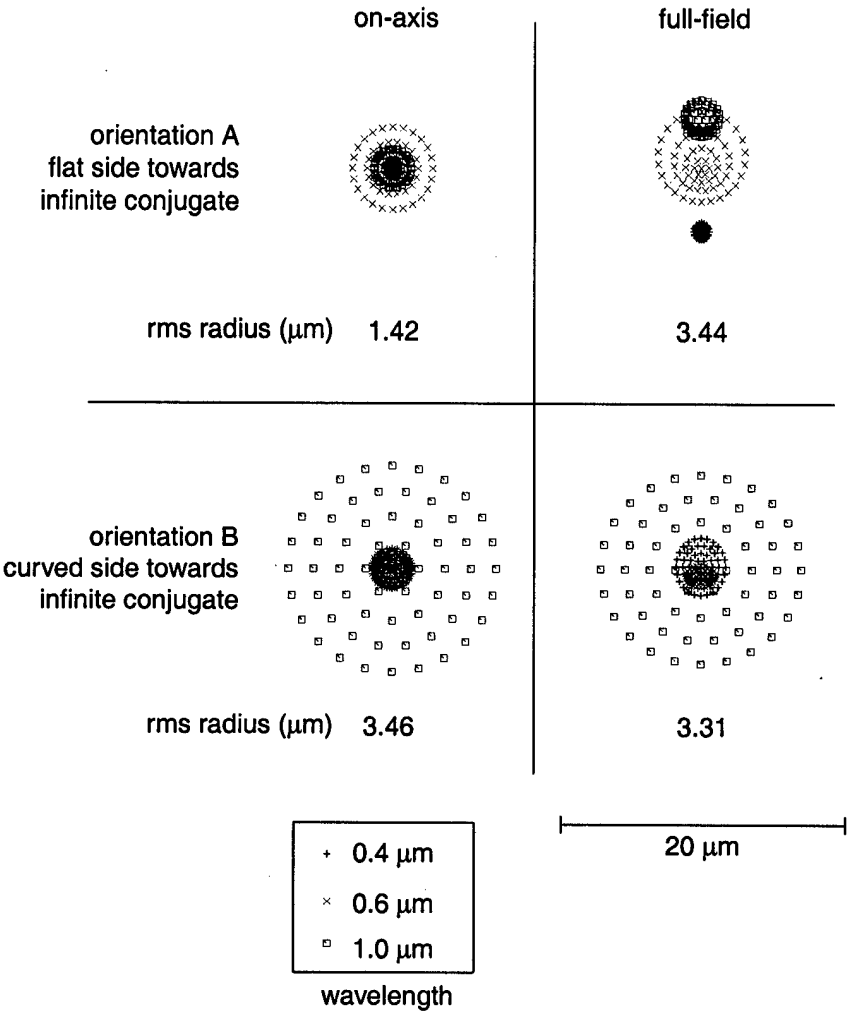

Figure 2.7 Spot diagrams for two orientations of the wavefront sensor collimating lens at three wavelengths. On-axis spots are on the left-hand side, full-field spots are on the right-hand side. The RMS spot radius with respect to chief ray is given. Orientation *A* has more transverse chromatic aberration and less longitudinal chromatic aberration than orientation B; thus, orientation A was chosen for this application.

	reference source imaging				pupil imaging			
orientation	W_{040}	W_{131}	$W_{020\lambda}$	$W_{111\lambda}$	W_{040}	W_{131}	$W_{020\lambda}$	$W_{111\lambda}$
A	0.009	–	−0.015	–	0.001	0	−0.159	0.008
B	0.001	–	−0.159	–	0.009	−0.010	−0.015	−0.275

Table 2.6 Wavefront aberration coefficients for two orientations of the wavefront sensor collimating lens. Orientation A has the more steeply curved side facing the $f/23$ focus; orientation B has the more steeply curved side facing the lenslet array. Figure 2.4 illustrates orientation A. Units are waves at 0.6 μm. The dashes represent field aberrations that do not influence reference source imaging. The aberrations listed are: W_{040} = spherical, W_{131} = coma, $W_{020\lambda}$ = longitudinal chromatic, and $W_{111\lambda}$ = transverse chromatic.

at infinity, onto the lenslet array. For this role, orientation A provides less coma and less spherical aberration. For imaging the pupil, the field aberrations can not be ignored. Transverse chromatic aberration will cause the secondary to be imaged onto the lenslet array at different magnifications.[21,32] Longitudinal chromatic aberration is not a serious problem, as the image of the pupil will be slightly out of focus at different wavelengths. Again, orientation A has better performance in imaging the pupil.

2.5.2 Lens Cell Mechanical Design

The next step was to design a mount for the lens and window. Figure 2.8 shows the basic design. The lens and window are held in a single aluminum cell that attaches to the dewar housing. The window rests directly against the cell with an o-ring making the seal. A spacer lies between the window and the lens. The spacer sets the distance between the lens cell and the back focal plane. First, the distance between the front of the dewar housing and the lenslet array substrate was carefully measured at 23.32 ± 0.025 mm. Next, the lens cell and spacer were manufactured. The spacer would be ground to the proper thickness after the back focal distance of

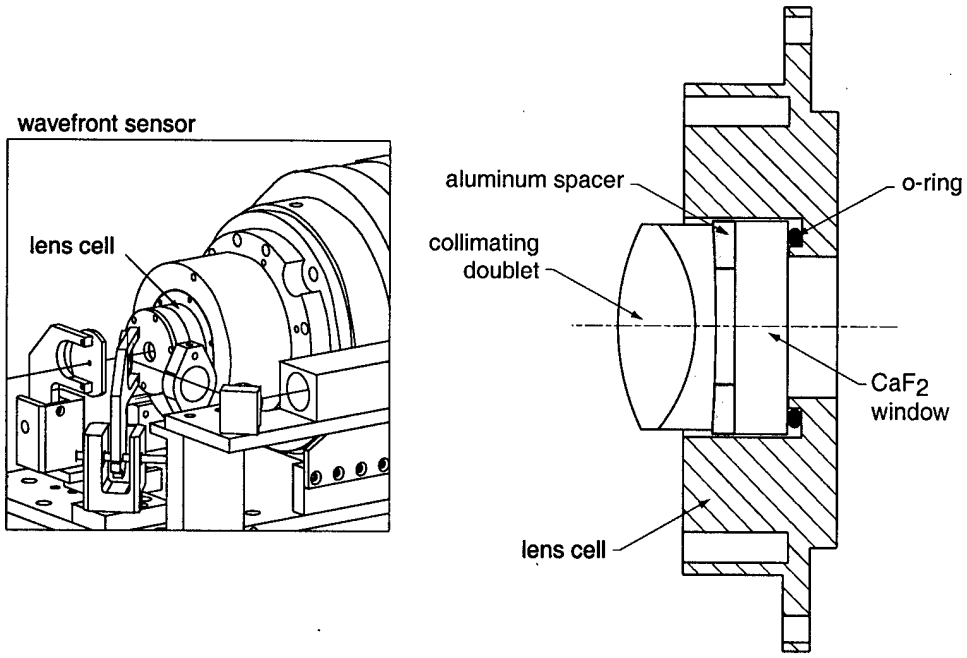

Figure 2.8 Cell for the wavefront sensor collimating lens and dewar window.

the lens was measured. Since force is required to compress the o-ring, axial contact stress, of about 90×10^3 psi, is produced in the lens by the aluminum spacer. To reduce the stress in the lens, a spherical lapping tool was used to grind a bevel on the lens side of the spacer. The bevel increases the contact area between the spacer and the lens which limits the axial stress to about 2×10^3 psi.

To make the spacer for the lens, the back focal distance was required. Since the transmission grating method determined only the effective focal length, the back focal distance was measured directly. Actually, the distance from the back of the assembled lens cell, including the calcium fluoride window, to the focal plane was measured. A phase-shifting interferometer (laser-based Fizeau) was used as illustrated in Figure 2.9. The collimator in the interferometer was adjusted to produce a plane wavefront. Collimation was verified using a shear plate. The assembled lens cell was placed in the beam to bring the light to focus. To limit the beam diameter, and spherical aberration, an aperture was inserted in the beam. A precision ball

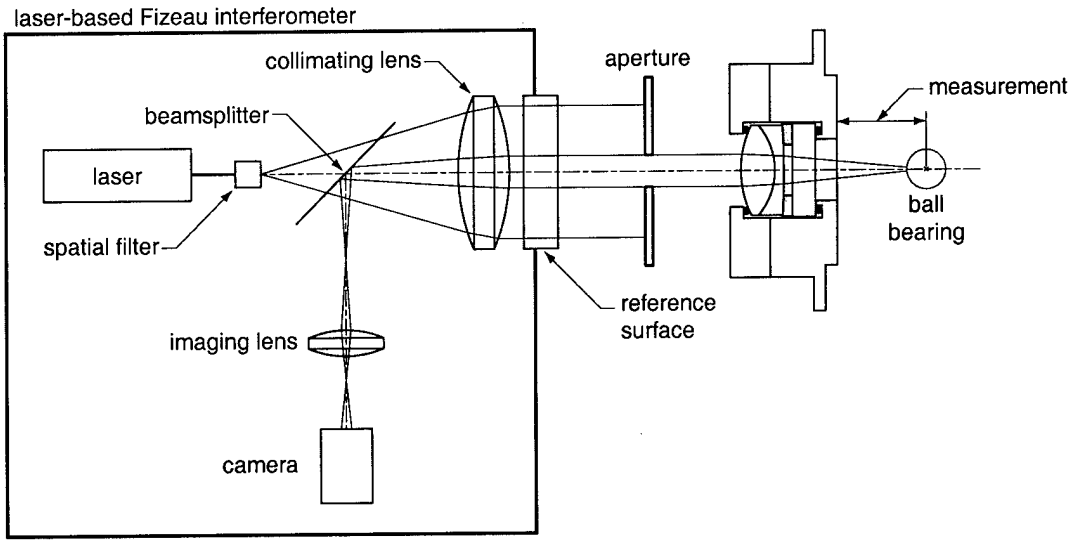

Figure 2.9 Apparatus used to determine back focal plane of the collimating lens mounted in its cell.

bearing was placed so that its center was near the focal point of the lens. The longitudinal position of the sphere was adjusted so that the interferometer measured a plane wavefront. The distance from the lens cell, plus half the diameter of the ball, yielded the back focal distance. Using this measurement, the spacer was ground to the correct thickness to correctly position the focal plane onto the far side of the glass lenslet array substrate.[¶]

After adjusting the thickness of the spacer, the dewar window and collimating lens were installed in their cell. The cell was carefully attached to the dewar housing in a clean room and a vacuum was established. I then installed the wavefront sensor in the top-box and aligned the entire system according to the procedure outlined in Appendix B.

The alignment of the top-box and wavefront sensor, although simple in concept, required careful measurements and adjustments in practice. First, the wavefront sensor optical axis, defined by the optical axis of the collimating lens and the center

[¶]Lens design software was used to model the position of the focal plane through the 6.0 mm thick BK7 lenslet substrate.

of the 12 × 12 lenslet array, was aligned to the mechanical axis of the rotational mount. This was accomplished by adjusting the tilt and translation of the wavefront sensor while observing the motion of the spots and pupil on the detector array as the wavefront sensor was rotated. Then the tilts of the pupil steering mirror and OAP2 were adjusted to eliminate wavefront tilt and to center the pupil on the lenslet array.

After the top-box and wavefront sensor were aligned, I made two performance measurements of the system: the on-axis wavefront aberration was measured and the pupil magnification and distortion were assessed. The next section describes these measurements, after presenting the modeled top-box performance.

2.6 System Optical Performance

To evaluate the top-box imaging performance, I first modeled the system using an optical analysis program. From this model, tolerances for positioning the optical components were developed to meet the design goals. Finally, I measured the top-box optical performance and compared the measurements to the expected performance.

2.6.1 Modeled Optical Performance

The optical design presented in Section 2.4 was entered into an optical design program, then optimized. Pupil mapping from the secondary mirror to the lenslet array and the RMS spot radius on the detector array were used as optimization criteria to adjust the positions of the elements. Since the pupil-steering mirror is used to offset-point the top-box, the wavefront error for fields up to 30 arcsec was evaluated as well. The design goals for the top-box optical performance are summarized in Table 2.7.[25,26]

The first task was to simulate the pupil-mapping errors using optical analysis

description	requirement	goal
pupil size error at lenslet array	±0.02 mm	±0.01 mm
pupil-mapping error at secondary	±6 mm	±2 mm
RMS spot diameter over ±15 arcsec field	0.05 arcsec	–

Table 2.7 Summary of design goals for top-box optical performance.

software. To do this I modeled the secondary as the object with the plane of the lenslet array as the image plane. I then traced rays from a series of points on the secondary to locations on the lenslet array. The model showed that the overall pupil size on the lenslet array was accurate to 0.002 mm. This exceeded the design goal of ±0.01 mm. The pupil-mapping error at the lenslet array, scaled to the secondary, was never more than 0.5 mm. Figure 2.10 shows the modeled mapping error for radially-spaced points on the secondary. The simulation also showed that, although pupil mapping was better than the design goal, the imaging of points on the secondary was not very good. This was not surprising, as the top-box was not designed for imaging over a large field.

After modeling the pupil-mapping performance of the top-box, I modeled its imaging performance. The simulated image quality over a ±15 arcsec field on the sky was close to the design goal. The RMS wavefront error, at the lenslet array, for a series of field angles is displayed in Figure 2.11. These data were simulated by tilting the pupil steering mirror about the y-axis to image a series of field angles on the sky. Recall, the y-axis is perpendicular to the optics bed while the x-axis is parallel to the optics bed. At each field angle, the wavefront sensor was refocused by translating it along the z-axis to minimize the RMS spot radius. Spot diameters in microns on the detector array are given in Table 2.8. Diffraction by the lenslets was not modeled in this analysis. A plate scale of 0.39 arcsec per pixel (24 μm in

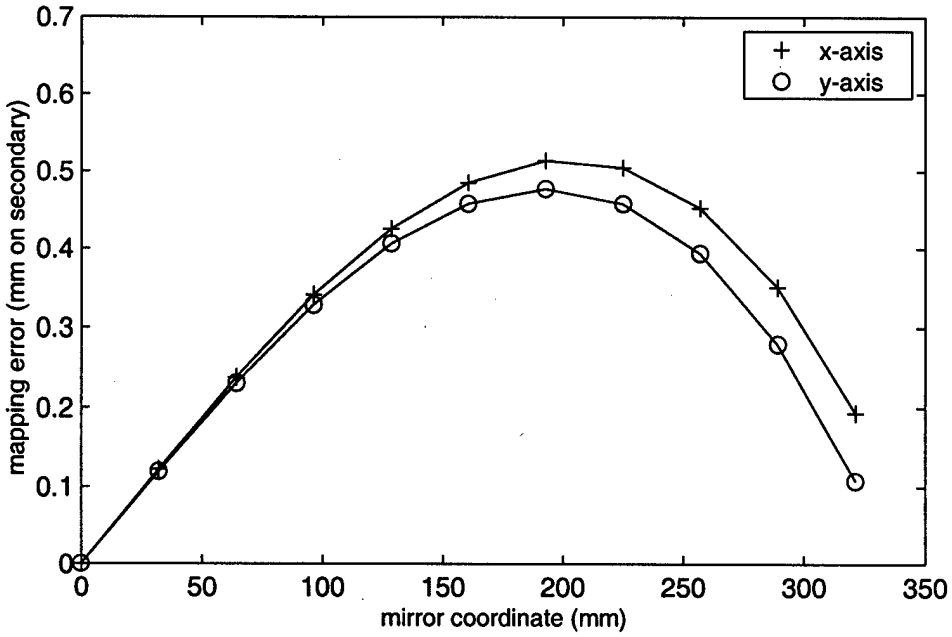

Figure 2.10 Simulated pupil-mapping error at the lenslet array in mm on the secondary.

width) was used to convert the spot diameters to angles on the sky. By far, the dominant aberration for y-tilts of the steering mirror was astigmatism, with coma and third-order spherical making a minor contribution. I expect tilts about the x-axis to introduce much less aberration since OAP2 should be much less sensitive to motions tangential to its axis of symmetry.

2.6.2 Measured Optical Performance

After modeling the optical performance of the top-box, I measured its pupil mapping and on-axis imaging performance. To verify the actual pupil image diameter at the lenslet array some measurements were taken using the shimulator. A complete description of the shimulator and its role in testing the adaptive optics system is given in Chapter 3. Fortunately, a lens nearly identical to the collimating doublet that was installed in the wavefront sensor was available. By placing this lens in the top-box before the wavefront sensor was installed, I was able to form an im-

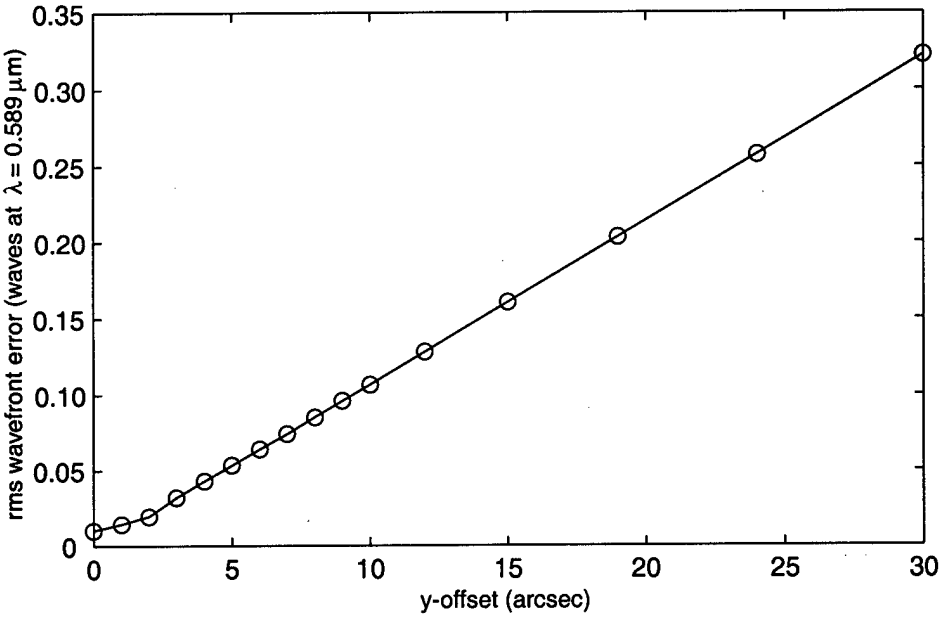

Figure 2.11 Wavefront error at the lenslet array for different field angles. The pupil steering mirror in a simulated top-box was tilted to view a series of field angles on the sky; the RMS wavefront error was then calculated.

field angle (arcsec)	RMS spot diameter (μm)	RMS spot diameter (arcsec)
0	0.2	0.003
10	1.7	0.028
15	2.6	0.043
30	5.2	0.087

Table 2.8 Modeled RMS spot diameter on the wavefront sensor detector array. Diffraction effects by the lenslets were not modeled. A plate scale of 0.39 arcsec per pixel was used to convert the spot diameters to angles on the sky. The unvignetted half-field of the telescope with the $f/15$ secondary is 16 arcsec. The diffraction-limited spot diameter, $2.44\lambda f/D$, is 34 μm.

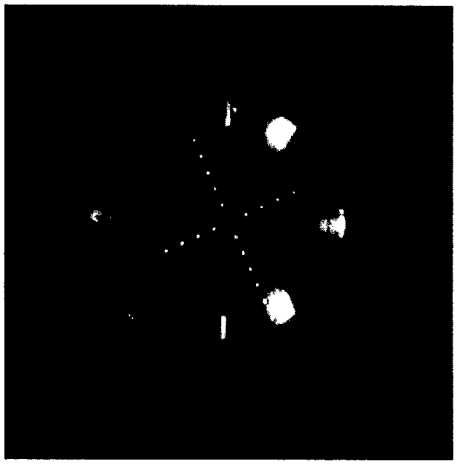

Figure 2.12 Image of secondary mirror as appears at the lenslet array plane. This image was made without the field stop using illumination scattered from the surface of the secondary mirror.

age of the secondary mirror. Using a video detector array in place of the lenslet array, the image shown in Figure 2.12 was obtained. Although the image suffers from spherical aberration, enough detail was present to evaluate the pupil mapping. The small bright dots in the image are fiducial marks placed at 2-inch intervals on the secondary. From the digitized video frame, the diameter of the image of the secondary was estimated at 1.71 ± 0.01 mm. The nominal pupil size is 1.728 mm with an allowable error of ± 0.02 mm.

The wavefront error introduced by the top-box optics was measured by placing a point source at the $f/15$ focus and estimating wavefront gradients with wavefront sensor measurements. I then used the wavefront gradients to reconstruct a wavefront, as discussed in Section 4.2. After accounting for other sources of wavefront error, I found the remaining RMS error was about 50 nm or 0.08 waves. At the wavefront sensor image plane, this corresponds to a spot diameter of approximately 1.4 μm or 0.022 arcsec on the sky. This is within the top-box design specification for collimation errors of less than 0.05 arcsec.[26]

According to a top-box tolerance analysis, an alignment error at OAP2 of 0.25 de-

grees could explain the residual wavefront error measured with the wavefront sensor. The analysis showed the dominant error from introduced tilt was astigmatism, the aberration which dominated the wavefront measurements. Indeed, as explained in Appendix B, OAP2 is intentionally misaligned from its nominal position when the wavefront sensor is aligned to the top-box.

Chapter 3

Adaptive Optics Test Apparatus: the Shimulator

3.1 Introduction

This chapter presents an analysis of the laboratory test apparatus for the 6.5 m MMT adaptive optics system, the *shimulator*.[†] As described in Chapters 1 and 2, the MMT adaptive optics system employs a new and unexplored technology: an adaptive secondary mirror.[33] Every astronomical adaptive optics system requires many days to assemble, test, and troubleshoot. Its numerous components must work together before the benefits of the adaptive optics system can be realized. Optical elements must be mounted and aligned, electronics must be installed and connected, software algorithms must be written and debugged. These are time-consuming tasks, especially when new instruments and technologies are developed and implemented. Many of these tasks can be completed with individual components on the electronics workbench or in the optics laboratory, but closed-loop testing of the entire adaptive optics system is often completed on the telescope. These on-

[†]The shimulator is named for one of its functions: simulating a shimmering atmosphere.

telescope engineering trials consume valuable observing time, which would otherwise be dedicated to scientific investigations. Furthermore, engineering trials of the whole adaptive optics system usually require a telescope which is largely operational. In the case of a new telescope or the upgrade of an existing telescope, this requirement prevents the parallel development and testing of the adaptive optics system and the telescope.

The solution to this challenge is to develop and test the entire adaptive optics system in the laboratory, before it is installed on the telescope. This permits a thorough and complete investigation of new instruments and algorithms without the competition and urgency that ordinarily accompanies the use of telescope time. Work in the laboratory is usually more efficient than work on an isolated mountain-top; laboratories are generally less remote with convenient access to the necessary infrastructure. The environment in the laboratory is more readily controlled than a telescope enclosure, permitting the isolation of the behavior of system components from significant environmental changes.

The testing of large convex aspheric mirrors, however, presents its own set of difficult challenges. One common method for testing aspheric surfaces uses auxiliary elements, known as null compensators or null correctors, which, when combined with the wavefront from the aspheric surface, produces a converging spherical wavefront.[34] Convex mirrors, unlike concave mirrors, do not convert light diverging from a point source into a converging beam. Therefore, the null corrector to test a convex aspheric mirror in reflection must be at least as large as the convex mirror under test. The Hindle test can be used to test a convex hyperboloid mirror, without a null compensator.[35] The convex hyperboloid is placed with its rear focus at the center of a large sphere as shown in Figure 3.1 (a). Light leaving the front geometrical focus of the hyperboloid will retro-reflect from the sphere, back to the

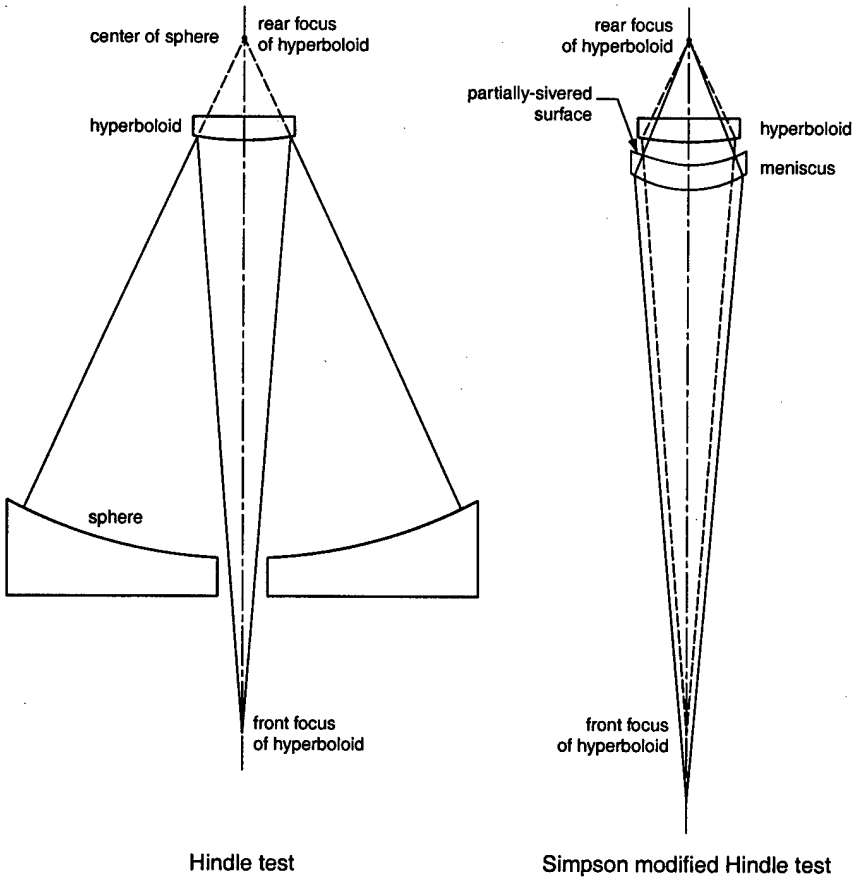

Figure 3.1 Traditional tests for convex hyperboloid mirrors. The figure on the left shows the Hindle test; the figure on the right shows the Simpson modified Hindle test.[34]

front focus. Unfortunately, to perform the Hindle test without a relatively large obscuration requires a spherical mirror much larger than the convex mirror.[34] A modification of the Hindle test has been devised which does not require large reference spheres.[36,37] The retro-reflection is provided by a partially-silvered concave surface of a transparent meniscus as shown in Figure 3.1 (b). The spherical aberration resulting from transmission through the concave surface of the meniscus can be balanced by proper choice of the radius of curvature of its convex surface.[38]

Either of the Hindle tests is adequate for measuring the surface quality of a convex hyperboloid; however, testing an adaptive optics system with a Hindle-type

test is problematic. Since there are *two* reflections from the hyperboloid mirror surface, any path change introduced by an adaptive secondary mirror is doubled. Therefore, it takes only half of the usual actuator motion to cancel the optical path variations measured by the wavefront sensor. This situation would not permit realistic tests of the adaptive secondary at correcting strong turbulence at the full dynamic range of the wavefront sensor. Additionally, mirror control laws developed on the shimulator could not be employed in operating the adaptive optics system on the telescope without first modifying the control relationships.

A more serious difficulty exists with using the modified Hindle test to exercise the 6.5 m MMT adaptive optics system in particular. Recall, the adaptive optics system uses two wavelength bands for operation: to sense global tilt it uses the advantage of a smaller image and larger isoplanatic patch in the infrared, while it senses higher-order aberrations in the visible. Thus, a full test of the adaptive optics system requires simultaneous dual-wavelength testing. Because of dispersion in the glass of the meniscus Hindle element, dual-wavelength operation would not be possible without making its design achromatic. This, in itself, would be a challenging design effort.

A solution to this challenge lies in the use of a computer-generated hologram.[39] Researchers at my institutions, the Steward Observatory Mirror Laboratory and the Optical Sciences Center, have pioneered techniques in using circular computer-generated holograms in testing aspheric surfaces—null correctors for large fast telescope primaries and for performing null tests of telescope secondaries directly.[40,41] A large full-size positive lens is placed directly in front of the hyperboloid secondary, as illustrated in Figure 3.2. The positive lens creates a converging wavefront normal to the mirror and focuses the light reflected from the mirror. Although the power of the large positive lens is split into two lenses to reduce spherical aberration,[42] a

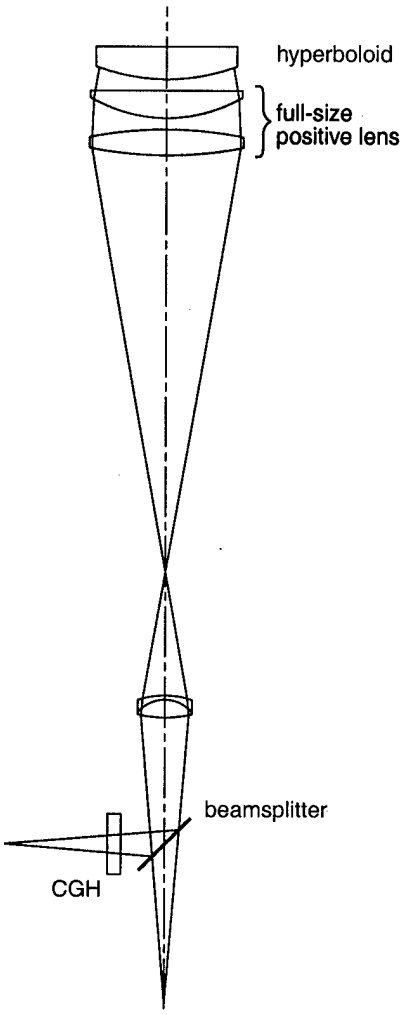

Figure 3.2 Concept for the shimulator optical design.

significant amount remains—about 850 waves at 594 nm, at the edge of the pupil. In addition, the hyperboloid secondary introduces about 1100 waves of spherical aberration. A computer-generated hologram is inserted into the outgoing beam to correct the tremendous amount of spherical aberration.[43] The computer-generated hologram must correct the aberrations at two wavelengths simultaneously. This is accomplished by interleaving or multiplexing two hologram patterns on the same substrate.

This test apparatus allows calibration and operation of the entire adaptive optics system, except for the laser beacon, in the laboratory. To help verify the shimulator alignment and to help calibrate the response of the wavefront sensor, a phase-shifting interferometer has been included. The next sections explain the optical and mechanical design of the shimulator in more detail. My work did not include designing the shimulator, but assembling and aligning it, and using it to test and calibrate the wavefront-sensing portion of the adaptive optics system. I present the optical design here simply for completeness. Section 3.4 gives an overview of the techniques that were developed and implemented to align the shimulator; special attention is given to design tolerances and compensators. Finally, Section 3.5 presents measurement and analysis of shimulator performance. For a description of how the shimulator was used to test and calibrate the wavefront sensor, please see Chapter 4.

3.2 Shimulator Optical Design

3.2.1 Shimulator Optical Design Requirements

The optical design of the shimulator had several demanding requirements, several of which are listed in Table 3.1.[39] As mentioned above, since the 6.5 m MMT adaptive optics system uses two wavelength bands to sense atmospheric path variations, a complete test of the system required the shimulator work the same for two wave-

specification	design goal
wavelength	simultaneous 594 nm and 1550 nm
focal plane	same as telescope; coincident for both wavelengths
pupil plane	coincident for both wavelengths
pupil mapping	< 2 mm at secondary mirror
portable	same optical design for laboratory and telescope
size	must fit within telescope interior envelope

Table 3.1 Shimulator optical design goals.[39]

lengths: one in the visible and one in the near infrared. The wavelengths chosen were based partly on the laser wavelengths that were commercially available. The 594 nm helium-neon laser wavelength is fortunately close to the 589 nm sodium laser beacon wavelength; reliable semiconductor lasers at 1550 nm are easily obtained.

For this work, however, the shimulator was operated and tested at only the visible wavelength. The original design of the turbulence generator used a flow of heated air through a portion of the beam.[28] Since the chromatic dispersion of air is negligible, the heated-air turbulence generator introduced the same path length variations for both wavelengths. Unfortunately, the heated-air design could not be made to match the strength turbulence found at the MMT. The design was changed to a near-index-match between two materials: acrylic and mineral oil. The acrylic was machined to match the Kolmogorov turbulence model. To reduce the phase variations introduced by the machined acrylic surface, mineral oil, with a refractive index close to that of acrylic, was used. The difficulty is the chromatic dispersions of acrylic and mineral oil differ; thus, the wavefront distortion imparted by the turbulence plate would differ for the two wavelengths. Both wavelengths could not be used with the current turbulence generator plates. As a result, until

this problem could be solved, it was decided to operate the shimulator with only 594 nm wavelength light.

The shimulator design should replicate the optical and mechanical characteristics the adaptive optics system will encounter when it is transferred to the telescope. This way, when the system is finally integrated with the telescope, few configuration changes will be required. The location of focal planes and pupil images should be the same relative to the top-box mounting flange. The f-number of the beam returned by the shimulator should be the same as the telescope f-number. For control of the adaptive mirror to work properly, the mapping of the secondary mirror to the pupil image at the wavefront sensor lenslet array must be accurate. The same pupil-mapping criterion that applied to the design of the top-box, less than 2 mm of error on the deformable secondary, was applied to the shimulator optical design. Lastly, testing of the adaptive optics system, during integration with the telescope, should not interfere with telescope operations at night. The shimulator optical mounts are being designed to be installed on the telescope during the day so the adaptive optics system can be tested without opening the telescope enclosure. The shimulator components can then be removed from the normal telescope optical path at dusk and reinserted the next morning. This presents a formidable challenge to the designer of the optical mounts if the large optical elements are to be positioned while maintaining the strict alignment tolerances.

3.2.2 Shimulator Optical Design Overview

An overview of the shimulator optical design is shown in Figure 3.3. Light from a 594 nm helium-neon laser is coupled into a single-mode optical fiber to form the source.[44] The speed of the beam leaving the fiber is increased with a small negative lens to overfill the 50 mm diameter computer-generated hologram. The hologram was made to add just enough aberration to offset the spherical aberration which will

be imparted farther along the optical path. When needed, the two near-index-match turbulence generators are placed between the source and the computer-generated hologram.[28] The position of the turbulence generators can be adjusted along the beam to control the strength of the turbulence. When no turbulence is needed, flat acrylic windows take the place of the turbulence plates to occupy the same optical thickness in the path. This eliminates the need to reposition the source when the turbulence generators are removed.

The beam, with its large amount of spherical aberration, is then folded upwards 90 degrees by a partially-reflecting beamsplitter. A doublet, which has a focal length of 536 mm, focuses the light roughly 1.4 m above.[‡] The diverging beam travels another 6.7 m from the focus to just before the secondary mirror where it encounters a large two-element lens; the first element is equi-convex and the second is plano-convex. The converging rays reflect from the secondary at nearly normal incidence, and travel back through the two-element lens. Now, largely free of spherical aberration, the beam comes to a focus about 0.9 m above the smaller doublet. This is evident in Figure 3.4 which shows the outgoing beam and the incoming beam at the caustic above the small doublet. The spherical aberration, readily apparent in the outgoing beam, is absent from the incoming beam.

The doublet relays the stigmatic image to the simulated telescope focus, at $f/15$, about 1.3 m below. This beam is reflected upwards into the top-box by a mirror in the place of the dichroic beamsplitter in the ARIES dewar. Because the image of the secondary mirror formed by the shimulator, as seen from the top-box, is not the same distance as the secondary mirror in the telescope, a lens is placed at the $f/15$ focus. This weak lens, with a focal length of 750 mm, corrects the pupil imaging in the top-box. Without the lens, the image of the secondary would not be formed on

[‡]Because of the large amount of spherical aberration, the term *focus* is ambiguous. I am describing the path of the marginal rays as they cross the optical axis.

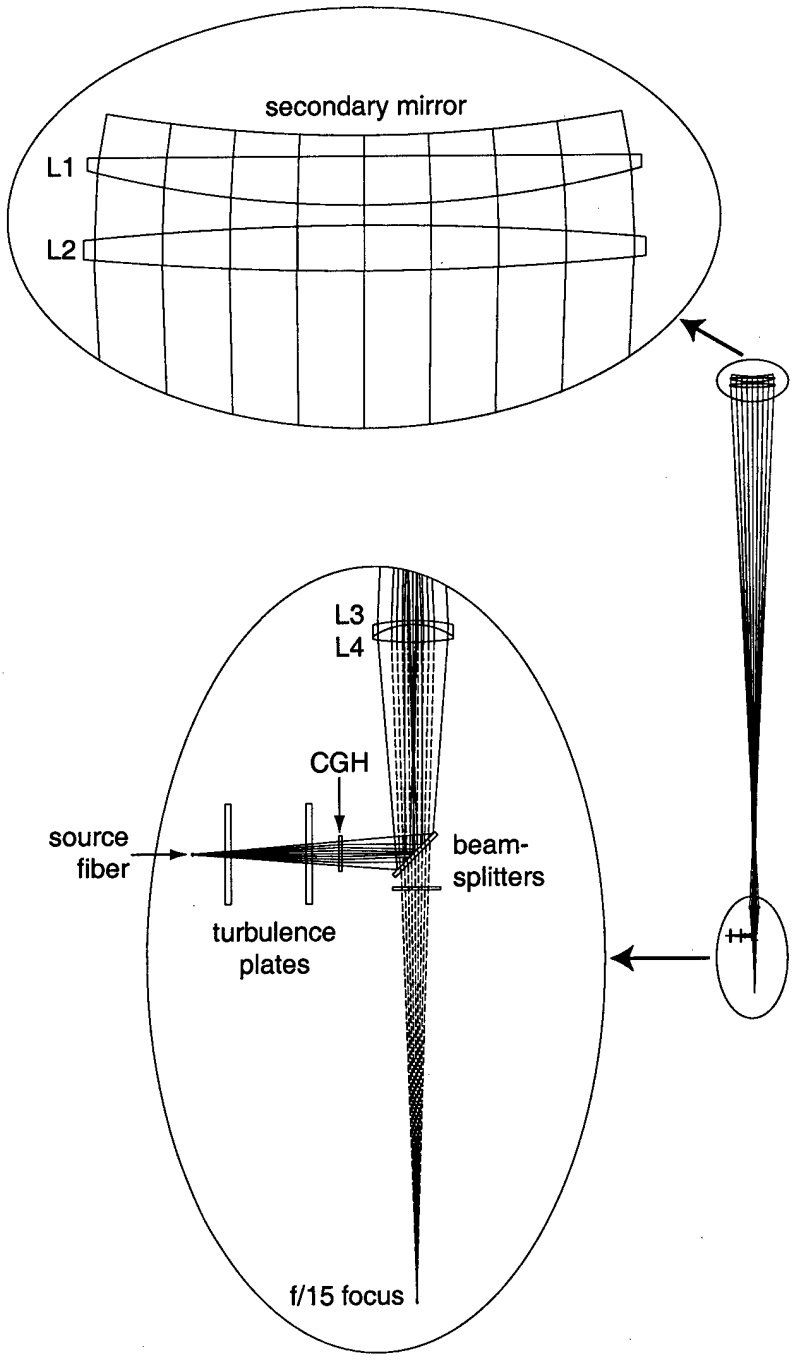

Figure 3.3 Overview of shimulator optical layout. Detailed views of the source and image portion, and the secondary mirror portion of the optical path are shown. Solid lines mark the outgoing beam path; dashed lines show the beam path after reflection from the secondary mirror. Only the 594 nm beam path is illustrated.

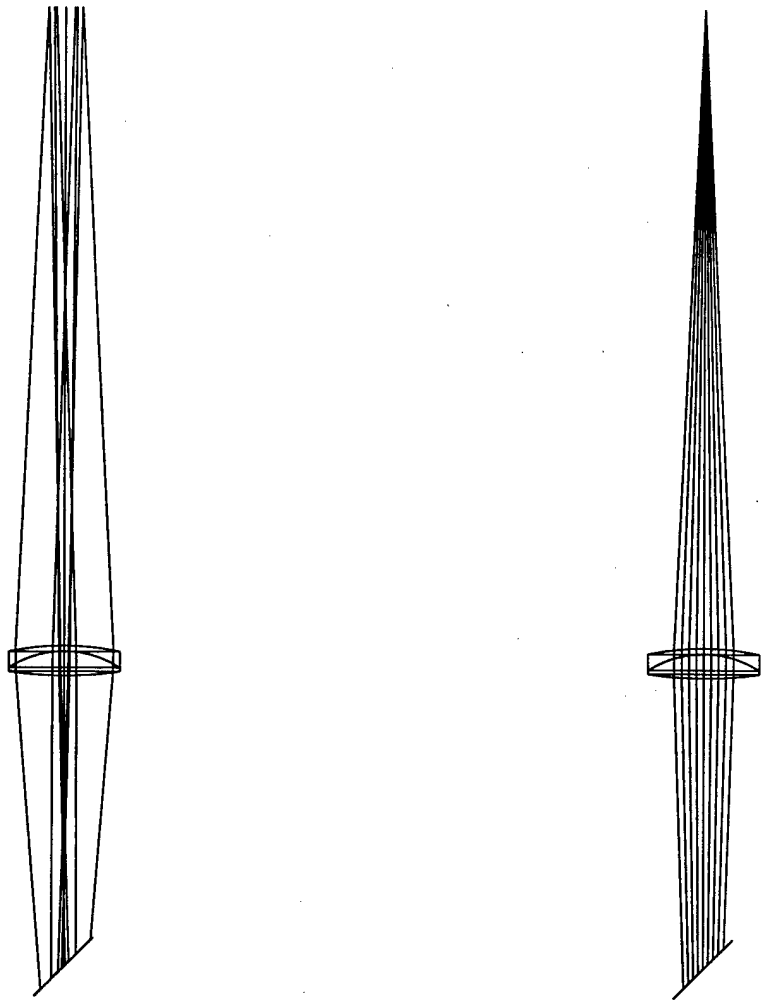

Figure 3.4 Comparison of the spherical aberration in the outgoing and returning shimulator beams just above the smaller doublet, L3 and L4. The left-hand figure shows the outgoing beam with the negative spherical aberration imparted by the computer-generated hologram. The right-hand figure shows the returning beam after the spherical aberration has been corrected.

the pupil-steering mirror, causing translation of the pupil at the wavefront sensor when the pupil-steering mirror is tilted.

3.2.3 Correcting Astigmatism in the Shimulator

To allow the phase-shifting interferometer to measure the wavefront which is sent to the top-box, beamsplitters are used. On the way to the $f/15$ focus, the beam encounters two partially-reflecting beamsplitters, both 8 mm thick and angled 45 degrees to the beam. The first beamsplitter is the one that turned the beam upward, after it left the hologram; the other sends light to the phase-shifting interferometer.[45,46]

Since the beamsplitters are tilted about orthogonal axes, much of the aberration they impart to the *transmitted* $f/15$ beam is canceled. Thus, the beam that goes to the top-box is mostly free from aberration. This is not the case for the *reflected* beam passing through only one beamsplitter on its way to the phase-shifting interferometer. A tilted parallel plate, when placed in a converging or diverging beam, shifts the beam laterally and introduces aberrations, mostly astigmatism.[21] The wavefront aberration coefficients for a tilted glass plate are given by

$$W_{040} = -\frac{1}{8}\left(\frac{n^2-1}{n^3}\right) u^4 t \qquad \text{spherical} \tag{3.1}$$

$$W_{131} = -\frac{1}{2}\left(\frac{n^2-1}{n^3}\right) \bar{u}\, u^3 t \qquad \text{coma} \tag{3.2}$$

$$W_{222} = -\frac{1}{2}\left(\frac{n^2-1}{n^3}\right) \bar{u}^2 u^2 t \qquad \text{astigmatism} \tag{3.3}$$

$$W_{311} = -\frac{1}{2}\left(\frac{n^2-1}{n^3}\right) \bar{u}^3 u\, t \qquad \text{distortion} \tag{3.4}$$

where n is the refractive index of the glass, $\bar{u}$ is the chief ray angle with respect to the plate, u is the marginal ray angle with respect to the chief ray, and t is the thickness of the plate.[32] For an 8 mm thick plate of BK7 glass and an $f/15$ beam,

symbol	W_{040}	W_{131}	W_{222}	W_{311}
aberration	spherical	coma	astigmatism	distortion
coefficient	−0.000775	−0.073	−1.72	−40.5

Table 3.2 Wave aberration coefficients for an 8 mm thick beamsplitter at $f/15$ calculated using Equations (3.1) through (3.4). The index of the BK7 glass is 1.517; the units are waves at 594 nm.

the wave aberration coefficients, with their names, are listed in Table 3.2. Using optical analysis software, I calculated the root-mean-square (RMS) wavefront error as 0.41 waves at 594 nm, excluding tip, tilt, and focus.

Just as the second beamsplitter canceled most of the aberration imparted by the first beamsplitter to the transmitted beam, a tilted parallel plate is introduced into the reflected beam to compensate for aberrations. This situation is illustrated in Figure 3.5 where the beam reflected to the phase-shifting interferometer is shown. Rays from the secondary are aberrated by passing through the first beamsplitter. The rays reflect from the second beamsplitter and are folded 90 degrees by a flat mirror. A 3 mm diameter mask is placed just before the $f/15$ focus to eliminate the unwanted orders of the circular computer-generated hologram.[40] A tilted plate, which doubles as the beam combiner for the interferometer, cancels much of the aberration introduced by the first beamsplitter. Table 3.3 lists the Zernike polynomial coefficients which show the effect of introducing the corrector plate; the effect of introducing a corrector plate of the wrong thickness is also shown. The small amount of wavefront distortion remaining is from those aberrations which do not cancel when rotated by 90 degrees. Zernike phase components that depend on twice the angular pupil coordinate 2θ, such as astigmatism, cancel; those that are rotationally symmetric or depend on θ, 3θ, or 4θ do not cancel. The optical analysis program reports the remaining RMS wavefront error as 0.013 waves at 594 nm, excluding tip,

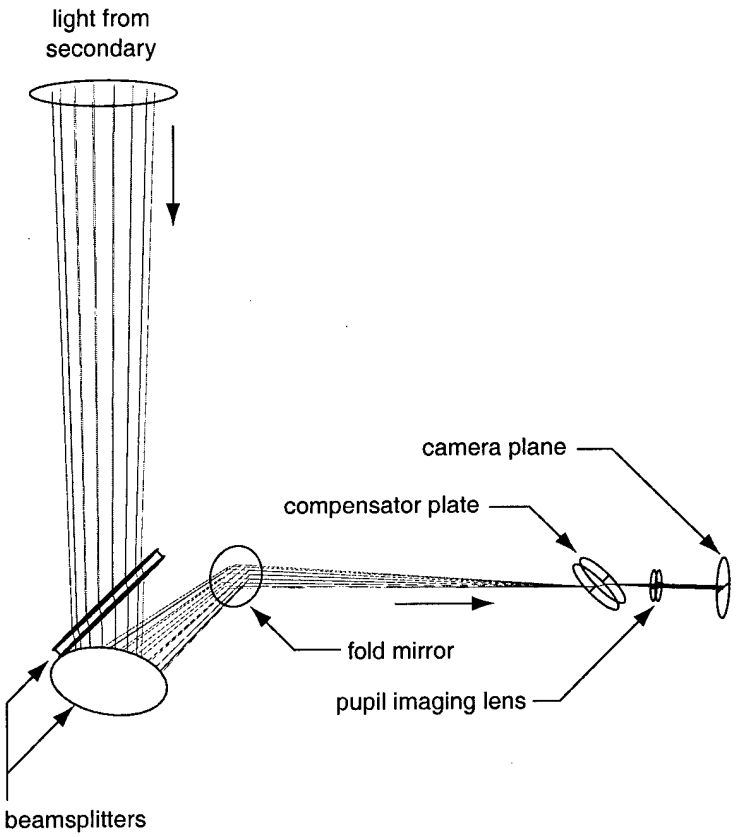

Figure 3.5 Shimulator beam path to the phase-shifting interferometer. Rays from the secondary are aberrated by passing through the first beamsplitter. A tilted compensator plate, which doubles as the beam combiner for the interferometer, cancels much of the aberration introduced by the first beamsplitter.

corrector plate thickness			
none	8 mm	5 mm	polynomial
0.00	15.68	9.80	$r\cos(\theta)$
−15.74	−15.68	−15.70	$r\sin(\theta)$
−170.01	−28.04	−81.22	$2r^2 - 1$
0.00	0.00	0.00	$r^2\sin(2\theta)$
240.69	0.00	90.18	$r^2\cos(2\theta)$
−5.56	−5.54	−5.55	$(3r^3 - 2r)\sin(\theta)$
0.00	5.54	3.46	$(3r^3 - 2r)\cos(\theta)$
0.97	0.96	0.96	$r^3\sin(3\theta)$
0.00	0.96	0.59	$r^3\cos(3\theta)$
0.00	−0.06	−0.04	$6r^4 - 6r^2 + 1$

Table 3.3 Zernike polynomial coefficients show the effect of introducing the 8 mm thick corrector plate: astigmatism is totally eliminated. The effect of introducing a corrector plate of the wrong thickness, 5 mm, is also shown. Units are nanometers, normalized to unit RMS. The y-axis is vertical and the x-axis is horizontal, θ is measured from the x-axis, increasing counter-clockwise.

tilt, and focus. A single-mode fiber, placed just above the tilted compensator plate, introduces the reference beam. A small positive lens images the secondary mirror onto a video detector array.

3.2.4 Phase-Shifting Interferometer

A self-contained laser source supplies the test and reference wavefronts for the shimulator phase-shifting interferometer. It applies a shift to the phase of the reference beam and includes controls to optimize contrast in the interferogram. A schematic diagram of the laser source for the shimulator is shown in Figure 3.6.[44] Both the test beam and the reference beam are supplied from the same laser. The beams are transmitted to the shimulator over single-mode optical fiber. The test beam

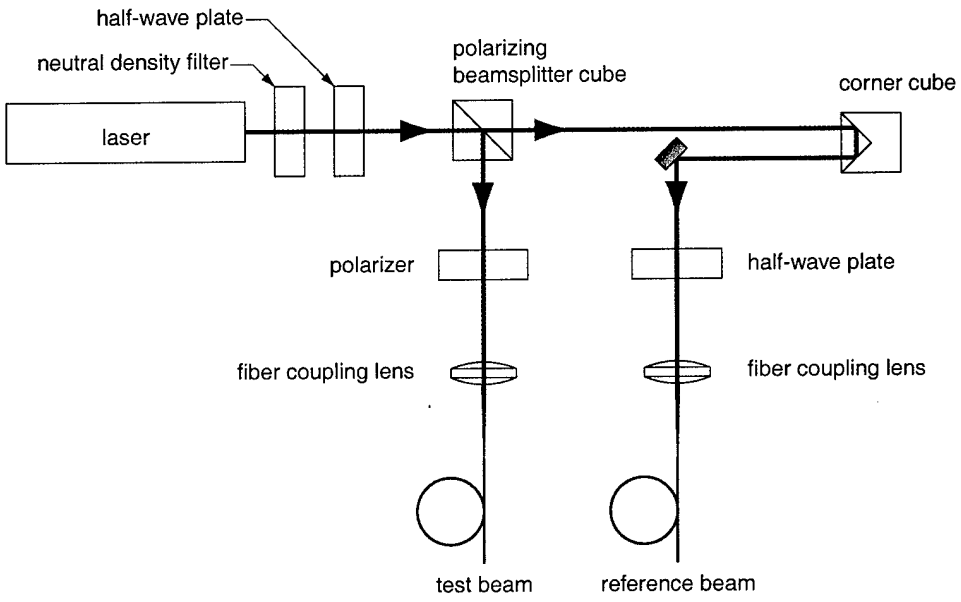

Figure 3.6 Schematic diagram of laser source for the shimulator. The laser output is split by a polarizing beamsplitter cube; one beam becomes the test beam while the other becomes the reference beam. A half-wave plate controls the fraction of light sent to each beam. The phase of the reference beam is shifted by a piezoelectric transducer which moves the corner cube and changes the path length. A second half-wave plate controls the polarization of the reference beam to maximize fringe contrast in the interferogram. Both beams are coupled into single-mode optical fibers for transport to the shimulator.

is injected into the shimulator just before the computer-generated hologram; the reference beam is combined with the test beam at the compensator plate in the interferometer. The wavefront sensor in the top-box receives only the test beam.

The source starts with a laser which produces 2 mW of continuous power at 594 nm wavelength; the output is linearly polarized. Neutral density filters are inserted onto the laser beam to control the overall intensity. A half-wave plate, in a rotating mount, controls the angle of polarization of the beam which enters a polarizing-beamsplitter cube. This determines the ratio of the intensity transmitted and reflected by the beamsplitter cube. The reflected light is coupled into a single-mode optical fiber to become the test beam. A linear polarizer controls the intensity of the test beam. The transmitted light is retro-reflected by a corner cube before being coupled into the optical fiber for the reference beam. The test beam, after passing through the shimulator, is combined with the reference beam in the interferometer. A half-wave plate sets the polarization angle of the light in the reference beam, allowing the contrast of the interference fringes to be maximized. The corner cube is mounted on a translation stage driven by a piezoelectric actuator for phase shifting. The phase of the reference beam is shifted by applying a voltage to the actuator, which moves the corner cube and changes the path length. The coarse position of the corner cube is adjustable so the path difference in the two beams can be set to an even integer multiple of the laser cavity length. This places the longitudinal laser modes in phase and improves contrast in the interferogram.

A personal computer is used to control the phase shift of the reference beam. It contains an analog-to-digital converter which produces the voltage to drive the piezoelectric transducer. The shimulator test beam is combined with the reference beam to produce an interferogram which is imaged onto a detector array. The video signal from the detector array is digitized by a frame-grabber in the personal com-

puter. Five interferograms, with $\pi/4$ phase steps of the reference beam, are digitized to reconstruct the test wavefront. Commercial software is used to control the piezoelectric transducer, digitize the video signal, and reconstruct the wavefront. The software typically uses the five-step Hariharan algorithm to reconstruct the wavefront.[47] The Hariharan algorithm is insensitive to quadratic detector nonlinearity and, most importantly, it can tolerate large errors in the phase steps. For example, a $\pi/20$ error in the $\pi/4$ phase step (81 degrees versus 90 degrees), yields a maximum wavefront phase error of about $\pi/500$.[45]

3.2.5 Shimulator Optical Design Review

A review of the flow of signals between the components of the adaptive optics test system is illustrated in Figure 3.7. Different symbols are used to represent the various types of links between the components. The diagram does not include control of the secondary mirror, which is not yet implemented in the shimulator. Soon, a link between the wavefront computer and the secondary mirror interface will be added, permitting closed-loop correction of wavefront distortions. Presently, two personal computers are used: one to collect and analyze the phase-shifting interferometer data, the other to control and analyze the wavefront sensor data. The final products of the test system, at least for this work, are two types of wavefronts:

1. wavefronts reconstructed from interferograms produced by the phase-shifting interferometer, and
2. wavefronts reconstructed from images produced by the Shack-Hartmann wavefront sensor.[§]

The wavefronts produced with the interferometer were used to verify the calibration of the those produced by the wavefront sensor, as discussed in Chapter 4.

[§]See Section 2.5 for a description of the wavefront sensor hardware and Section 4.3 for a discussion on how wavefronts are reconstructed from wavefront sensor measurements.

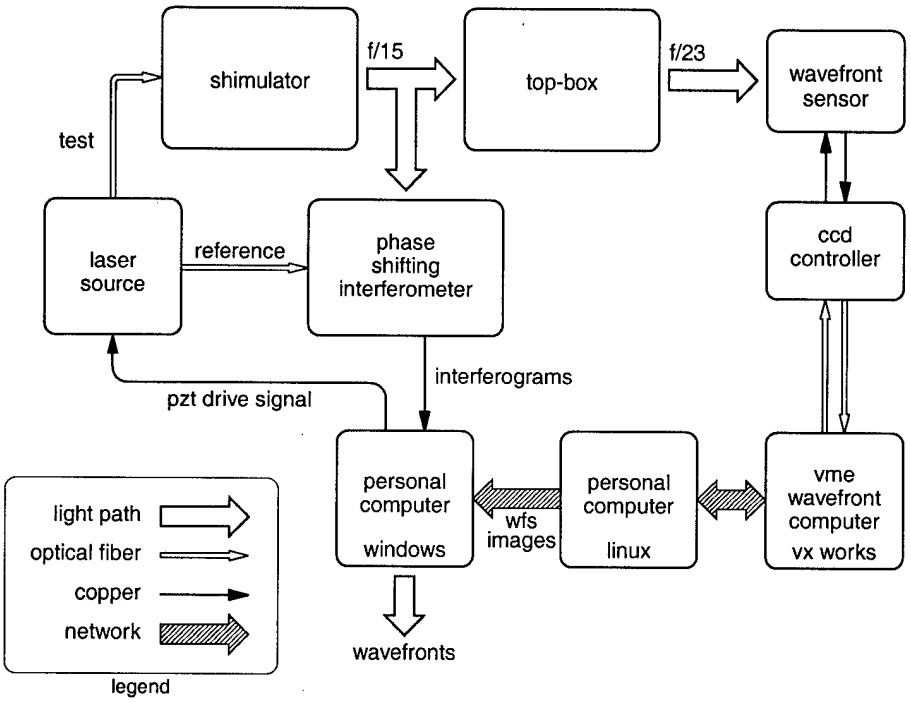

Figure 3.7 Flow diagram for the shimulator and top-box. Different symbols are used to represent the various types of links between the components. Two personal computers are used: one to collect and analyze the phase-shifting interferometer data, the other to control and analyze the wavefront sensor data.

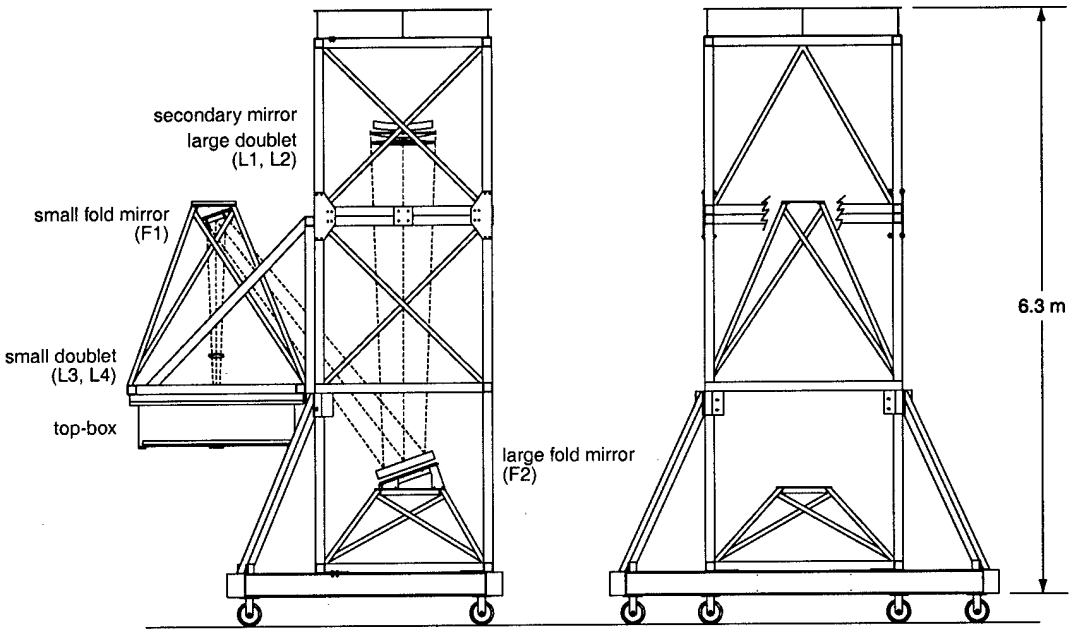

Figure 3.8 Drawing showing two views of the shimulator tower.

3.3 Shimulator Mechanical Design

This section describes how the shimulator optical elements are mounted and how their positions are adjusted. Two views of the nearly 7 m tall shimulator tower are shown in Figure 3.8. Four outriggers, which add stability and provide vibration isolation using pneumatic actuators, are not shown in the drawing. The 8 m optical path between the doublet and the large lenses, shown earlier in Figure 3.3, has been folded twice. The first fold is from a solid elliptical mirror, about 22 × 34 cm along its axes; the second fold is from a light-weighted 50 cm diameter circular mirror. The mirror surfaces are parallel with the fold angle at each surface about 38 degrees; their tilts are adjustable in two axes. The secondary mirror is suspended from the shimulator tower by a hexapod. The hexapod, shown in Figure 3.9, has 6 legs, whose lengths are independently adjusted to control the position of the secondary mirror in 6 axes. The hyperboloid secondary mirror, still attached to its blocking body[¶], is

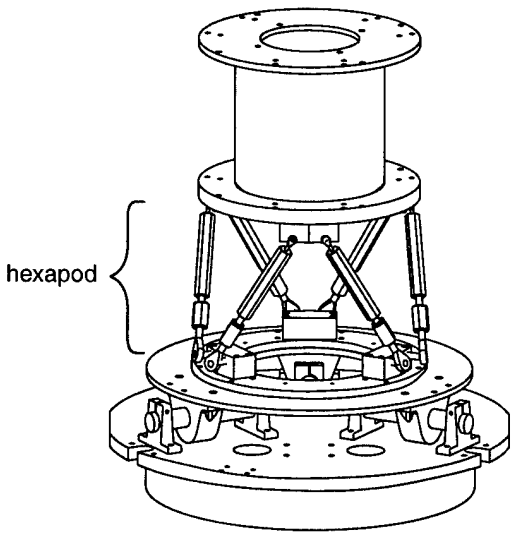

Figure 3.9 Drawing showing the hexapod support for the secondary mirror. The hexapod has 6 legs whose lengths can be independently adjusted to control the position of the secondary mirror in 6 axes. The secondary mirror, still on its blocking body, is suspended below the hexapod with a whiffletree. The three-point whiffletree for the spherical secondary is shown; a nine-point whiffletree was used for the hyperboloid secondary.

held below the hexapod with a nine-point whiffletree.[15] The large 70 cm diameter lenses are mounted in a single lens cell suspended from the top of the shimulator by three threaded steel rods. The tilt and vertical (z-axis) position of the lenses is adjusted by turning nuts on the threaded rods. The horizontal (x- and y-axis) position is controlled by two fine-thread screws which press against the side of the lens cell.

The remaining shimulator optical components are placed in the top-box as pictured in Figure 3.10. The smaller doublet (L3, L4) is mounted in a lens cell with three fine-thread screws which control its tilt in two axes. Micrometers are used to adjust the translational (x-, y-, and z-axis) position of the doublet. The two beamsplitters are held in a single mount whose vertical position and tilt in two axes

¶The aspheric mirror shell had not yet been integrated with the adaptive secondary; thus, the shimulator was tested with the shell attached to the blocking body.

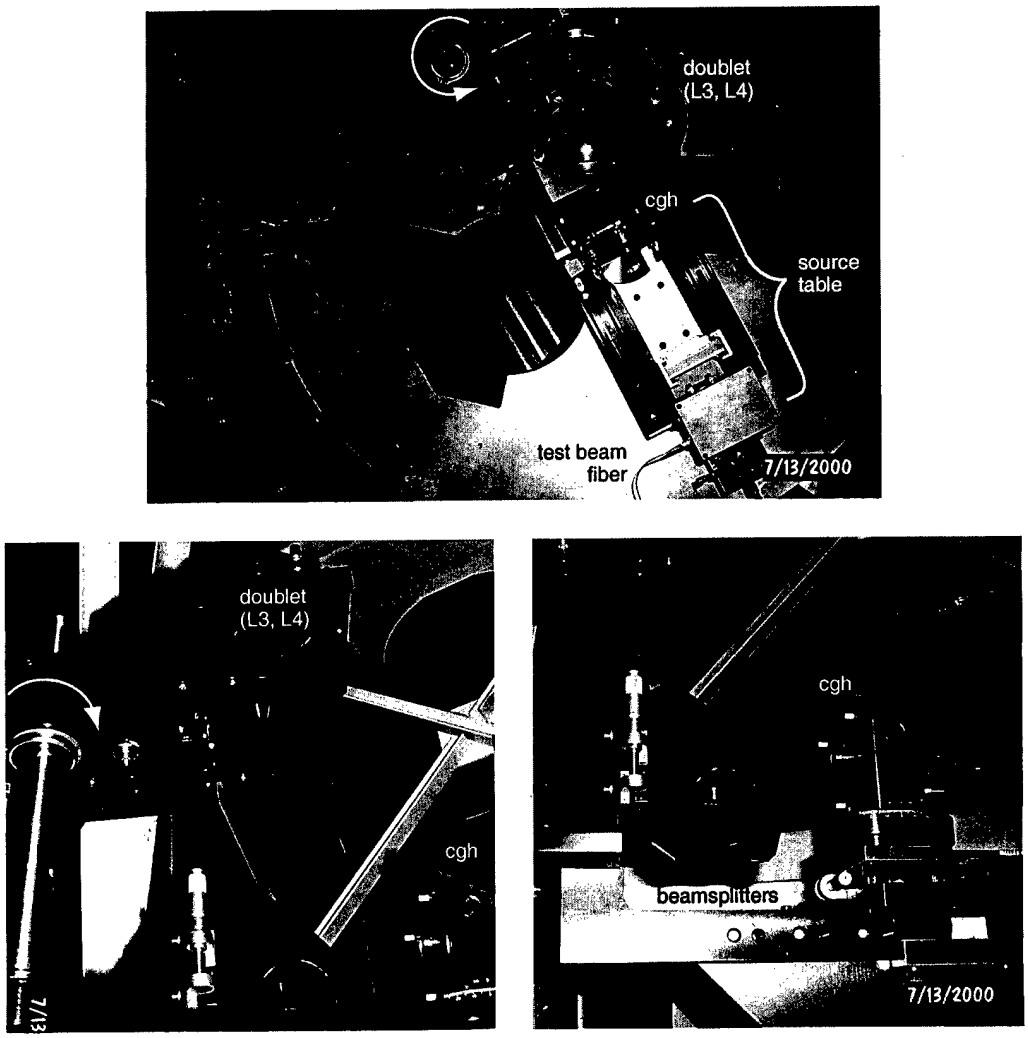

Figure 3.10 Photographs showing three views of the shimulator components in the top-box. The top photograph is a view from above the top-box. The turbulence generator plates are not present, instead four plain acrylic plates are shown.

are adjustable. The doublet lens cell and beamsplitters are attached to a movable cantilever. When the shimulator is installed on the telescope, the cantilever swings to remove doublet and beamsplitters from the beam path. The computer-generated hologram, turbulence generator plates, and test beam optical fiber are mounted on an single aluminum plate, called the source table. Their positions on the table, as well as the position of the table, are adjusted with linear translation stages and micrometers. In addition, the computer-generated hologram is held in a gimbal mount with adjustable two-axis tilt.

The phase-shifting interferometer is positioned in the top-box as shown in Figure 3.11. Light from the smaller doublet is folded into the plane of the top-box optics bed by the lower beamsplitter. A small round mirror, with two-axis tilt adjustment, turns the beam roughly 90 degrees into the interferometer. The entire interferometer can be positioned vertically with a single actuator. The beam combiner and compensator plate has two-axis tilt adjustment only. A three-axis translation stage controls the position of the reference fiber. The pupil imaging lens has no adjustments at all. Finally, the video detector array, onto which the secondary mirror is imaged, is mounted on a three-axis translation stage. Table 3.4 lists the major shimulator optical elements with the possible adjustments used to control their position. In some cases, more that one adjustment can control a particular motion; in that case, I have listed the most convenient adjustment.

3.4 Shimulator Alignment

The term *alignment* refers to setting the distances between the optical elements, adjusting their transverse positions, and adjusting their tilt with respect to the optical axis. In this section, I give a general overview of the techniques that were developed and implemented to align the shimulator. Appendix A presents a specific

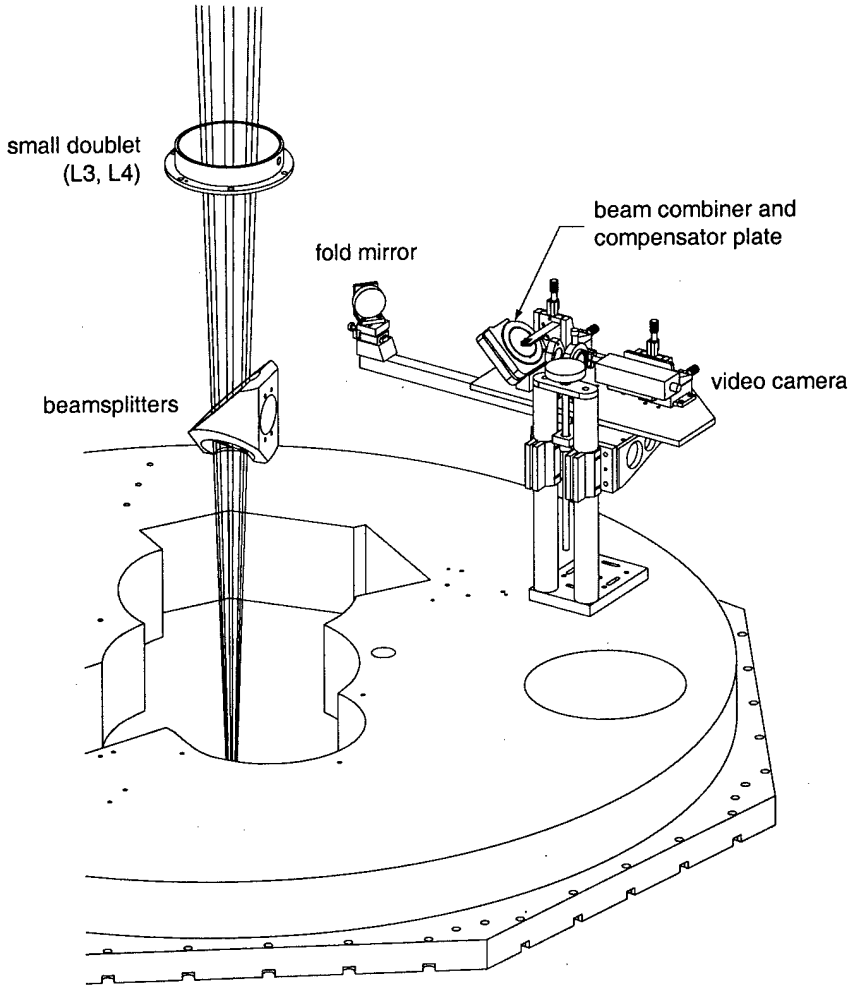

Figure 3.11 Drawing showing the phase-shifting interferometer in the top-box.

component	symbol	translation	tilt
secondary mirror	M2	hexapod x y z	hexapod
large lenses	L1, L2	screws x y	threaded rod +z
large fold mirror	F1	–	μm +z
small fold mirror	F2	–	screws +z
small doublet	L3, L4	stage, μm x y z	fs
beamsplitters	B1, B2	stage, μm z	fs
source table	ST	stage, μm x z	–
hologram	CGH	–	gimbal, fs
turb. generator	TG1, TG2	rail, clamp z	–
fiber, neg. lens	–	stage, fs x y z	–
interferometer	PSI	stage, screw y	–
fold mirror	PSIF1	–	fs
field mask	–	fs x y	–
beam combiner	PSIB1	–	fs
reference fiber	–	fs x y z	–
pupil lens	PSIL1	–	–
video detector	–	fs x y z	–

Table 3.4 Adjustments used to position the shimulator optical elements. For each element, the method of adjustment is listed with the axes which are controlled. A dash indicates that adjustment is not available. Abbreviations: μm = micrometer, fs = fine thread screw, usually with 80 threads per inch. In the top-box, the x-axis is parallel to the optical bed.

procedure to follow to align the shimulator; this section describes how that procedure evolved. Specific optical design parameters and tolerances, and measurements of optical characteristics are also listed in Appendix A.

Before aligning the shimulator, the first step was to characterize the first-order properties of the optical elements. Once the optical elements were reasonably characterized, the optical model used in the design phase was updated to calculate new spacings for the elements. The index of refraction and the curvature of the refractive elements determine their first-order properties: focal length and cardinal points. The surface accuracy of reflective optical elements is especially important; poor accuracy in a mirror will have roughly four times the effect on wavefront error as poor accuracy in a refractive element. For both the large 70 cm lenses (L1, L2) and the smaller doublet (L3, L4), I obtained melt data, supplied by the glass manufacturer, to determine the refractive index. Since L1 and L2 were fabricated at the Steward Observatory Mirror Laboratory, figuring data were available. From notes taken on test plate measurements, the radii of curvature of the L1 and L2 surfaces were estimated to be close to the upper limit of the design tolerance. The smaller doublet was fabricated by a commercial facility and test data were not available. Thus, its focal length was carefully measured using a phase-shifting interferometer. The procedure followed was the same procedure used to measure the back focal length of the wavefront sensor collimating lens, detailed in Section 2.5. The measured back focal distance was 0.4 mm longer than the designed back focal length of 523.3 mm. Other than the secondary mirror, these are the only major shimulator elements with curved surfaces.

Next, I incorporated these measurements into the original optical design to update the nominal spacings between the elements. I used optical analysis software to optimize the updated design to minimize the RMS wavefront error and pupil-

spacing	nominal (mm)	change (mm)	Δfocus (mm)	f/#	ΔW (waves)	Z_{11} (waves)	Z_{22} (waves)
M2–L1	25.7	−0.5	28.9	15.6	0.12	0.27	−0.013
L2–L3	8075.6	−1.0	4.3	15.1	0.08	−0.17	−0.021
CGH–B1	143.6	−0.5	1.2	15.3	0.44	−0.82	−0.690
nominal			0	15.0	0.01	−0.01	−0.015

Table 3.5 Tolerance analysis on shimulator element spacing. ΔW = RMS wavefront error in waves at 594 nm, Z_{11} = third-order spherical aberration, Z_{22} = fifth-order spherical aberration.

mapping error. The effects of varying the element spacings were then modeled to determine the tolerances on the spacings. Table 3.5 lists the effect of allowing three of the spacings to vary by small amounts. I estimate the spacings were actually set to within half the deviation listed in the table. As shown in Section 2.4, the f-number of the shimulator beam determines the size of the pupil image. As expected, my analysis showed the spacing between the secondary mirror (M2) and the large lenses (L1) has a strong influence on the f-number, thus an error in this spacing can lead to pupil-mapping errors. Also, I found the placement of the computer-generated hologram has a large effect on shimulator imaging performance. R. Sarlot conducted a similar analysis to determine the tolerances on de-centering and tilting the optical elements.[48]

After the spacings and tolerances were determined, the actual alignment of the shimulator could begin. The process was divided into several phases:

1. Install the secondary mirror and the large lenses in the shimulator tower; center them and set their spacings.
2. Adjust the tilt of the large fold mirrors so the physical axis of the top-box is roughly aligned to the secondary.

3. Use an alignment telescope to locate and adjust the optical axis of the secondary mirror and large lenses.
4. Measure and set the distance between the large lenses and the mount for the smaller doublet using a theodolite.
5. Use the alignment telescope to place the smaller doublet on the optical axis.
6. Assemble and align the source fiber and computer-generated hologram on the source table; align the source table to the optical axis using special alignment marks generated by the hologram.
7. Use the phase-shifting interferometer to fine-tune the CGH spacing and the alignment of the secondary mirror.

These steps provide a rough outline of the alignment process. The last step is repeated occasionally, as thermal fluctuations, among other phenomena, require the tilts of some of the elements be adjusted to compensate.

3.5 Shimulator Performance

As mentioned above, the two primary measures of shimulator performance are wavefront error and pupil-mapping accuracy. For the adaptive optics system to operate, the mapping of the secondary mirror onto the pupil formed on the wavefront sensor lenslet array must be accurate. The phase-shifting interferometer was used to evaluate both of these measures. Figure 3.12 shows a wavefront measured by the interferometer, while Table 3.6 lists the first few Zernike coefficients for the shimulator wavefront. The RMS wavefront error is 0.72 waves at 594 nm wavelength with a peak-to-valley error of 4.1 waves. Tilt and defocus were removed as they are determined by the position of the reference fiber. Similarly, coma is determined by the tilt of the aspheric secondary mirror. With coma removed, the RMS wavefront error is is réduced slightly to 0.70 waves at 594 nm wavelength.

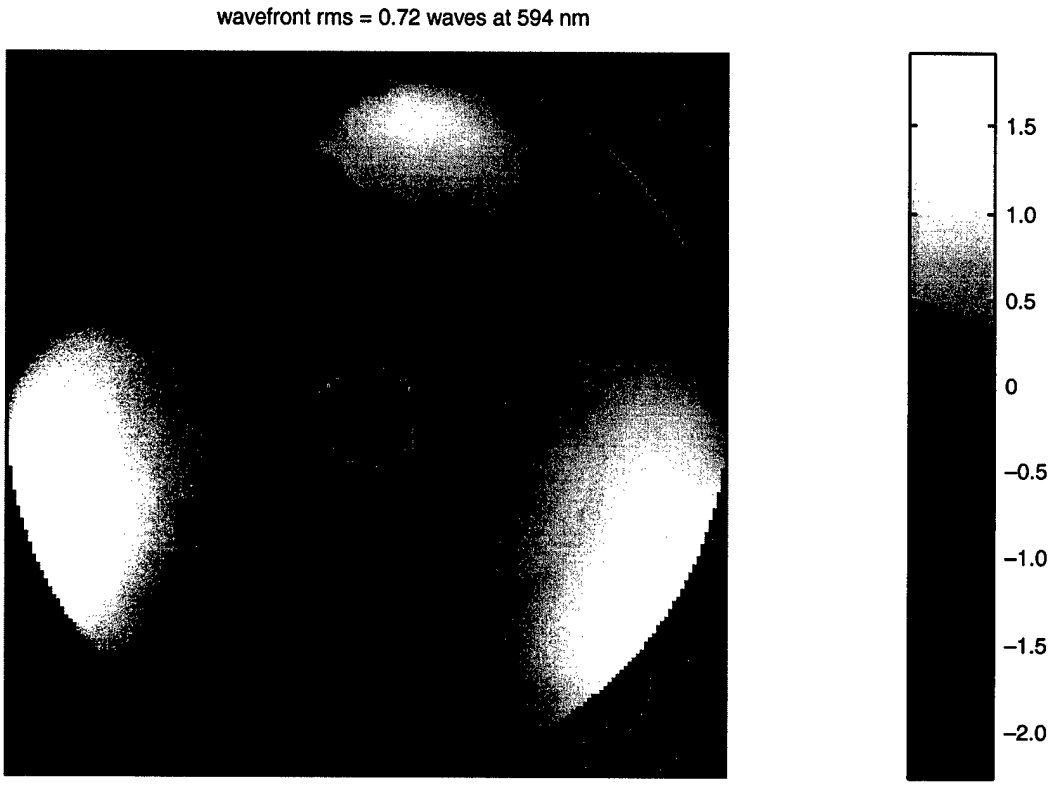

Figure 3.12 Shimulator wavefront measured by the phase-shifting interferometer. Units are waves at 594 nm wavelength.

coefficient	polynomial	name
−50.3	$r^2 \sin(2\theta)$	astigmatism
110.0	$r^2 \cos(2\theta)$	astigmatism
−83.0	$(3r^3 - 2r) \sin(\theta)$	coma
−8.6	$(3r^3 - 2r) \cos(\theta)$	coma
−177.8	$r^3 \sin(3\theta)$	trifoil
−95.4	$r^3 \cos(3\theta)$	trifoil
−90.6	$6r^4 - 6r^2 + 1$	3rd order spherical
−17.6	$(4r^4 - 3r^2) \cos(2\theta)$	
39.9	$(4r^4 - 3r^2) \sin(2\theta)$	
5.6	$r^4 \cos(4\theta)$	
12.7	$r^4 \sin(4\theta)$	
6.0	$(10r^5 - 12r^3 + 3r) \cos(\theta)$	
−71.8	$(10r^5 - 12r^3 + 3r) \sin(\theta)$	
5.7	$(5r^5 - 4r^3) \cos(3\theta)$	
34.6	$(5r^5 - 4r^3) \sin(3\theta)$	
5.2	$r^5 \cos(5\theta)$	
3.9	$r^5 \sin(5\theta)$	
−41.1	$20r^6 - 30r^4 + 12r^2 - 1$	5th order spherical

Table 3.6 Zernike coefficients of the shimulator wavefront measured by the phase-shifting interferometer. Tilt and defocus are not shown. Units are nanometers, normalized to unit RMS. Relative to the top-box, the y-axis is vertical and the x-axis is horizontal, θ is measured from the x-axis, increasing counterclockwise. The RMS wavefront error was 425 nm.

The RMS wavefront error of 425 nm corresponds to an image size of about 3 times the diffraction limit. By far, the dominant aberration is trifoil, with a significant amount of astigmatism. According to computer modeling and intuition, trifoil is probably not an error of alignment; rather, it is more likely due to a surface figure error in a reflective element. The figure error could have been caused by insufficient support in mounting or by improper figuring during manufacture. To investigate, analysis of the self-weight deflection of the three large mirrors was performed.[17] The analysis showed the large amount of trifoil probably was not caused by self-weight deflection. A likely culprit is one of the thin beamsplitters. Since both the wavefront sensor and the phase-shifting interferometer see roughly the same trifoil, the upper beamsplitter (B1) is possibly the cause. When time permits, it should be removed from the system and tested. If the trifoil is removed, the RMS wavefront error becomes 375 nm which corresponds to 2.5 times the diffraction-limited imaging performance.

The relatively small amount of coma can be eliminated by carefully adjusting the tilt of the secondary mirror. The presence of third- and fifth-order spherical aberration suggests the spacing between the CGH and the smaller doublet was slightly in error. Indeed, careful measurement of the distance, using inside micrometers, showed it was about 0.5 mm too short.[49] According to the results of the tolerance analysis shown in Table 3.5, this spacing error accounts for the observed spherical aberration and more. At least, the signs and relative magnitudes of the two spherical aberration coefficients match the prediction for the CGH to L4 spacing.

To measure pupil distortion, I placed small temporary markers on the surface of the secondary mirror at 50.8 mm (2 inch) intervals. Two rows of paper markers, or fiducial marks, were attached across the mirror diameter in a cross pattern. The commercial software used to reduce the interferometer data has the provision to

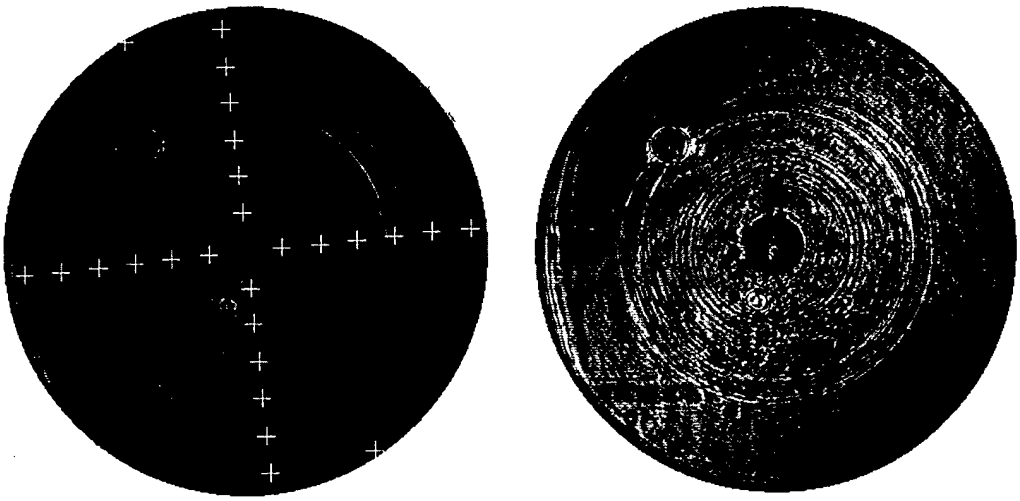

Figure 3.13 Secondary mirror fiducial marks as seen by the phase-shifting interferometer. The crosses in the image on the left-hand side show measured locations of the fiducial marks. The crosses were eliminated from image on the right-hand side so the fiducial marks can be seen.

calculate the fringe modulation in the image as the phase is shifted. Naturally, the fringe modulation is zero at the opaque markers. Figure 3.13 shows an intensity map of the modulation over the secondary mirror. The fiducial marks are clearly visible, at least in false-color on a computer monitor, as areas of low modulation. I mapped the coordinates of the marks and compared them to their known placement. The mapping error as a function of radial position is shown in Figure 3.14.

The bulk of the error was linear with radial position. This suggests an overall pupil scaling error, most likely due to inaccurately sizing the pupil in my analysis, not on the interferometer detector. The difference in slope suggests the aspect ratio of the interferogram may have been in error. The aspect ratio of the detector array was supplied to the interferogram analysis software based on data from the video camera manufacturer; it should be verified before suspecting an optical pupil distortion. When these overall scaling errors are removed, as shown in Figure 3.15, the residual mapping error is 1.1 mm RMS on the secondary mirror. The maximum allowed

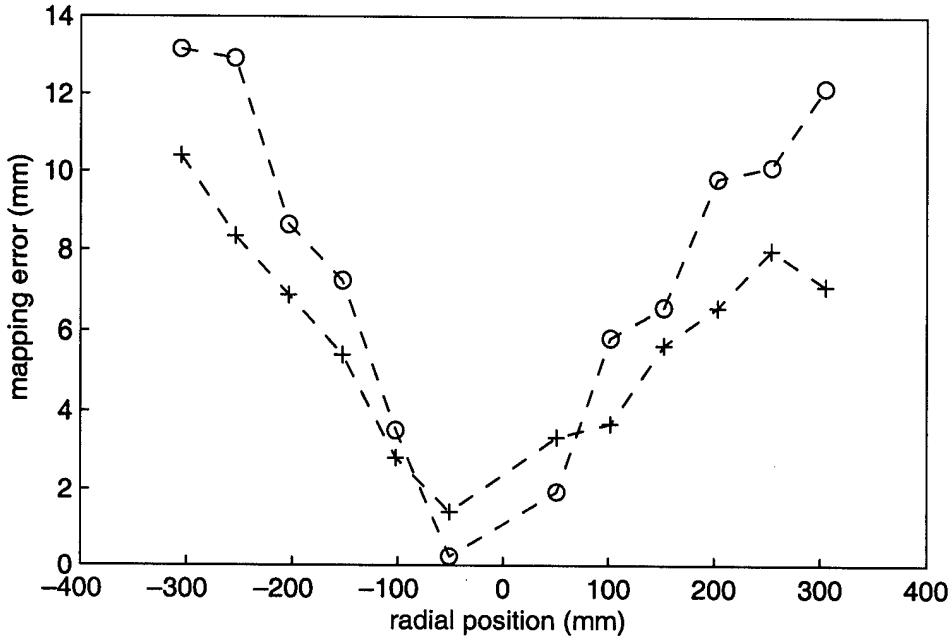

Figure 3.14 Pupil-mapping error as a function of radial position on the secondary mirror.

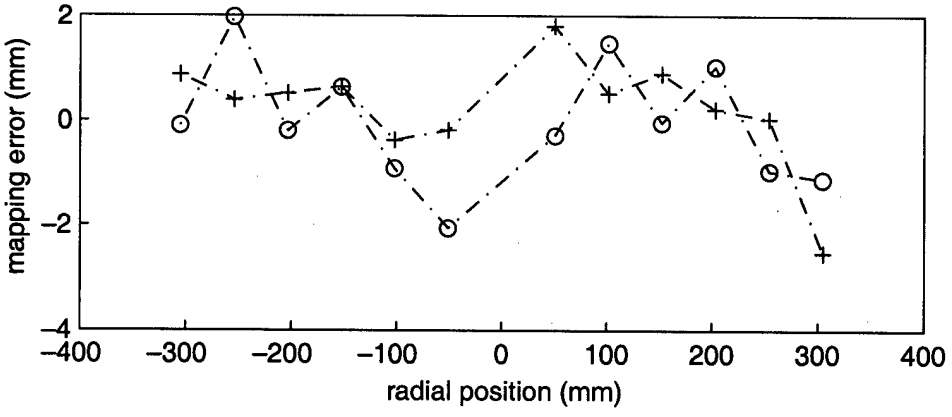

Figure 3.15 Pupil-mapping error after removing overall scaling error.

mapping error of 2 mm was slightly exceeded for only two of the fiducial marks. This analysis shows that, other than overall pupil scaling, the residual mapping errors of the shimulator are acceptable. The next step should be to measure the mapping error at the wavefront sensor. One possible method is to scan a light-emitting diode across the mirror while monitoring the illumination in each subaperture of the wavefront sensor.[50] The diode position could then be correlated with changes in the total illumination in a given subaperture. This method would provide a robust means of measuring the pupil mapping error of the entire optical path.

CHAPTER 4

WAVEFRONT SENSOR CALIBRATION AND TESTING

4.1 Introduction

This chapter presents work to calibrate optical path measurements made with the 6.5 m Multiple Mirror Telescope (MMT) adaptive optics system and its Shack-Hartmann wavefront sensor. The measurements were made using an adaptive optics test tower, called the *shimulator*, at the Steward Observatory Mirror Laboratory. The 6.5 m MMT adaptive optics system is described in Chapter 2. The role of the shimulator in testing the adaptive optics system is given in Chapter 3. My goal in this investigation was to compare wavefronts reconstructed from measurements made by the wavefront sensor with wavefronts obtained using a phase shifting interferometer. This comparison would confirm the performance of the top-box, help in the development of wavefront reconstruction algorithms, and, most importantly, validate the operation of the wavefront sensor in the presence of simulated atmospheric turbulence.

By introducing known tilts to the optical path, the response of the wavefront sen-

sor, or transfer function, was calibrated. The transfer function gave the relationship between spot displacement and local slope over each subaperture. Next, I measured spot displacements, or centroids, for highly-aberrated wavefronts. From the centroids, wavefronts were estimated using a modal least-squares reconstructor.[51] I developed the reconstructor by modeling the response of the wavefront sensor to a set of modal wavefront inputs. An accurate theoretical model of the wavefront sensor was developed by taking a *wave-optics* approach, as opposed to the usual geometric optics approach.[52] A wave-optics analysis includes significant diffraction effects not modeled by the geometric optics approach. Furthermore, the wave-optics approach can be extended to allow measurement of wavefronts with large aberrations, even where the wavefront distortions exceed the conventional dynamic range of the wavefront sensor.[53] I used this reconstructor to estimate wavefronts from the centroid measurements.

The reconstructed wavefronts were then compared with wavefronts measured by the phase-shifting interferometer. To improve the comparison, I measured the aberrations arising from optical elements unique to the path of the wavefront sensor, that is, the top-box optics. The root-mean-square (RMS) wavefront error from the entire top-box optical path was less than 70 nm. The effects of these non-common path aberrations were subtracted from the wavefront sensor measurements; the corrected results were then compared with the phase-shifting interferometer wavefronts. The wavefront measurement process is illustrated in Figure 4.1; the details are explained in the sections that follow.

4.2 Wavefront Sensor Calibration

As explained in Section 2.5, the Shack-Hartmann wavefront sensor divides the telescope pupil into a two-dimensional array of subapertures. The local wavefront slope

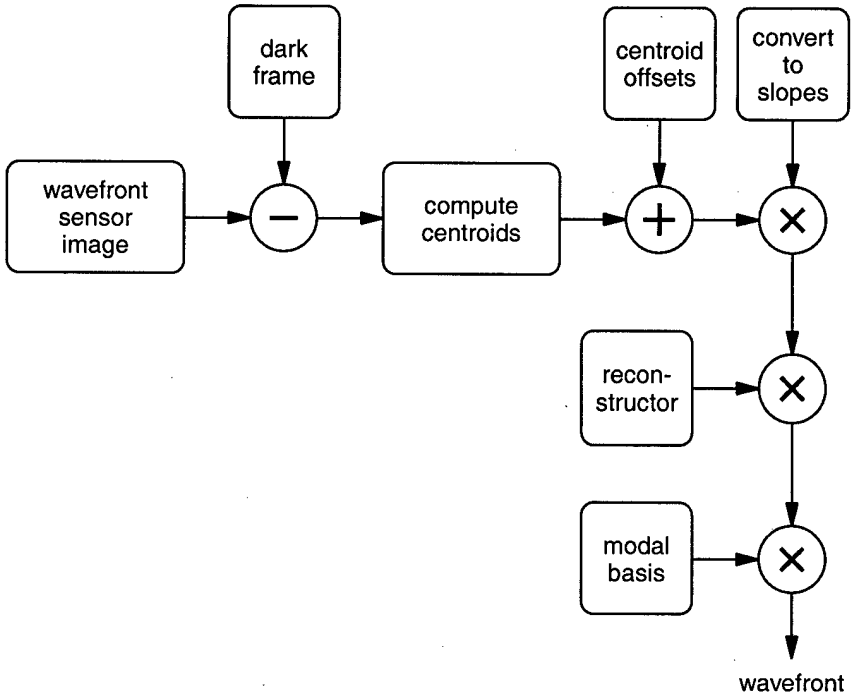

Figure 4.1 Block diagram of the wavefront sensor measurement process.

over each subaperture was measured by observing the displacement of images of the reference source on the detector array. When the digitized images from the detector array are used to reconstruct wavefronts, four steps are performed:

1. subtract dark frame,
2. calculate centroids,
3. apply offsets to centroids,
4. convert to wavefront slopes.

The following sections describe the measurements I made to calibrate the wavefront sensor response. These measurements were used in the steps listed above to reconstruct wavefronts from wavefront sensor images.

4.2.1 Dark Frame Subtraction

Subtracting the dark frame removed the fixed pattern of noise, from read noise and stray light,[†] on the detector array. The dark frame was collected by blocking the reference source, then collecting and averaging 64 wavefront sensor images. A new dark frame was collected whenever the integration time or the ambient illumination changed, and at the beginning of a data collection session. Of course, the dark frame did not correct for stray light from the reference source scattered from surfaces within the shimulator. Furthermore, flat-field correction was not applied to correct for the quantum efficiency of the pixels, nor to correct for the gain of the amplifiers. As mentioned earlier, the lenslet array is permanently bonded to the detector package, making uniform illumination of the detector array difficult. Although noise would have been less at lower temperature, the detector was operated at room temperature. When operated at $-70°C$, the read noise of 3–6 electrons per pixel dominates other noise sources.[54] At 20°C, the dark signal is 10^4 electrons per pixel per second. For a 75 ms integration time, this corresponds to 750 electrons; which is much less than the 3×10^5 electron per pixel well depth. Thus, the signal performance was limited by photon-noise, not by the dark signal. Ample light was available from the 2 mW laser to fill the pixel wells while keeping the exposure time short. Neutral density filters were used to prevent saturation of the detector array.

4.2.2 Centroid Calculation

After the dark frame was subtracted, centroids were calculated for each subaperture, denoted k, by weighting the counts in each pixel of the sub-array by its distance from the center of the sub-array. Centroids, $\vec{x}_k$, are vectors given by

[†]Although the shimulator was covered with sheets of black plastic to control stray light, not all of the stray light could be eliminated.

$$\vec{x}_k = \frac{\sum_{n=1}^{N} c_n x_n}{\sum_{n=1}^{N} c_n} \hat{u}_x + \frac{\sum_{n=1}^{N} c_n y_n}{\sum_{n=1}^{N} c_n} \hat{u}_y \tag{4.1}$$

where N is the number of pixels in the sub-array of subaperture k, c_n is the number of counts for the nth pixel, x_n is the x-distance of the nth pixel from the center of the sub-array, and $\hat{u}_x$ is a unit vector in the direction of the x-axis. Recall that the detector array is divided into sub-arrays, each 6×6 pixels. When the wavefront sensor is used to operate the adaptive optics system, the sub-arrays are binned, on the detector chip, into 2×2 quad-cells. Thus the clock rate can be reduced by 9 times, keeping the read-out time the same. Because the read noise is proportional to the clock rate, reducing the clock rate reduces the read noise by the same factor. Since I was interested in accurately measuring highly aberrated wavefronts, the sub-arrays were not binned. Binning reduces the dynamic range of slopes measurements.

The first two steps in the calibration process, dark subtraction and centroid computation, are illustrated in Figure 4.2. Note the dark frame, Figure (a), in which each of the detector quadrants displays a different overall intensity level. The quadrants of the detector are transferred to separate storage areas, then passed to separate amplifiers, each with a different gain. This caused the quadrant pattern that appears in the dark frame. There is also a gradient, within each quadrant, in the read-out direction. The maximum intensity in Figure (b) is about 3.3×10^4 counts; the digitizer has 15-bits of resolution, or 32,768 levels. The reference source intensity and detector integration time were adjusted so that the digitizer was near saturation for the pixels with the highest intensity. This maximizes the signal-to-noise ratio without the added complexity of cooling the detector. The centroids, shown in Figure 4.2 (d), were calculated according to equation (4.1). The average centroid displacement was 8.4 μm and the largest displacement was 28.8 μm.

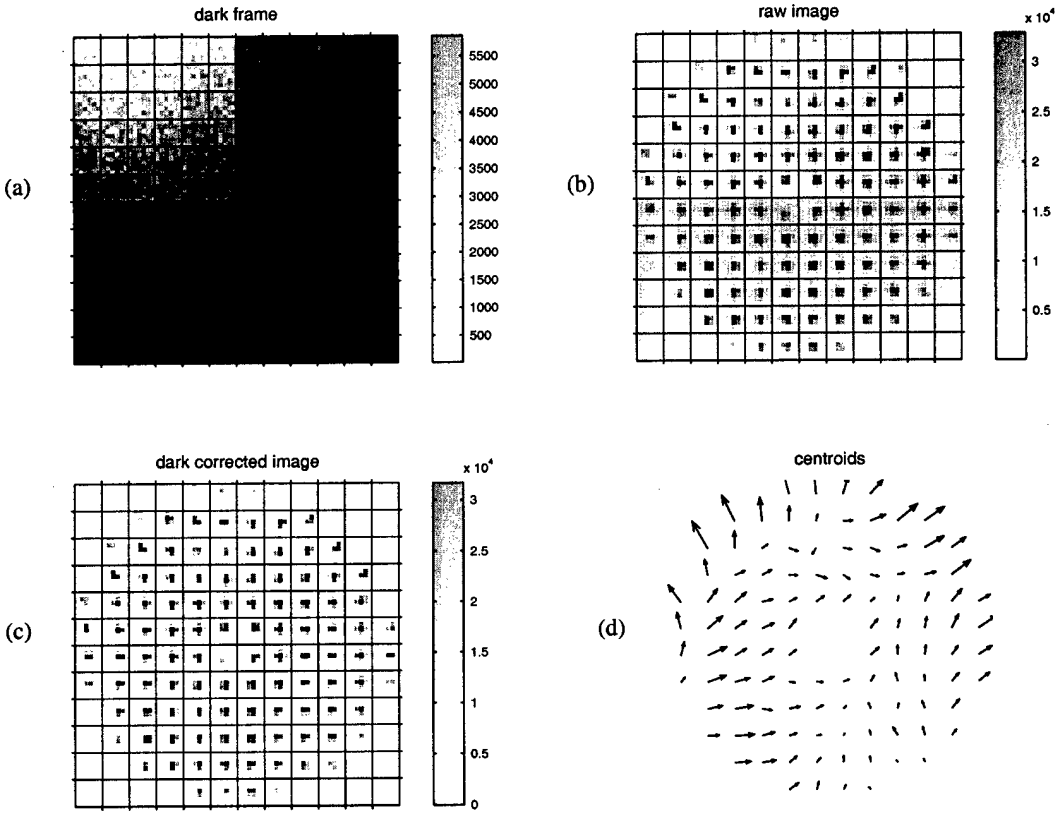

Figure 4.2 Dark subtraction and centroid calculation. Only the central 72×72 pixels of the wavefront sensor detector array are shown; the 6×6 pixel sub-array boundaries are marked with black lines. The units are 15-bit digitizer counts. The integration time was 75 ms. Figure (a) shows the average dark frame, Figure (b) shows the unprocessed image, Figure (c) shows the dark corrected image, and Figure (d) shows the centroids. The average centroid displacement was 8.4 μm (0.35 pixels) and the longest was 28.8 μm (1.2 pixels).

4.2.3 Centroid Offset Measurement

The third step in the wavefront sensor calibration process was to measure centroid offsets. The offsets were due to the optical elements that were not part of the common path the wavefront sensor shared with the phase-shifting interferometer. These elements include the top-box mirrors, the collimating lens at the front of the wavefront sensor, and the lenslet array. When the adaptive optics system is installed on the telescope, the same corrections should be applied, for the top-box optical elements are not shared with the imaging sensor. These non-common path elements introduce small aberrations which are seen only by the wavefront sensor—not by the other instruments. The offsets need only be updated when the optical elements are moved or if they drift over time.

To measure the offsets, I sent a spherical wavefront through the top-box to the wavefront sensor, where centroids were measured. The spherical wavefront was provided by coupling laser light into a single-mode optical fiber. Its 5 μm diameter fiber core acted essentially as a point source. First, the fiber was placed at the $f/15$ focus, upstream of the mirror that folds light into the plane of the top-box. The fiber was positioned by observing light scattered back to the fiber from the wavefront sensor detector. Recall, the detector lies at the focal plane of the lenslet array. Although the silicon detector has an anti-reflection coating, its reflectivity is at a least few percent.[54,55] Light from the array of images formed by the lenslets was reflected back, from the detector, through the lenslets. This light passed back through the top-box to form an array of images of the fiber in the plane of the fiber. The specular reflection from the detector array formed a single bright image of the fiber; the scattered light from the detector array formed an array of less bright images of the fiber. I adjusted the transverse position of the fiber by centering the bright reflected image on the end of the fiber. To make fine adjustments of the fiber

alignment, I eliminated the tilt and defocus measured with the wavefront sensor.

After the fiber alignment, 16 wavefront sensor images were recorded, averaged, and dark adjusted. I then calculated centroid offsets and reconstructed the wavefront using the least-squares reconstructor discussed in Section 4.3. The resulting wavefront sensor image and centroids offsets are shown in Figure 4.3, along with an image of the reconstructed wavefront. The first few Zernike coefficients are listed in Table 4.1. I calculated the RMS wavefront error to be 68 nm; the dominant aberrations were astigmatism and coma. Some of this error can be attributed to surface irregularities of the top-box mirrors. Table 4.2 lists the approximate surface errors of the three mirrors.[23] When combined in quadrature, the total wavefront error from the mirrors was 36 nm RMS. Another source of the centroid offsets was slight misalignment between the lenslet array and the detector array. This misalignment could be caused, in part, by irregularities in the arrangement of detector and lenslet elements. Minute positioning errors while bonding the lenslet array to the detector package may also contribute to the centroid offsets. The alignment was measured in the laboratory, yielding a residual wavefront error of 27 nm.[28] This adds to the wavefront error from the mirrors to yield 45 nm RMS, leaving about 50 nm RMS to other sources. These sources include intentional misalignment of the top-box optical elements to adjust pupil position at the wavefront sensor and accidental misalignment.

The exact source of the centroid offsets is not important, as long as the offsets are small compared with the range of slopes that can be measured by the wavefront sensor using binned pixels. If these offsets are accurately measured and remain relatively stable in time, their effects can be reliably eliminated. After the centroids are calculated, the offsets are merely subtracted. To yield a final estimate of the local wavefront slope over a subaperture, the corrected centroids are converted to

(a)

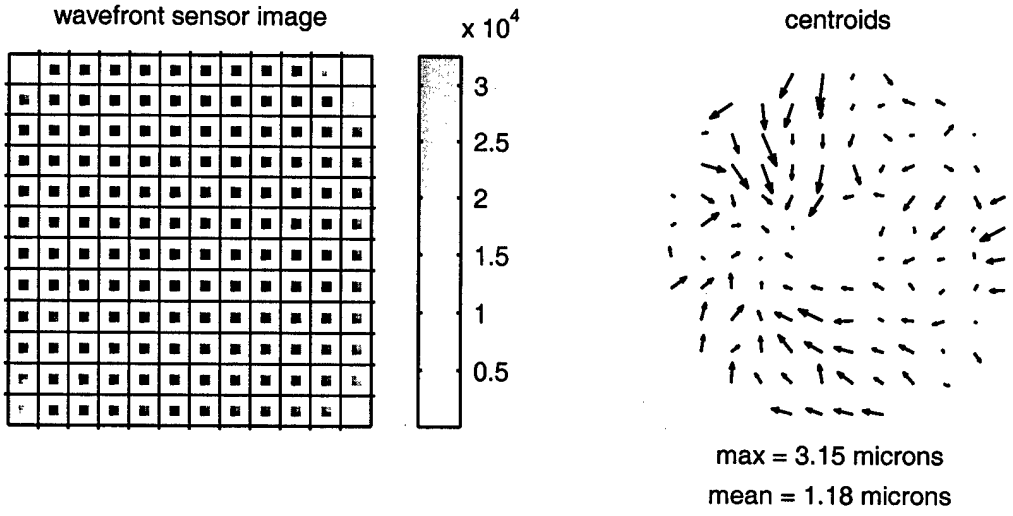

(b)

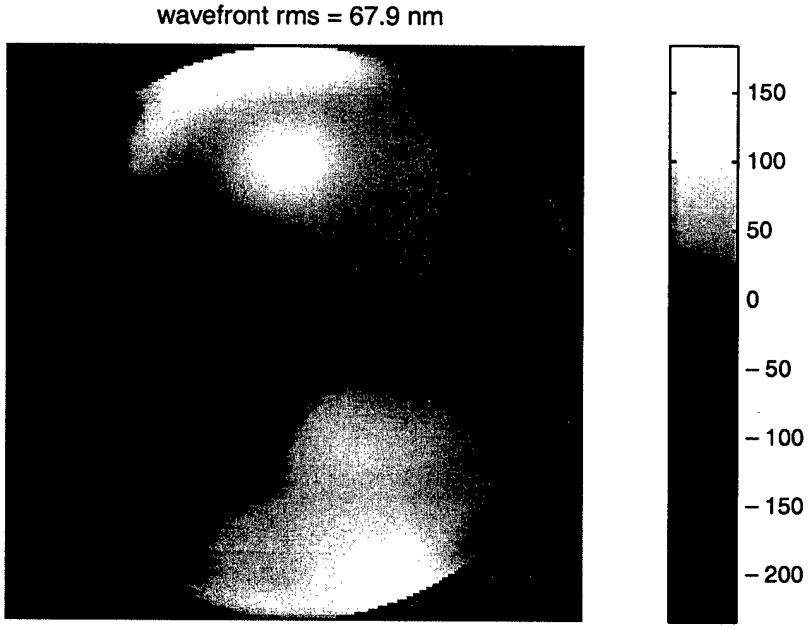

Figure 4.3 Wavefront sensor image and wavefront error for aberrations measured using a fiber at the $f/15$ focus. Figure (a) shows the dark corrected image and the centroids. Figure (b) shows the wavefront reconstructed from the centroids; the units are nanometers.

coefficient	polynomial
13.0	$r^2 \sin(2\theta)$
−55.2	$r^2 \cos(2\theta)$
25.2	$(3r^3 - 2r) \sin(\theta)$
−1.7	$(3r^3 - 2r) \cos(\theta)$
−4.2	$r^3 \sin(3\theta)$
−5.5	$r^3 \cos(3\theta)$
8.4	$6r^4 - 6r^2 + 1$
8.7	$(4r^4 - 3r^2) \cos(2\theta)$
−0.2	$(4r^4 - 3r^2) \sin(2\theta)$
2.1	$r^4 \cos(4\theta)$
6.7	$r^4 \sin(4\theta)$
2.0	$(10r^5 - 12r^3 + 3r) \cos(\theta)$
−5.2	$(10r^5 - 12r^3 + 3r) \sin(\theta)$
0.4	$(5r^5 - 4r^3) \cos(3\theta)$
0.5	$(5r^5 - 4r^3) \sin(3\theta)$
−4.4	$r^5 \cos(5\theta)$
0.3	$r^5 \sin(5\theta)$

Table 4.1 Zernike coefficients for top-box aberrations measured using a fiber at the $f/15$ focus. Tip, tilt, and defocus are not shown. Units are nanometers, normalized to unit RMS. The y-axis is vertical and the x-axis is horizontal, θ is measured from the x-axis, increasing counter-clockwise. Total RMS wavefront error was 68 nm.

mirror[a]	surface (waves RMS)	wavefront (nm RMS)
OAP1	0.01	12.7
PSM	0.025	31.7
OAP2	0.01	12.7

[a] OAP = off-axis paraboloid
PSM = pupil-steering mirror

Table 4.2 Wavefront error from surface irregularities of the top-box mirrors. The surface figure of the paraboloids was measured.[23] The surface figure of the steering mirror was estimated from specifications. When added in quadrature, the total wavefront error for the mirrors is 36 nm RMS.

wavefront slopes, as described in the next section.

4.2.4 Centroid to Wavefront Slope Conversion

The final step in the wavefront sensor calibration process was to scale the centroid measurements to obtain slopes. The purpose of this step was to relate the response of the wavefront sensor to the local slope at each subaperture. From the centroid measurements $\vec{x}_k$, the local slope $\vec{s}_k$ of the wavefront is given by

$$\vec{s}_k = \frac{2\pi\,(\vec{w}_k \cdot \vec{x}_k)}{\lambda f_l} \tag{4.2}$$

where λ is the wavelength and f_l is the focal length of the lenslet. The weighting factor for each subaperture, $\vec{w}_k$, is ideally unity, however it can depend on the shape of the spots formed by the lenslets and their size in relation to the detector elements.[56] The weighting factor can be a linear multiplier or it can be a function of $\vec{x}_k$. These quantities are illustrated in Figure 4.4 where the geometry for a single lenslet is shown. The units of $\vec{s}_k$ in equation (4.2) are radians of phase per unit transverse distance.

Since slope calibration required the use of the electronically-actuated tip-tilt

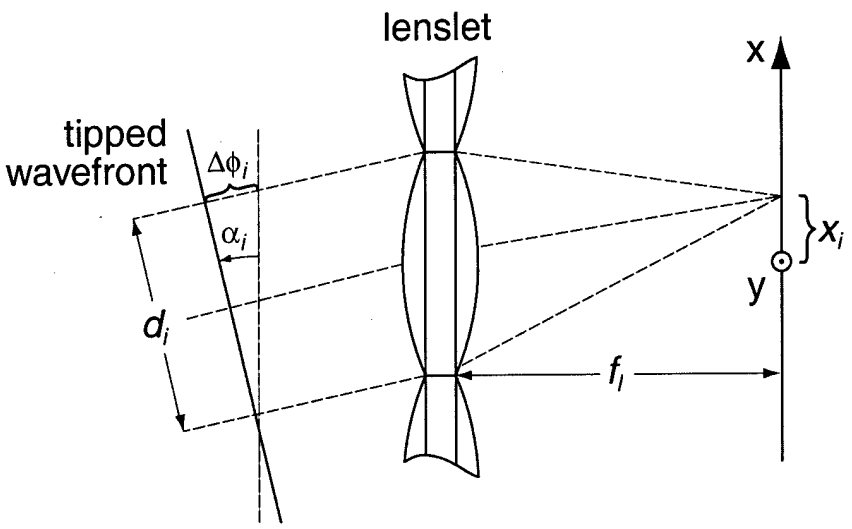

Figure 4.4 Geometry for a single subaperture. The view is of a single lenslet looking down the y-axis. The detector array is in the x-y plane.

mount for the pupil-steering mirror, its performance was evaluated. First, the relationship between mirror angle and actuator displacement was measured. The 5 cm lever arm of the mirror mount was designed to give about 1 degree of angle per millimeter of actuator travel. Since the mount had been modified to accommodate the oversized electronic actuators, I sought to verify this relationship. With the actuators near the center of their travel and the mirror angle set to zero, the actuators were individually moved. The actuators reported the relative movement to an accuracy of better than 1 μm.[20] As the actuators moved, the angle of the mirror was measured using a digital level. The angular movement was quite linear over the relatively small range which would be used. When the mirror mount was installed, however, some backlash or hysteresis was noted. To measure the backlash, I inserted a video detector array in the top-box, after the $f/23$ focus, in place of the wavefront sensor. The secondary mirror was imaged onto the detector using a collimating lens identical to that in the wavefront sensor.[‡] One of the mirror actuators was

[‡]These video images were later used to estimate the magnification of the secondary mirror on the lenslet array, as described in Section 2.6.

axis[a]	angular response	backlash
tip	1.1 deg/mm	7 μm
tilt	1.1 deg/mm	18 μm

[a] tip = rotation about axis parallel to top-box plane
tilt = rotation about axis perpendicular to top-box plane

Table 4.3 Angular response and backlash of pupil-steering mirror mount. Note that the mount was oriented 90 degrees from its intended orientation; this may have contributed to the backlash.

moved 100 μm in one direction; an image was digitized and the reported actuator position was recorded. Then the actuator was moved again 100 μm in the same direction. Next, the actuator was commanded to move in the opposite direction until the *image* reached the same position as was digitized before. The difference in the positions reported by the actuator yielded the backlash in that axis. The process was repeated for the other actuator. The backlash for each axis, along with the angular response, is listed in Table 4.3. This amount of backlash was problematic, for according to equation (4.2), 10 μm of movement at the pupil-steering mirror corresponds to 22 μm of centroid displacement. To avoid backlash, the mirror angle was changed by only driving the actuators in one direction.

Having characterized the performance of the pupil-steering mirror mount, I could proceed with the wavefront sensor slope calibration. A reasonably planar wavefront[§] was passed from the shimulator to the top-box. I adjusted the pupil-steering mirror, while being mindful of mirror backlash, to minimize overall tilt as measured by the wavefront sensor. This left the spots approximately in the center of their sub-arrays. One mirror actuator was moved to bring the spots half-way to the edge of their sub-arrays. Next, that actuator was commanded to make 10 steps of 2 μm

[§]The RMS error in the wavefront generated by the shimulator was 400 nm.

in the opposite direction; centroids were measured at each step. After that, the overall tilt was again minimized, and the process was repeated for the other mirror actuator.

The change in slope introduced to the wavefront for each actuator step can be found as follows. The quantity $\vec{x}_k/f_l$ in equation (4.2) is equal to the angle α_k in Figure 4.4. Now, for small angles, $\alpha_k \propto \Delta\phi_k/d_k$ where $\Delta\phi_k$ is the phase at the edge of the subaperture k and d_k is the width of the subaperture, 144 μm. Since there are 6 subapertures per pupil radius, $\Delta\phi_k = \Delta\phi_p/6$, where $\Delta\phi_p$ is the change in phase at the edge of the pupil introduced by the mirror. Again, for small angles $\Delta\phi_p \propto \alpha_p d_p$, where α_p is the angle of the pupil-steering mirror and d_p is the diameter of the pupil at the mirror, about 56 mm. This gives the change in slope for an actuator movement

$$\delta s = \frac{2\pi}{\lambda}\alpha_k = \frac{2\pi}{\lambda}\frac{\alpha_p d_p}{6\, d_k} \tag{4.3}$$

where α_p is the angular response of the mirror mount given in Table 4.3. For a 2 μm actuator movement, the change in wavefront slope at the lenslet array is about 0.0272 rad/μm.[¶] By measuring the average centroid displacement for each of the slope changes introduced by the pupil-steering mirror, the wavefront sensor slope response was calculated. Figure 4.5 shows the average centroid displacement for both axes as a function of wavefront slope. As one actuator of the mirror was moved, there were large centroid displacements in the corresponding axis of the wavefront sensor and small displacements in the other axis. This implies the axes of the mirror were not perfectly aligned with the axes of the wavefront sensor, or the gimbal axes were not perfectly orthogonal. A least-squares linear fit gives the

[¶]The expression for the slope introduced by the pupil-steering mirror is not exact. In the shimulator, a field lens is used at the $f/15$ focus to correct the pupil imaging in the top-box. Because the focal length of the field lens was 600 mm instead of the required 800 mm, the pupil-steering mirror was not exactly at a pupil of the system. Large mirror tilts introduced a small translation of the beam on the lenslet array.

(a)

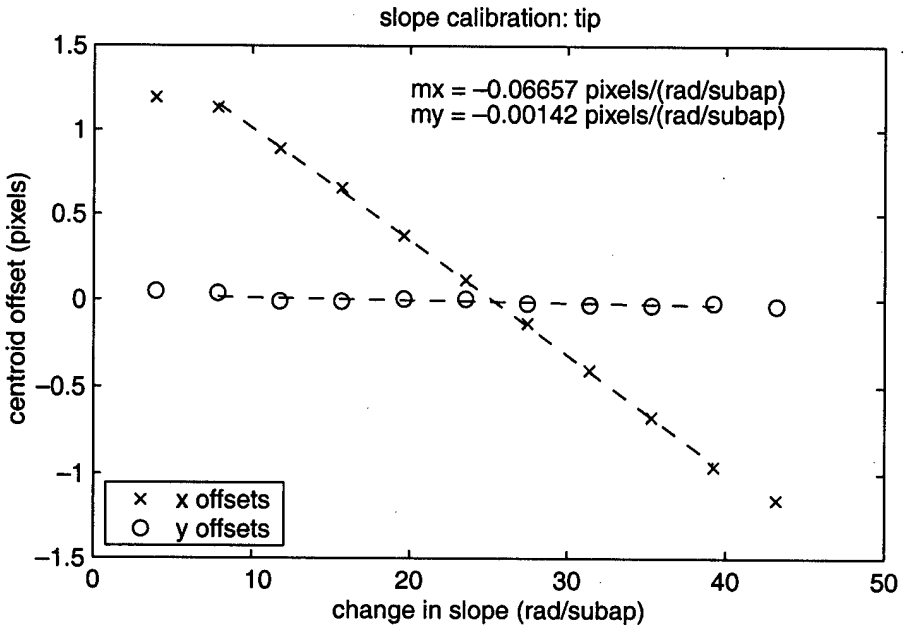

(b)

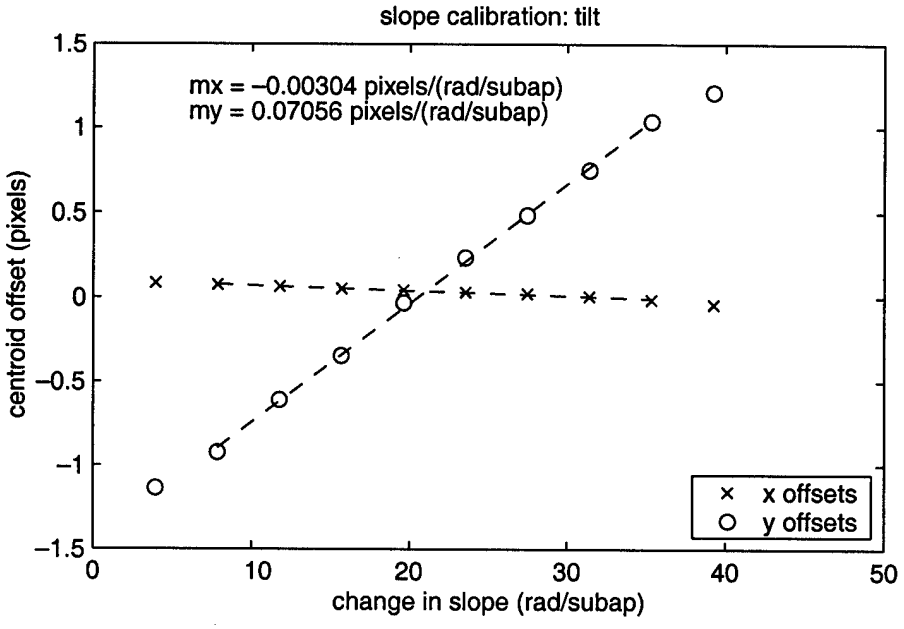

Figure 4.5 Average centroid displacement as a function of wavefront slope change introduced by the pupil-steering mirror. The dashed lines show a least-squares linear fit; the points at the slope extremes were not used.

average change in centroid for a change in slope, $\partial\vec{x}/\partial\vec{s}$. In fitting the points, I ignored the centroid offsets at the slope extremes, as the spots were not entirely contained within their sub-arrays. The two components of centroid motion were added in quadrature. The resulting value for $\partial\vec{x}/\partial\vec{s}$ was used in equation (4.2) to solve for the weighting factor

$$\vec{w} \approx 1.409\,\hat{u}_x + 1.328\,\hat{u}_y \tag{4.4}$$

which is the same for all subapertures. This agrees favorably with weighting factors of 1.33 and 1.34 reported by T. Rhoadarmer.[28] Given the adjusted and calibrated centroid displacements, the wavefront is reconstructed as described in the next section.

4.3 Wavefront Reconstruction Algorithm

Before the wavefront sensor measurements could be compared with phase-shifting interferometer measurements, an estimate of the original wavefront had to be reconstructed from the calibrated centroids. In this section, I describe my approach to developing a wavefront reconstructor. The process of wavefront reconstruction in the typical adaptive optics system involves converting wavefront slope or curvature measurements into commands that are applied to a wavefront corrector. My goal was slightly different—I wanted an accurate estimate of the wavefront to evaluate the performance of the wavefront sensing portion of the adaptive optics system. I chose to implement a modified least-squares reconstructor.[51,57,58] The least-squares reconstructor seeks to minimize the difference, or mean-square error, between the measured slopes and those that would be observed from a given set of modal wavefront inputs. The general technique is developed and discussed by Hardy.[56] A brief overview of the least-squares reconstruction technique is presented here, followed by a short description of my implementation of the modal reconstructor.

The goal here is to fit the slope measurements to an estimate of the wavefront by minimizing the mean-square error. The wavefront $\phi(x, y)$ may be expressed as an expansion of basis functions, or modes, defined over the telescope pupil

$$\phi(x, y) = \sum_{m=1}^{M} a_m Z_m(x, y) \tag{4.5}$$

where the a_m are the M coefficients, to be determined, and $Z_m(x, y)$ are the basis functions, which are orthogonal over the pupil. Since the basis functions are orthogonal, the coefficients a_m are mutually independent. It is convenient to choose Zernike polynomials for the $Z_m(x, y)$.[59] They have zero mean and can be normalized so their mean-square phase is

$$\sigma_\phi^2 = \sum_{m=1}^{M} a_m^2. \tag{4.6}$$

The x- and y-slopes are obtained by differentiating equation (4.5)

$$\begin{aligned} s^x(x, y) &= \frac{\partial}{\partial x} \phi(x, y) \\ s^y(x, y) &= \frac{\partial}{\partial y} \phi(x, y). \end{aligned} \tag{4.7}$$

In a Shack-Hartmann wavefront sensor, the slope is measured over distinct areas defined by each subaperture. This yields two vectors of slope measurements whose elements for each subaperture k, centered at coordinates (x_k, y_k), are given by

$$\begin{aligned} s_k^x &= \frac{\partial}{\partial x} \phi_k = \sum_{m=1}^{M} a_m \left[\frac{\partial}{\partial x} Z_m(x, y) \right] \Big|_{(x,y)=(x_k,y_k)} \\ s_k^y &= \frac{\partial}{\partial y} \phi_k = \sum_{m=1}^{M} a_m \left[\frac{\partial}{\partial y} Z_m(x, y) \right] \Big|_{(x,y)=(x_k,y_k)}. \end{aligned} \tag{4.8}$$

Equation (4.8) can be written in matrix form as

$$\mathbf{s} = \mathbf{D}\,\mathbf{a} \tag{4.9}$$

where $\mathbf{a}$ is the vector of Zernike coefficients, $\mathbf{D}$ is a matrix of derivatives of the Zernike basis functions, and $\mathbf{s}$ vector containing the measured x- and y-slopes. The vector of Zernike coefficients, $\mathbf{a}$, has M elements, $\mathbf{D}$ is a rectangular matrix with M columns and $2P$ rows, and the vector of x- and y-slopes, $\mathbf{s}$, has $2P$ elements. P is the number of subapertures in the pupil.

Recall, the goal is to find the coefficients $\mathbf{a}$, given the vector of slopes $\mathbf{s}$, by minimizing the difference $(\mathbf{s} - \mathbf{D}\,\mathbf{a})$. If we multiply equation (4.9) from the left by $\mathbf{D}^\dagger$ (the transpose of $\mathbf{D}$) we have the normal equation

$$(\mathbf{D}^\dagger\,\mathbf{D})\,\mathbf{a} = \mathbf{D}^\dagger\,\mathbf{s}. \tag{4.10}$$

The standard least-squares solution[60] is found by inverting $(\mathbf{D}^\dagger\,\mathbf{D})$ and multiplying to yield an estimate of the coefficients

$$\hat{\mathbf{a}}_{LS} = (\mathbf{D}^\dagger\,\mathbf{D})^{-1}\mathbf{D}^\dagger\,\mathbf{s}. \tag{4.11}$$

To implement the solution given in equation (4.11), several approaches are possible. First, a general approach is outlined, then a description of the particular method I implemented follows. For the chosen basis functions, the Zernike polynomials, the derivatives that make up $\mathbf{D}$ can be found analytically. The derivatives are evaluated at each subaperture, (x_k, y_k), and used to build $\mathbf{D}$. Alternatively, the complexity of finding analytic expressions for the gradients can be avoided by evaluating the derivatives of the Zernike polynomials numerically. Next, the least-squares solution, $(\mathbf{D}^\dagger\,\mathbf{D})^{-1}\mathbf{D}^\dagger$ is calculated. This solution and the measured slopes are inserted into equation (4.11) to find an estimate of the coefficients $\hat{\mathbf{a}}_{LS}$. Of course, the same solution is used repeatedly to estimate coefficients from the separate sets of slope measurements. Finally, by substituting the polynomial coefficients $\hat{\mathbf{a}}_{LS}$ into equation (4.5), one obtains an estimate of the wavefront. There are 108 subapertures; I used 99 modes. The sizes for the arrays in equation (4.11) are listed in Table 4.4.

array	$\hat{\mathbf{a}}_{LS}$	$(\mathbf{D}^\dagger\mathbf{D})^{-1}\mathbf{D}^\dagger$	$\mathbf{s}$
variable[a]	$M \times 1$	$M \times 2P$	$2P \times 1$
dimension[b]	99×1	99×216	216×1

[a] M = number of modes
P = number of subapertures
[b] rows × columns

Table 4.4 Dimensions of the arrays in equation (4.11).

To construct $\mathbf{D}$, I took a slightly different path. The intermediate step of converting centroids to slopes was eliminated by expressing $\mathbf{D}$ in terms of centroids instead of slopes. Centroids were then used to reconstruct a wavefront directly. This generalization was valid since, from equation (4.1), centroids and slopes bear a linear relationship. $\mathbf{D}$ became a matrix of centroids, instead of slopes, that resulted when each of the modal basis functions was processed by a theoretical model of the wavefront sensor. I developed my reconstructor by accurately modeling the response of the wavefront sensor by applying wave-optics techniques,[52] as opposed to familiar geometric optics methods.[21] The wave-optics analysis included important diffraction effects not modeled by geometric optics. This technique of modeling the wavefront sensor was adapted from an approach used by Roggemann and Schulz to extend the measurement capabilities of Shack-Hartmann wavefront sensors.[53] A short introduction to wave-optics analysis is presented below; the interested reader is encouraged to consult the references for a thorough treatment.

In wave-optics analysis, optical instruments are treated as linear, space-invariant systems.[52,60,61] The instruments are modeled using mathematical operators, denoted $\mathcal{S}\{\cdot\}$. Inputs to the optical instruments are cast as functions, $g_i(x_i, y_i)$. The set of input functions are mapped to a set of output functions, $g_o(x_o, y_o)$, by the

mathematical operators

$$g_o(x_o, y_o) = \mathcal{S}\{g_i(x_i, y_i)\}. \tag{4.12}$$

For example, the Shack-Hartmann wavefront sensor maps an input complex field amplitude at the lenslets to the output field amplitude at its detector. The effect of the individual components of the optical system can be characterized using separate mathematical operators that are applied to the input functions in succession. The output of a linear space-invariant system, at output coordinates (x_o, y_o), can be completely characterized by its response, h, to an impulse or delta function, denoted δ, at input coordinates (x_i, y_i)

$$h(x_o, y_o; x_i, y_i) = \mathcal{S}\{\delta(x_i, y_i)\}. \tag{4.13}$$

The function h is called the impulse response or point-spread function. For a space-invariant system, the output is given by the convolution of the input function with the impulse response

$$g_o(x_o, y_o) = \iint_{-\infty}^{\infty} g_i(x_i, y_i)\, h(x_o - x_i, y_o - y_i)\, dx_i\, dy_i. \tag{4.14}$$

The convolution integral is written more compactly as

$$g_o = g_i \otimes h \tag{4.15}$$

where $\otimes$ indicates that g_i and h are convolved to yield g_o. The cumbersome convolution integral becomes a simple multiplication in the frequency or Fourier domain

$$G_o(f_x, f_y) = H(f_x, f_y)\, G_i(f_x, f_y) \tag{4.16}$$

where the capital letters represent the Fourier transform of their respective functions. For example, the Fourier transform of the impulse response function is written

$$H(f_x, f_y) = \iint_{-\infty}^{\infty} h(x_i, y_i)\, \exp[-j\, 2\pi(f_x\, x_i + f_y\, y_i)]\, dx_i\, dy_i. \tag{4.17}$$

The function $H(f_x, f_y)$ is known as the transfer function of the system. The output of the system is found by computing the Fourier transform of the input function, multiplying by the transfer function, and computing the inverse Fourier transform of the product. The Fourier transform operation is written $\mathcal{F}\{\cdot\}$ and the inverse Fourier transform is written $\mathcal{F}^{-1}\{\cdot\}$; thus, $H = \mathcal{F}\{h\}$ and $h = \mathcal{F}^{-1}\{H\}$. Working in the frequency domain can greatly simplify the analysis of optical systems. For example, under certain limitations, the far-field diffraction pattern from an aperture is simply given by the Fourier transform of the aperture function.[61]

The mathematics of scalar diffraction theory can be recast onto this framework of linear, space-invariant systems. The concept of the angular spectrum of plane waves is central to this approach. Goodman describes the plane wave spectrum:

> If the complex field distribution of a monochromatic disturbance is Fourier-analyzed across any plane, the various spatial Fourier components can be identified as plane waves traveling in different directions away from that plane. The field amplitude at any other point (or across any other parallel plane) can be calculated by adding the contributions of these plane waves, taking due account of the phase shifts they have undergone during propagation.[52]

Using this approach, wave propagation over a distance z can be seen as a linear filter with a transfer function

$$H_a(f_x, f_y) = \begin{cases} \exp\left[j\frac{2\pi}{\lambda}z\sqrt{1-(\lambda f_x)^2-(\lambda f_y)^2}\right] & \sqrt{f_x^2+f_y^2} < \frac{1}{\lambda}, \\ 0 & \text{otherwise.} \end{cases} \tag{4.18}$$

We are now in a position to analyze the behavior of a Shack-Hartmann wavefront sensor using a wave-optics approach. We start with an aberrated wavefront of unit amplitude at the entrance pupil of the telescope. Let the pupil function of the

telescope be

$$P(x,y) = \begin{cases} 1 & \text{inside the aperture,} \\ 0 & \text{otherwise.} \end{cases} \tag{4.19}$$

The complex field amplitude of the aberrated wavefront at the aperture of the telescope is

$$U_{ab}(x,y) = P(x,y)\ \exp[\,j\,\phi_{ab}(x,y)] \tag{4.20}$$

where $\phi_{ab}(x,y)$ is the wavefront phase. Assume the telescope aperture is perfectly imaged onto the lenslet array. We will find it helpful to define the amplitude transfer function, $t_a(x,y)$, of an aperture or thin optical element as the ratio of the transmitted field amplitude, $U_t(x,y)$, to the incident field amplitude, $U_i(x,y)$,

$$t_a(x,y) = \frac{U_t(x,y)}{U_i(x,y)}. \tag{4.21}$$

The amplitude transfer function in the paraxial region of a lens with focal length f_l, centered at coordinates (x_k, y_k), is

$$t_l(x,y) = \exp\left[-j\frac{\kappa}{2f_l}(x-x_k)^2 + (y-y_k)^2\right] \tag{4.22}$$

where $\kappa = 2\pi/\lambda$.[52] The spatial extent of a rectangular lens can be limited using a rectangular aperture function

$$\text{rect}(x) = \begin{cases} 1 & |x| < \frac{1}{2}, \\ \frac{1}{2} & |x| = \frac{1}{2}, \\ 0 & \text{otherwise.} \end{cases} \tag{4.23}$$

Thus, the amplitude transfer function of the lenslet array in the Shack-Hartmann wavefront sensor is

$$t_{sh}(x,y) = \sum_{k=1}^{P} \exp\left[-j\frac{\kappa}{2f_l}(x-x_k)^2 + (y-y_k)^2\right] \text{rect}\left(\frac{x-x_k}{d}\right) \text{rect}\left(\frac{y-y_k}{d}\right) \tag{4.24}$$

where d is the width of a lenslet.[53] The field amplitude transmitted by the lenslet array is

$$\begin{aligned} U_{la}(x,y) &= U_{ab}(x,y)\, t_{sh}(x,y) \\ &= P(x,y)\, \exp[\, j\, \phi_{ab}(x,y)]\, t_{sh}(x,y). \end{aligned} \tag{4.25}$$

Recall, the detector array lies a distance f_l behind the lenslet array. To find the field amplitude at the detector array, we Fourier transform $U_{la}(x,y)$, given by equation (4.25), multiply by the propagation transfer function $H_a(f_x, f_y)$, then inverse Fourier transform the result. Thus, the field amplitude at the detector array is

$$U_{da}(x,y) = \mathcal{F}^{-1}\left\{\mathcal{F}\{U_{la}(x,y)\}\, H_a(f_x, f_y)\right\} \tag{4.26}$$

where $H_a(f_x, f_y)$ is given in equation (4.18) with $z = f_l$. The amplitude and phase of the field at the detector array coordinates (x,y) are calculated by evaluating the Fourier transform at spatial frequencies $(f_x = x/\lambda f_l, f_y = y/\lambda f_l)$. The intensity distribution in the plane of the detector array is

$$I_{da}(x,y) = |U_{da}(x,y)|^2. \tag{4.27}$$

To accurately model the intensity pattern on the detector array, I gave close attention to sampling of the various functions. In equation (4.25), the sample spacing Δx in the lenslet plane is chosen to satisfy

$$\Delta x \leq \frac{2\lambda f_l}{3d} = \frac{2(0.59\,\mu\text{m})(3400\,\mu\text{m})}{3(144\,\mu\text{m})} = 9.4\,\mu\text{m} \tag{4.28}$$

where f_l is the focal length of the lenslets and d is the pitch of the lenslets.[53] A generous margin was provided by choosing $\Delta x = 2.7\,\mu$m. This yielded more than 50 samples per lenslet. Sampling in the Fourier domain depends on the choice of Δx. The number of samples in the plane wave spectrum propagator of equation (4.26) must satisfy the condition[53]

$$N \geq \frac{3\lambda f_l}{(\Delta x)^2} = \frac{3(0.59\,\mu\text{m})(3400\,\mu\text{m})}{(2.7\,\mu\text{m})^2} = 840. \tag{4.29}$$

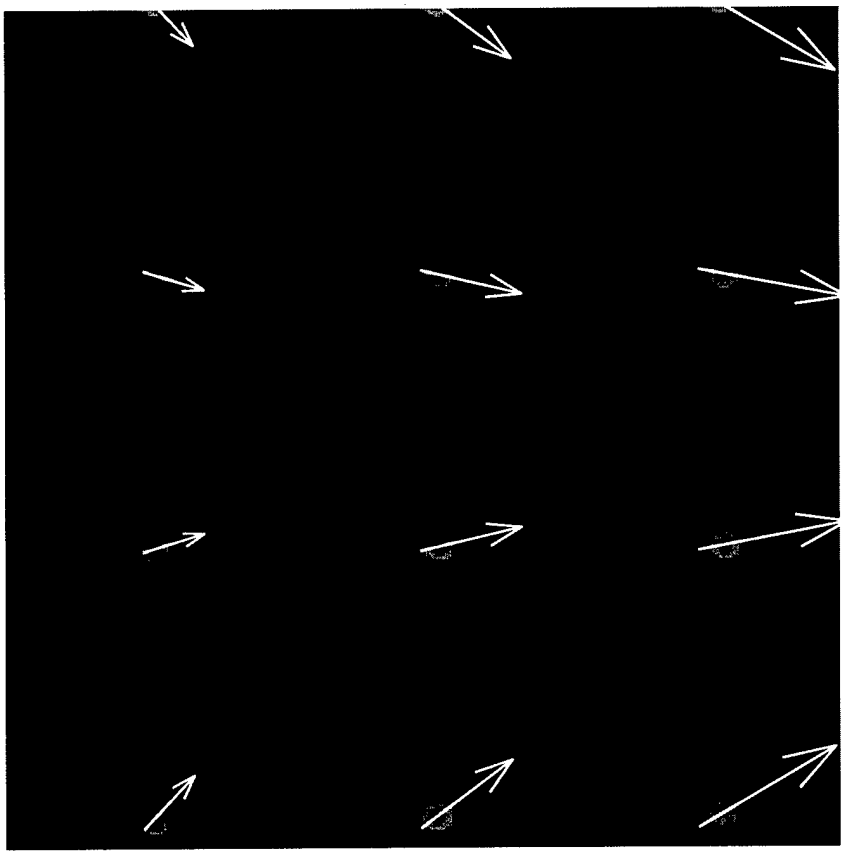

Figure 4.6 Simulated intensity pattern on the wavefront sensor detector array for the Zernike polynomial $Z_{10} = \sqrt{8}\,r^3\cos(3\theta)$. This represents a small section of the detector array about 30 detector pixels wide. The diffraction patterns from the square lenslets are evident. The arrows show the relative spot displacement from the center of each sub-array.

A fast Fourier transform algorithm, requiring $N = 2^n$ where n is an integer, was used in these calculations; thus, the number of samples used was $N = 1024$.

Using the expression for the field amplitude at the detector array in equation (4.26), I developed a model of the wavefront sensor. An image showing a portion of the intensity pattern on the detector array for the Zernike polynomial $Z_{10} = \sqrt{8}\,r^3\cos(3\theta)$ is shown in Figure 4.6. The diffraction patterns from the square lenslets are evident. The arrows show the spot displacement from the center of the sub-array. This theoretical model was the foundation used to build a reconstructor

that estimates wavefronts from centroid measurements.

To review, the algorithm I used to build the reconstructor followed these steps:

1. compute amplitude transfer function of lenslet array, $t_{sh}(x, y)$,
2. compute angular spectrum propagation transfer function, $H_a(f_x, f_y)$,
3. generate phase for each Zernike mode, $\phi_{ab}^m(x, y) = Z_m(x, y)$,
4. calculate intensity pattern at detector array for each Zernike mode, $I_{da}(x, y)$,
5. build matrix $\mathbf{D}$ by computing centroids from $I_{da}(x, y)$,
6. calculate least-squares solution, $(\mathbf{D}^\dagger \mathbf{D})^{-1}\mathbf{D}^\dagger$.

I used this reconstructor to estimate wavefronts from the centroid measurements. I then compared the reconstructed wavefronts with wavefronts measured by a phase-shifting interferometer, as described in the next section.

4.4 Comparison of Wavefront Sensor and Phase-Shifting Interferometer Measurements

After the optical elements of the shimulator were carefully assembled and aligned, the spacings between the elements were measured and adjusted to be within acceptable tolerances. Using phase-shifting interferometer wavefront measurements as a guide, I adjusted the position of the secondary mirror to minimize coma and spherical aberration. The top-box optical components were assembled and precisely attached to the optical bed. The new wavefront sensor optics were installed and the top-box optical components were aligned. In total, over thirty optical elements ranging in size from 5 μm to 65 cm were aligned to tolerances as small as 20 μm. After performing the calibrations to the wavefront sensor measurements outlined above, I sought to compare wavefronts measured by the phase-shifting interferometer. First, measurements were taken with both instruments and no additional

plate	position	d_n
1	89	18
2	122	24

Table 4.5 Turbulence plate positions and beam diameters (d_n). Units are mm.

aberrations added by the turbulence plates. Then, five sets of measurements were taken in the presence of large amounts of simulated turbulence.

Using commercial software, I recorded phase-shifting interferometer fringes and generated wavefronts. I collected several sets of fringes and averaged the wavefronts that were reconstructed from these fringes. This helped to eliminate the effects of non-static turbulence in the optical path and reduce the measurement noise. The main goal was to determine how well the wavefront sensor could measure large amounts of wavefront deformation. To accomplish this, I inserted two near-index-match optical elements to introduce a static wavefront deformation. These turbulence plates, designed and built by T. Rhoadarmer [28], were added and the interferometer and wavefront sensor measurements were recorded. The positions of the plates relative to the fiber source, along with the beam diameters at the plates, are listed in Table 4.5. The turbulence plates were built with a coherence length, r_0, of about 1.2 mm. The ratio of the diameter of the beam, d, to the effective coherence length, r_0^{eff}, is given by

$$\left(\frac{d}{r_0^{eff}}\right)^{5/3} = \left(\frac{d_1}{r_0}\right)^{5/3} + \left(\frac{d_2}{r_0}\right)^{5/3}, \tag{4.30}$$

where d_1 and d_2 are the beam diameters at the two turbulence plates, and r_0 is the coherence length of the phase profiles from each of the turbulence plates. Thus, d/r_0^{eff} was about 27, which yields an r_0^{eff} of about 24 cm on the sky.

I found the best results could be obtained when the milling marks from the

trial	PSI	WFS	PSI − WFS
0	479	515	173
A	706	722	289
B	844	844	323
C	1602	1457	391
D	1196	1053	363
E	583	652	349

Table 4.6 Wavefront statistics for measurements made using the phase-shifting interferometer (PSI) and wavefront sensor (WFS). Listed are the RMS wavefront errors for the PSI, WFS and the difference between the two. Trial 0 is with no turbulence plates, trails A–E are with two turbulence plates. Units are nm; tilt and defocus have been removed.

two turbulence plates were arranged at right angles to each other. Diffraction from the milling marks in the turbulence plates also caused small areas of poor fringe modulation where the phase could not be determined from the phase-shifting interferometer measurements.[28] These small areas were filled in by applying a median window to the reconstructed wavefronts using the interferogram analysis software. The wavefronts measured by the phase-shifting interferometer were then rotated to match the orientation of the wavefront sensor and Zernike polynomials were fitted to the wavefronts.

The following figures show a sample of the reconstructed wavefronts. The wavefronts with no turbulence plates, only the plain shimulator beam, are shown in Figure 4.7. Wavefronts from one of the five trials, trial D, are shown in Figure 4.8. For a clear comparison of the wavefronts, profiles of the wavefronts along two axes are plotted in Figure 4.9. The smoother profiles are reconstructed from wavefront sensor data. Table 4.6 lists wavefront statistics from the five sets of measurements made using the phase-shifting interferometer and wavefront sensor.

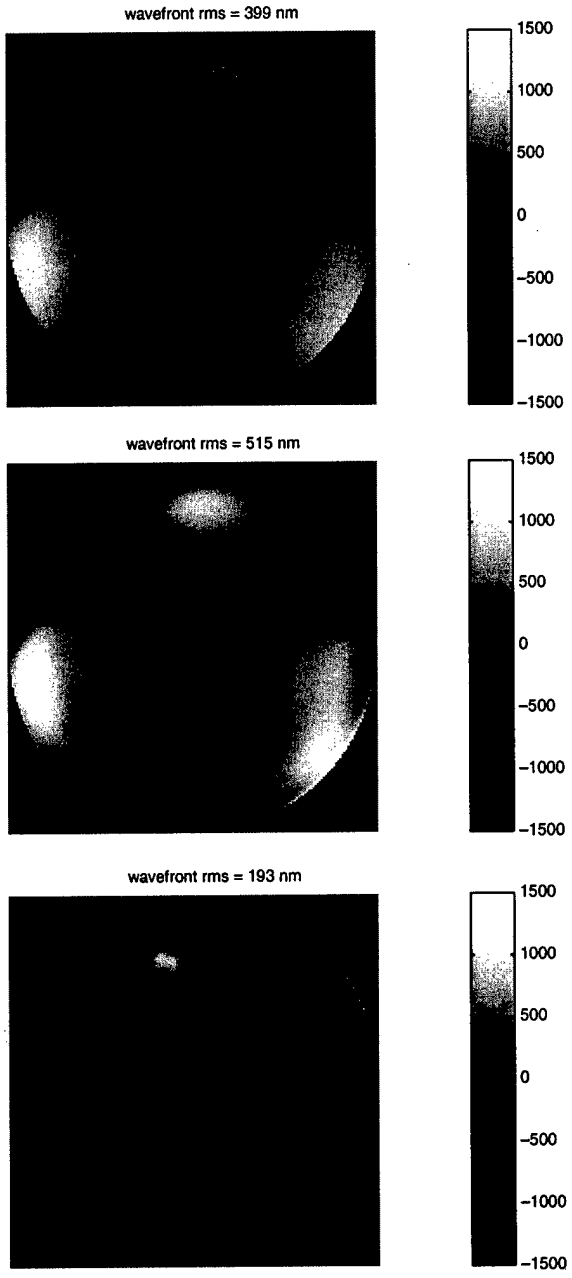

Figure 4.7 Wavefront reconstructions with no turbulence plates using (a) phase-shifting interferometer data, (b) wavefront sensor data, and (c) the difference (a − b). Units are nm; tilt and defocus have been removed.

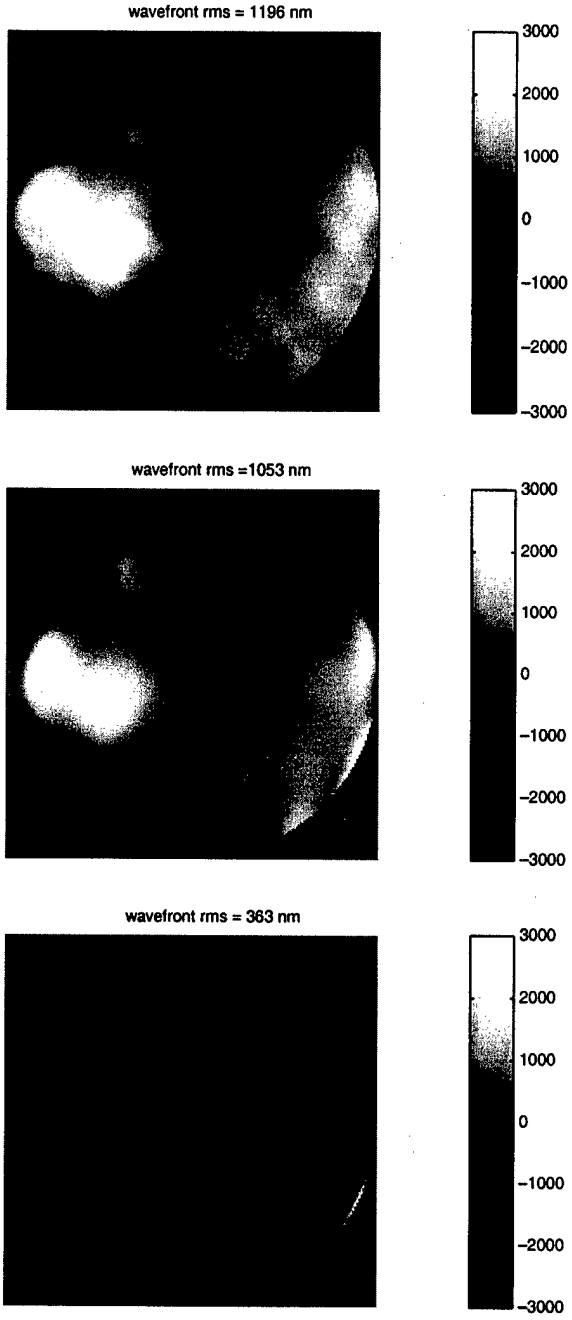

Figure 4.8 One of the five sets (trail D) of wavefront reconstructions with two turbulence plates using (a) phase-shifting interferometer data, (b) wavefront sensor data, and (c) the difference (a − b). Units are nm; tilt and defocus have been removed.

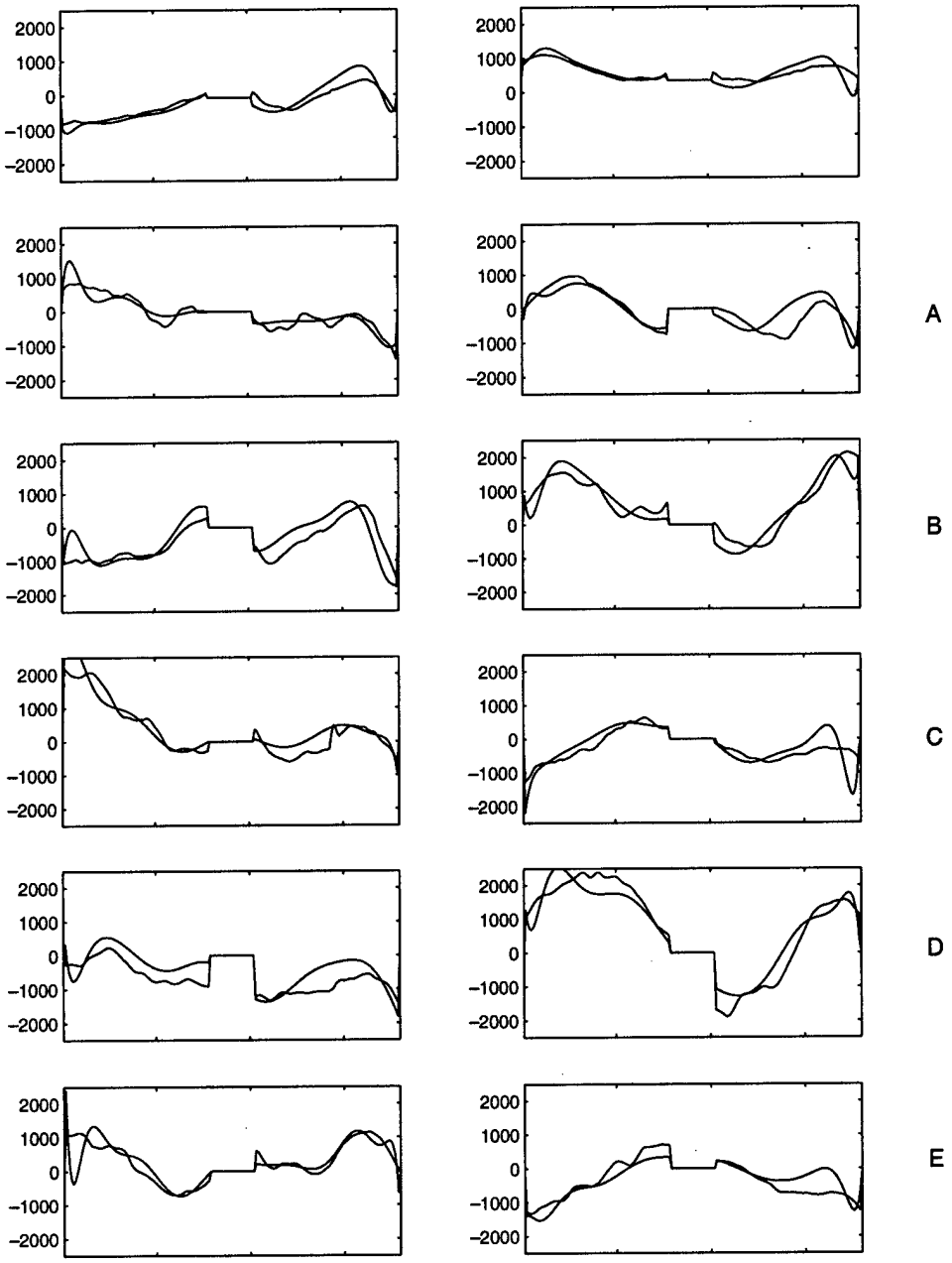

Figure 4.9 Comparison of wavefront profiles for wavefront reconstructions using phase-shifting interferometer and wavefront sensor. The top profiles are with no turbulence plates; the next five sets of profiles are trials with different rotations of two turbulence plates. Units are nm; tilt and defocus have been removed.

As can be seen from Figures 4.7 and 4.8 (c), some of the difference in wavefront measured by the wavefront sensor (WFS) and the phase-shifting interferometer (PSI) is of spatial frequency too high to be detected by the WFS. But this can explain only part of the discrepancy. For example, if we calculate, for the two turbulence plate case, the RMS of the difference between the WFS wavefront and the Zernike polynomial fit of the PSI wavefront, we get about 340 nm RMS, only slightly less than the 360 nm RMS corresponding to the difference between the WFS wavefront and the raw PSI wavefront. Let us take a closer look at the two turbulence plate case.

From the wavefront images, we can see that much of the difference may be due to fitting errors near the edge of the WFS data. This is especially evident in Figure 4.9. In fact, if we calculate the RMS difference over only the central 80 percent of the pupil diameter, we get about 235 nm for the two turbulence plate case.

Note also in Figure 4.9 that the peaks and valleys of the WFS wavefronts often occur at a smaller radial position than those of the PSI wavefronts. This suggests an error in the imaging of the pupil on the WFS lenslet array, that is, the image of the pupil is too small. The observation that the subapertures at the edge of the pupil receive less illumination than those well inside the pupil supports this notion. If we increase the assumed size of the WFS pupil by 6 percent, then calculate the difference between the WFS and PSI wavefronts, we get about 265 nm RMS. This reduces to 210 nm RMS if we consider only the central 80 percent of the pupil diameter. Recall, as described in Section 2.6.2, the pupil size was measured at 1.71 mm, only 1 percent less than the nominal 1.728 mm. An error in imaging the pupil seems an unlikely explanation for the difference in the measured wavefronts. Perhaps inaccuracies in the wavefront sensor measurement of high-order Zernike modes provides a better explanation.

Figure 4.10 Interferogram from the video camera of the phase-shifting interferometer. Note the uniform intensity of the fringes over the outer half of the pupil.

There may be other reasons for the reduced illumination near the edge of the pupil. Obvious reasons include the gaussian intensity profile produced by the fiber source and uneven spray-silver coatings on the large mirrors in the shimulator. If one examines a raw PSI image, as shown in Figure 4.10, we see that although the intensity drops off with radial distance from the center, the decrease is quite gradual. So, unless the top-box optics are to blame for non-uniform illumination of the pupil, further investigation is warranted.

Chapter 5

Gap Sensors: Theory and Design

5.1 Introduction

The 6.5 m MMT adaptive optics system employs a unique adaptive secondary mirror. Using the secondary mirror for wavefront correction eliminates many of the extra mirrors required to implement an adaptive optics system. With fewer mirrors, light throughput is increased and thermal emissivity is reduced. This improves the imaging of faint objects, especially at infrared wavelengths.[16]

The adaptive secondary mirror consists of three layers, as shown in Figure 5.1. The deformable mirror surface is a convex shell made from Schott Zerodur.† The aspheric shell is 1.8 mm thick and 640 mm in diameter.[15] It is supported mechanically by a hub attached to a flexure mounted to the center of a 50 mm thick glass reference surface. This flexure constrains the lateral position of the shell during operation and supports the shell against gravity when the mirror is not operating. The reference surface was carefully fabricated from Corning ultra-low expansion glass. Behind this is a 50 mm thick spherical aluminum cold plate. The 336 electromagnetic force actuators are attached to the cold plate and extend through the reference

†Zerodur is a glass-ceramic material with an extremely low coefficient of thermal expansion.

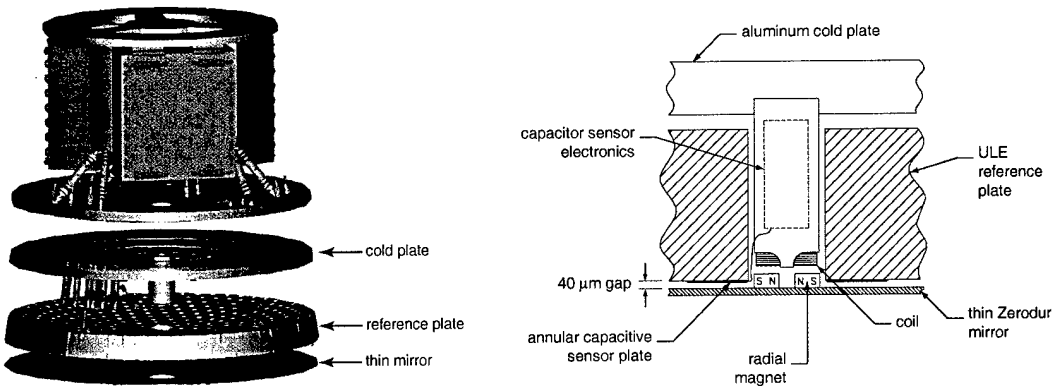

(a) (b)

Figure 5.1 Parts of the adaptive secondary mirror. Figure (a) shows an exploded view of the thin aspheric mirror shell, thick reference plate, and cold plate. Figure (b) is a cross section of a single electromagnetic force actuator and its capacitive position sensor. The actuators consist of an electromagnet that drives a small permanent magnet attached to the back of the deformable mirror shell.

surface. The actuators consist of electromagnets that drive small permanent magnets attached to the back of the deformable mirror surface.

Capacitive position sensors have been placed at each force actuator, to allow local control of the actuator position. The capacitive position sensors share a common plate formed by applying a layer of chromium to the back surface of the deformable mirror. The other capacitor plates are formed by rings of chromium applied to the reference surface around each actuator. Actuator position is referenced to the precisely polished glass surface. The position sensors allow the shape of the mirror to be controlled without measuring the reflected wavefront; thus, the secondary can be used for observations without requiring operation of the entire adaptive optics system. The distance between the deformable mirror and the reference surface is nominally 40 μm. This thin air film provides viscous damping to control resonance in the flexible mirror.[62]

The capacitive sensors will be used to measure and control the deformable mirror at a bandwidth of 1 kHz with an accuracy of a few nanometers.[63] The sensors must be calibrated to provide an accurate measurement. One technique for calibrating these capacitive sensors, uses a phase-shifting interferometer to measure small displacements of the secondary mirror surface. Such an interferometer is not typically available on astronomical telescopes. I have developed a small optical instrument, called a gap sensor, that measures the absolute distance between the thin shell and the thick reference surface. The gap sensors will be installed at 24 locations on the adaptive secondary mirror. They will allow the capacitive position sensors to be quickly and accurately calibrated without installing and aligning an interferometer on the telescope. The gap sensor is a unique tool for precisely measuring the thickness of any transparent film and thus has many applications beyond the one described here.

5.2 Optics of Thin Films

5.2.1 Reflected Intensity for a Film Between Glass Surfaces

Under certain conditions, when two waves reflect from the surfaces of a thin film, the waves interfere constructively if the optical thickness of the film is an integral number of half-wavelengths. By observing the pattern of interference between the two waves as their wavelength is varied, the thickness of the film can be determined. Before attacking the problem of multiple beam interference in multiple layers of thin films, we first consider a simple thin film between two thick surfaces. A film is thin when interference occurs in either the reflected or transmitted light. Interference effects will be observed when the optical path length through the film is less than the coherence length of the light; accordingly, when the optical path length is greater than the coherence length, the film is thick. The approach here will be brief and

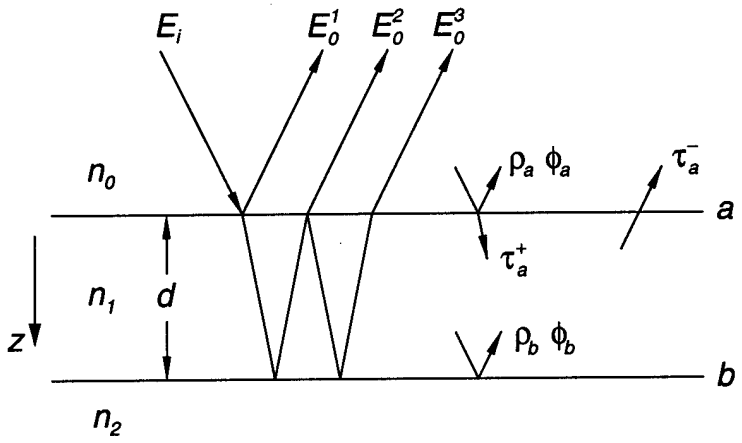

Figure 5.2 Notation for a single thin film between two thick surfaces. The derivation in the text is for normal incidence; the rays are shown separated for clarity.

incomplete; please consult Born and Wolf for a more rigorous analysis.[24]

Consider a thin transparent film of refractive index n_1 and thickness d surrounded by two glass plates of index n_0 and n_2 as shown in Figure 5.2. The interface between the upper glass plate and the film is labeled boundary a; the interface between the film and the lower glass plate is labeled boundary b. Let this film be illuminated by a normally incident monochromatic plane wave of complex amplitude E_i and wavelength λ. This results in a series of reflected plane waves of complex amplitude E_0^1, E_0^2, E_0^3, ... Let ρ_a and ρ_b be the reflection amplitude coefficients for boundary a and boundary b, respectively, and let ϕ_a and ϕ_b be the phase changes associated with the reflections at these boundaries. Also let τ_a^+ and τ_a^- be the transmission amplitude coefficients at boundary a for the positive and negative going waves, respectively.

For the case where $n_0 = n_2$, the complex amplitudes of the reflected plane waves are

$$\begin{aligned} E_0^1 &= E_i \rho_a e^{i\phi_a}, \\ E_0^2 &= E_i \tau_a^+ \tau_a^- \rho_b e^{i(2\delta+\phi_b)}, \\ E_0^3 &= E_i \tau_a^+ \tau_a^- \rho_b^3 e^{i(4\delta+3\phi_b)}, \\ &\vdots \end{aligned} \tag{5.1}$$

where the phase change due to the film thickness is

$$\delta = 2\pi n_1 d/\lambda. \tag{5.2}$$

The amplitude reflection and transmission coefficients for normal incidence are given by the Fresnel formulae

$$\begin{aligned} \rho_a &= \frac{n_0 - n_1}{n_0 + n_1}, \\ \rho_b &= \frac{n_1 - n_2}{n_2 + n_1}, \\ \tau_a^+ &= \frac{2n_0}{n_0 + n_1}, \\ \tau_a^- &= \frac{2n_1}{n_0 + n_1}. \end{aligned} \tag{5.3}$$

Neglecting terms in ρ_b of higher order than two, we get for the reflected amplitude

$$\begin{aligned} E_r &= E_0^1 + E_0^2 \\ &= E_i[\rho_a e^{i\phi_a} + \tau_a^+ \tau_a^- \rho_b e^{i(2\delta+\phi_b)}]. \end{aligned} \tag{5.4}$$

For a thin film of air, $n_1 = 1$, surrounded by two glass plates of the same index, $n_2 = n_0 = 1.5$, the quantity ρ_b^3 in equation (5.1) is -0.008. This implies $E_0^2 \gg E_0^3$; the approximation made in equation (5.4) gives a good estimate of the reflected amplitude. Since ρ_a is positive, $\phi_a = 0$, so long as $n_0 > n_1$; conversely, since ρ_b is negative, $\phi_b = \pi$, so long as $n_1 < n_2$.[24] Furthermore, $\rho_b = -\rho_a$ since $n_2 = n_0$. The expression for the reflected amplitude can be simplified

$$\begin{aligned} E_r &= E_i[\rho_a - \tau_a^+ \tau_a^- \rho_a e^{i2\delta} e^{i\pi}] \\ &= E_i[\rho_a + \tau_a^+ \tau_a^- \rho_a e^{i2\delta}]. \end{aligned} \tag{5.5}$$

If E_r^* is the complex conjugate of E_r, the reflected intensity is

$$\begin{aligned} I_r &= E_r E_r^* \\ &= E_i E_i^* \rho_a^2 [1 + (\tau_a^+)^2 (\tau_a^-)^2 + \tau_a^+ \tau_a^- (e^{i2\delta} + e^{-i2\delta})]. \end{aligned} \tag{5.6}$$

Applying Euler's formula, $(e^{i2\delta} + e^{-i2\delta}) = 2\cos(2\delta)$, equation (5.6) simplifies to

$$I_r = I_i \rho_a^2 [1 + (\tau_a^+)^2 (\tau_a^-)^2 + 2\tau_a^+ \tau_a^- \cos(2\delta)]. \tag{5.7}$$

We define reflectance as the ratio of the reflected and incident intensities, $R \equiv I_r / I_i$. Substituting for δ and inserting the refractive indexes in equation (5.3) yields

$$R \approx (0.077) \left[1 + \cos\left(\frac{4\pi d}{\lambda} \right) \right]. \tag{5.8}$$

Thus, if we measure the reflected intensity as the wavelength of the incident light is increased, we get interference fringes whose spacing increases with wavelength, as shown in Figure 5.3. As film thickness d increases, fringe spacing decreases. These fringes can be recorded, then analyzed to determine the thickness of the film.

5.2.2 Reflected Intensity for a Film Between Metal Layers

The analysis in the previous section ignores the effect of multiple reflections within the thin film. In that simple analysis, the reflected amplitudes E_0^1 and E_0^2 have about the same magnitude; the fringe visibility is nearly unity as shown in Figure 5.3. Fringe visibility $\mathcal{V}$ is defined as

$$\mathcal{V} = \frac{I_{max} - I_{min}}{I_{max} + I_{min}} \tag{5.9}$$

where I_{max} and I_{min} are the maximum and minimum intensities in the immediate neighborhood of some point in the interferogram. Although high fringe visibility is clearly desirable, the average reflected intensity is a small fraction of the incident

(a)

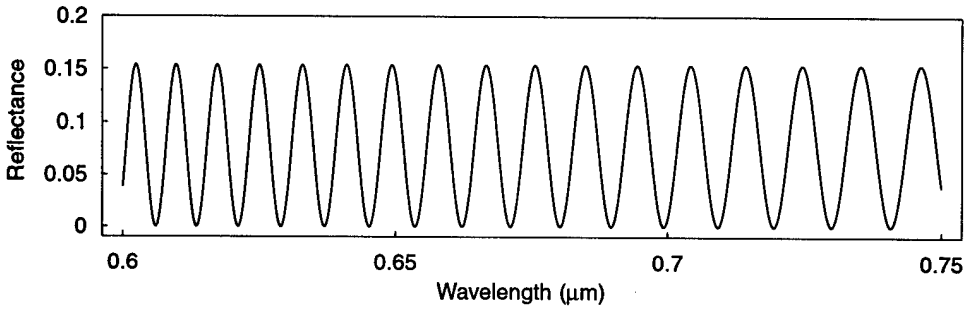

(b)

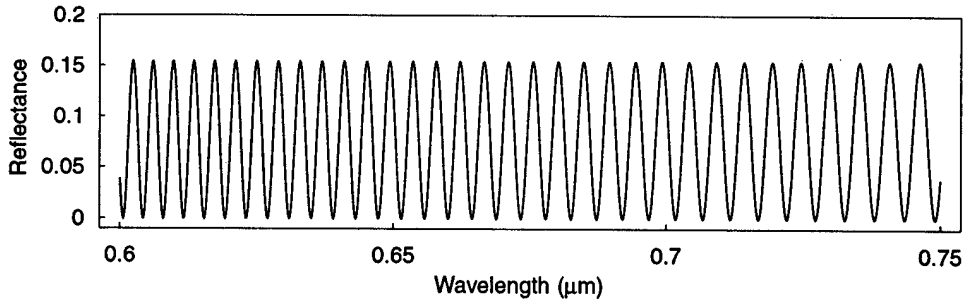

Figure 5.3 Reflected intensity modeled using equation (5.8) for thin air films between two glass surfaces. Only the first two reflected rays are considered in this model. The fringe spacing increases with wavelength. As film thickness increases, fringe spacing decreases. Figure (a) shows fringes for a 25 μm film; Figure (b) shows fringes for a 50 μm film.

intensity. If a semi-transparent film of metal is applied to the first interface, boundary a, and a thick layer of metal is applied to boundary b, the reflected intensity is increased while maintaining good fringe visibility. This complicates matters as the multiple reflections in the film of air can not be ignored. An accurate analysis must account for the effect of these extra reflections. Applying the approach taken in the previous section would quickly lead to extremely complex expressions. Fortunately, Macleod presents an elegant approach to solving Maxwell's equations for a series of thin films.[24,55] Rather than tracing each ray as it reflects at each boundary then summing the result, this approach sets boundary conditions then solves Maxwell's equations for the reflected and transmitted waves. The solution is general and compact with each layer represented by a 2×2 matrix; a series of films is represented by a product of these matrices. The solution is simply presented here after a brief description of its derivation.

Before presenting the solution, we must select a convention for the vector directions used to calculate phase differences. The conventions we use here are illustrated in Figure 5.4. As usual, the plane of incidence is defined by the incident ray and the surface normal. The field vectors are divided into two orthogonal components. A wave with the electric field vector in the plane of incidence is called p-polarized; a wave with the electric field vector perpendicular to the plane of incidence is called s-polarized. A p-polarized wave is also called TM for transverse-magnetic; an s-polarized wave is called TE for transverse-electric.

The p- and s-polarized field vector components are first examined for non-absorbing media. The solution for a single interface is then obtained by carefully applying boundary conditions, equating components of the electric and magnetic fields parallel to the boundary. The reflectance and transmittance are calculated in terms of energy flows traveling perpendicular to the boundary. The solution for

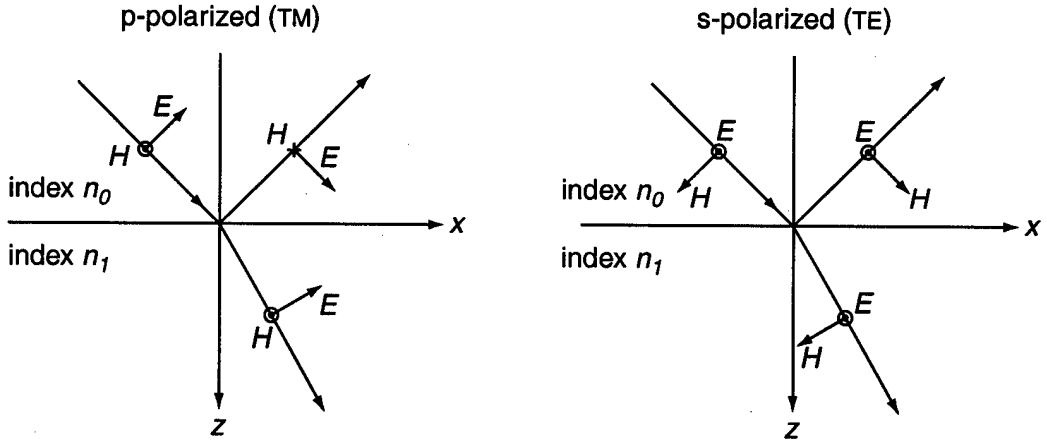

Figure 5.4 Sign conventions for electric and magnetic field vectors. Positive directions are shown for (a) p-polarized or TM waves and (b) s-polarized or TE waves.

absorbing media can be obtained by restricting calculations of reflectance to transparent incident media. The solution for a single interface is extended first to a single thin film, then to an assembly of thin films.

The notation for two thin films on a thick surface is illustrated in Figure 5.5. The complex index of refraction is $N = n - ik$, where n is the real refractive index and k is the extinction coefficient. Angles of refraction within the media are calculated from Snell's law, $N_0 \sin\theta_0 = N_1 \sin\theta_1$, which may include complex angles. For oblique angles of incidence, the tilted optical admittance is defined as

$$\eta_s = N\mathcal{Y}\cos\theta \qquad \text{s-polarization} \qquad (5.10)$$

$$\eta_p = N\mathcal{Y}/\cos\theta \qquad \text{p-polarization} \qquad (5.11)$$

where $\mathcal{Y}$ is the admittance of free space; $\mathcal{Y} = 2.654 \times 10^{-3}$ S. The fields at opposing boundaries can be calculated by shifting the z coordinate by the film thickness d and altering the phase factor. For a positive-going wave we multiply by $\exp(i\delta)$;

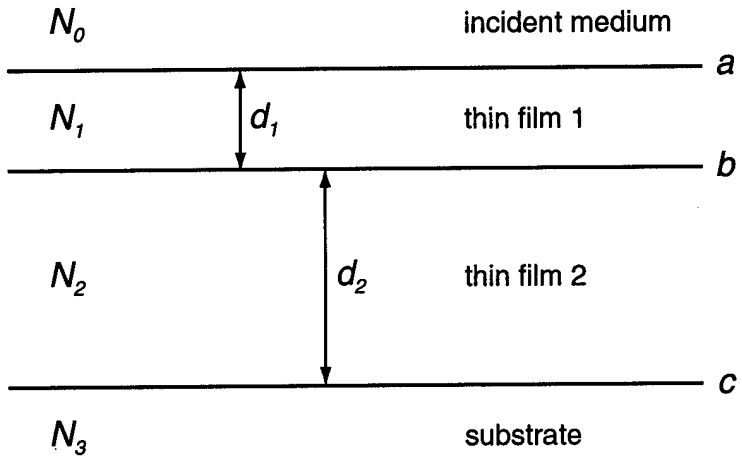

Figure 5.5 Notation for two thin films on a thick substrate. The incident medium is non-absorbing.

for a negative-going wave we multiply by $\exp(-i\delta)$ where $\delta = 2\pi N d \cos\theta/\lambda$. For absorbing media, the phase thickness is computed using

$$\delta_r = (2\pi/\lambda)\, d_r (n_r^2 - k_r^2 - n_0^2 \sin^2\theta_0 - 2\, i\, n_r k_r)^{1/2} \tag{5.12}$$

where the subscript r denotes the absorbing medium, the subscript 0 denotes the incident medium, and the correct solution is in the fourth quadrant. The admittances for absorbing media are

$$\eta_{rs} = \mathcal{Y}\,(n_r^2 - k_r^2 - n_0^2 \sin^2\theta_0 - 2\, i\, n_r k_r)^{1/2}, \tag{5.13}$$

and

$$\eta_{rp} = \left[\mathcal{Y}^2\,(n_r - i\, k_r)^2\right]/\eta_{rs}, \tag{5.14}$$

for s- and p-polarization, respectively.

The behavior of a stack of thin films with q layers can be calculated by using the product of the characteristic matrices of the individual layers

$$\begin{bmatrix} B \\ C \end{bmatrix} = \left(\prod_{r=1}^{q} \begin{bmatrix} \cos\delta_r & (i\sin\delta_r)/\eta_r \\ i\eta_r \sin\delta_r & \cos\delta_r \end{bmatrix} \right) \begin{bmatrix} 1 \\ \eta_m \end{bmatrix} \tag{5.15}$$

where the subscript r denotes each layer and η_m is the substrate admittance. The qth layer is the layer closest to the substrate. In equation (5.15), the symbols B and C represent the two elements of the matrix formed by the product on the right-hand side of the equation. The multilayered stack can be treated as a single surface with optical admittance $Y = C/B$. The reflectance, transmittance, and absorptance are

$$R = \left(\frac{\eta_0 B - C}{\eta_0 B + C}\right)\left(\frac{\eta_0 B - C}{\eta_0 B + C}\right)^*, \tag{5.16}$$

$$T = \frac{4\eta_0 \,\Re(\eta_m)}{(\eta_0 B + C)(\eta_0 B + C)^*}, \tag{5.17}$$

and

$$A = \frac{4\eta_0 \,\Re(BC^* - \eta_m)}{(\eta_0 B + C)(\eta_0 B + C)^*}. \tag{5.18}$$

Since the distinction between s- and p-polarization disappears for normal incidence, these expressions can be greatly simplified. Even so, the dependence of reflectance on wavelength can not as easily be discerned from equation (5.16) as with equation (5.8).

Using a computer with mathematical analysis software, I developed an algorithm to implement the expression for reflectance given in equation (5.16). The reflectance was then calculated using this algorithm. The results are graphed in Figure 5.6. The reflectance for two structures are shown: a 25 μm air film between thick glass surfaces; and a 25 μm air film between a 7 nm chromium film on glass and a thick layer of chromium. The arrangement of the layers is listed in Table 5.1 along with the refractive indexes. Note the fringes produced by the multiple reflection model of structure (a) are nearly identical to those in Figure 5.3 (a), which used a single reflection model. The fringes produced by structure (b) display a different form;

(a)

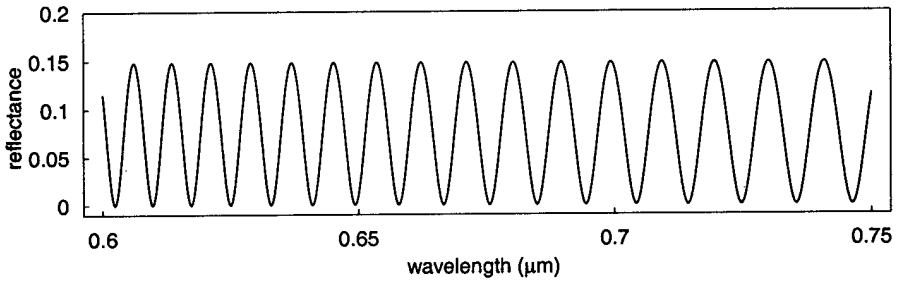

(b)

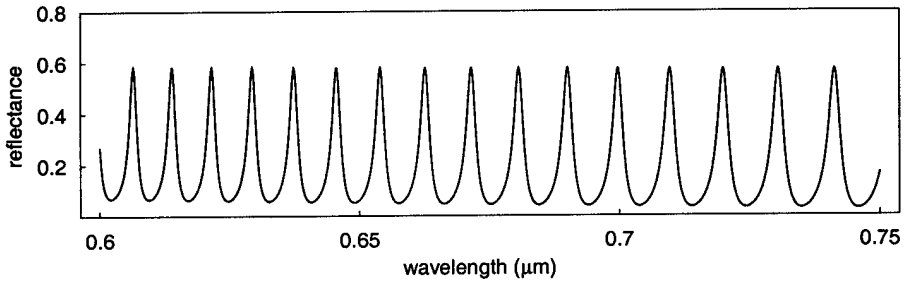

Figure 5.6 Reflected intensity modeled for multiple reflections using equation (5.16) for 25 μm air films. Spectral dispersion in the media is not modeled. Figure (a) shows fringes for an air film between glass surfaces; Figure (b) shows fringes for an air film between chromium layers. See Table 5.1 for the structure of the layers modeled here.

(a)	material	$\longrightarrow$	glass	air	glass
	thickness	$\longrightarrow$	thick	25 μm	thick
	index	$\longrightarrow$	1.52	1.00	1.52
(b)	material	glass	chromium	air	chromium
	thickness	thick	7 nm	25 μm	thick
	index	1.52	$3.8 - i4.4$	1.00	$3.8 - i4.4$

Table 5.1 Structure of layers modeled using multiple reflection algorithm. The indexes listed are for 700 nm wavelength. Reflectance is shown in Figure 5.6.

they are much narrower than the fringes of structure (a). Structure (b) produces multiple reflections similar to those produced by a Fabry-Perot interferometer[64], albeit with low finesse; hence, the fringes become narrow.

The thickness of the chromium film in structure (b) was chosen to maximize the visibility of the interference fringes. Clearly visibility is maximized when I_{min} is zero. Fringe visibility was calculated using equation (5.9) at three different wavelengths as the thickness of the chromium film was varied. Calculating visibility at different wavelengths is necessary since the complex index of the chromium varies with wavelength: from 3.1 at 0.55 μm to 4.5 at 1.05 μm. The refractive index and absorption coefficient of chromium are illustrated in Figure 5.7. As shown in Figure 5.8, the model indicated visibility was greater than 0.8 for a chromium film thickness of about 4–9 nm; errors towards thicker chromium films would yield better fringe visibility.

5.3 Algorithm to Calculate Film Thickness

The thickness of the transparent film or air gap can be calculated from the interference fringes if the refractive index and spectral dispersion of the film are known. In this section, I describe two methods that can be used to find gap thickness:

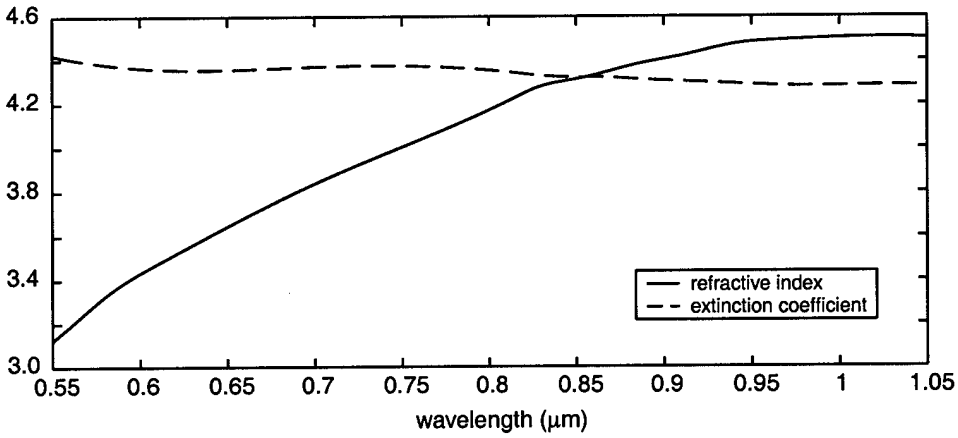

Figure 5.7 Refractive index and extinction coefficient for chromium as a function of wavelength.

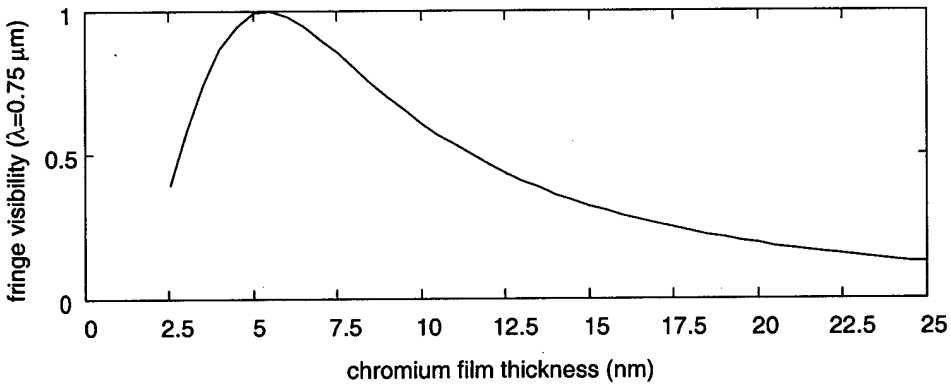

Figure 5.8 Fringe visibility modeled as a function of chromium film thickness. The structure modeled was a 50 μm air film between a thin chromium film on glass and a thick layer of chromium. The wavelength used was 0.75 μm. Visibility is greater than 0.8 for a chromium film thickness of about 4–9 nm.

one method finds the correlation between modeled and measured fringes, the other method uses a Fourier transform. Then, I discuss refinements to the algorithm to increase the precision of measurements of gap thickness. For this work, it is assumed the transparent film, whose thickness is to be measured, is air with refractive index 1.0 and no spectral dispersion.[‡] The structure discussed is a nominally 50 μm air gap sandwiched between a thin chromium film on glass and a thick layer of chromium.

5.3.1 Developing an Algorithm

A straightforward method to calculate gap thickness from measured fringes is to model the fringes produced for a particular gap, then calculate the correlation of the modeled fringes with the measured fringes. This process is repeated for a range of gap thicknesses, yielding a result similar to that plotted in Figure 5.9. The modeled gap with the highest correlation gives the measured gap thickness. The correlation coefficient is calculated from M reflectivity measurements R_{meas} made at wavelengths λ_j

$$cc = \frac{\sum_{j=1}^{M} R_{meas}(\lambda_j) R_{model}(\lambda_j)}{\sum_{j=1}^{M} R_{meas}^2(\lambda_j)} \tag{5.19}$$

where the modeled reflectivity is denoted by R_{model}. A comparison between modeled and measured fringes is shown in Figure 5.10. Modeled fringes for three gap thickness are illustrated, each representing three points on the correlation curve of Figure 5.9, the peak and the two minima.

The correlation method is not the most efficient; fringes for many gap thicknesses must be modeled and compared with the measured fringes. The range of gap thicknesses that must be modeled can be greatly reduced if an estimate of the gap

[‡]The refractive index of dry air at standard temperature and pressure is

$$n = 1 + 10^{-6} \times \left(287.6 + 1.629\lambda^{-2} + 0.0136\lambda^{-4}\right)$$

where λ is the vacuum wavelength in microns. The index of air at 0.7 μm is about 1.00029 and the dispersion is about 0.009; the approximation is valid.

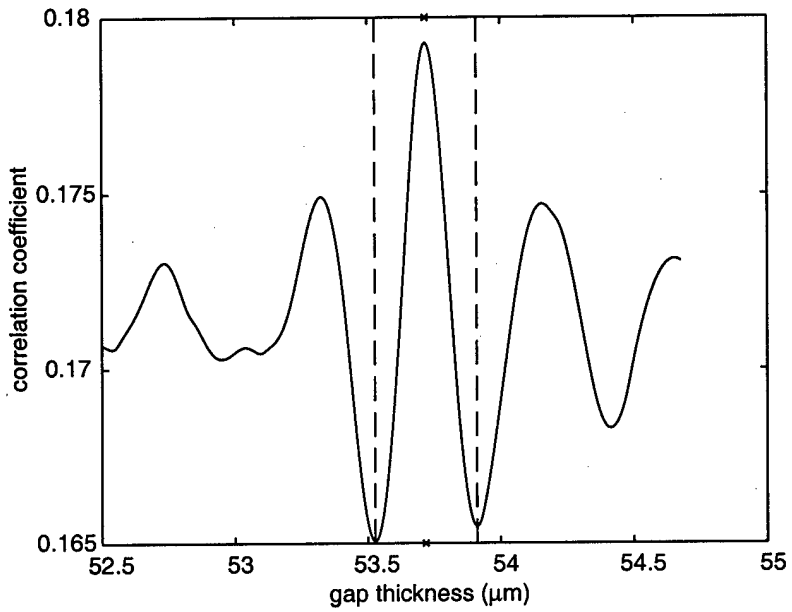

Figure 5.9 Correlation for modeled fringes and measured fringes for an approximately 54 μm air gap. The dashed lines mark the first minima in the correlation curve; they represent the resolution of the correlation method in determining gap thickness. The minima occur at $\pm\lambda/4$ from the peak of the correlation, where the wavelength λ is at the center of the wavelength band.

(a)

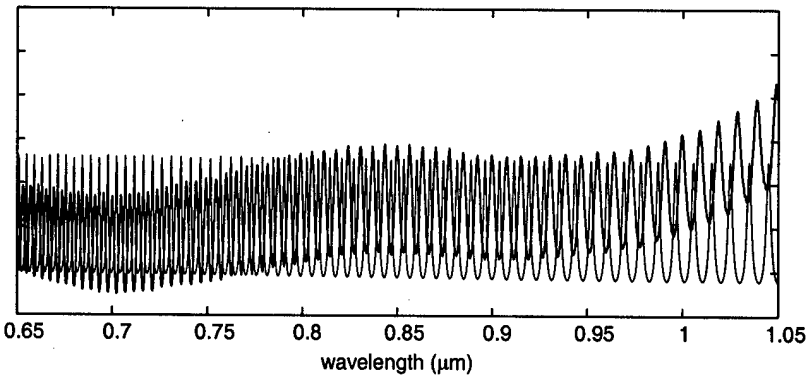

(b)

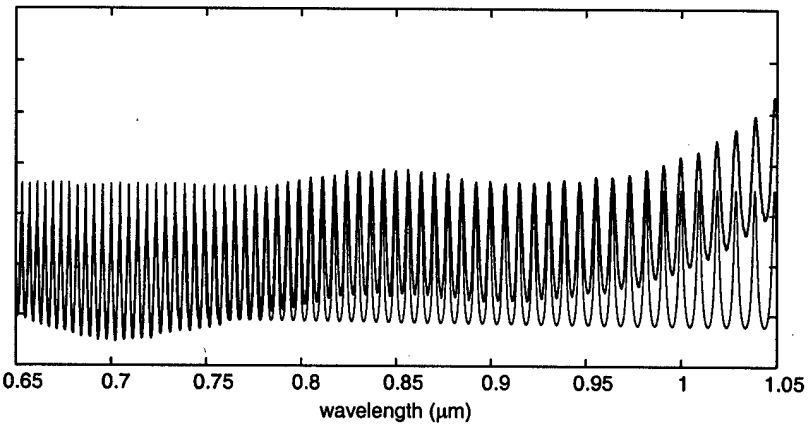

(c)

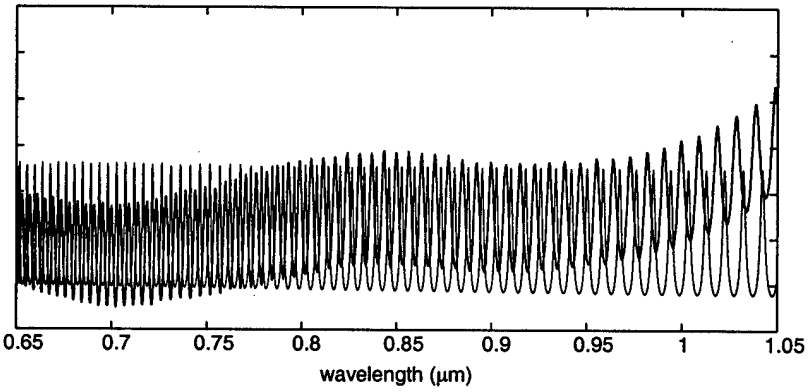

Figure 5.10 Comparison between modeled fringes and measured fringes. Three gap thicknesses are modeled: (a) 53.53 μm, (b) 53.72 μm, and (a) 53.91 μm. These gaps correspond to three points on the correlation curve of Figure 5.9: the first minimum, the peak, and the second minimum, respectively. The thin lines represent the modeled fringes, the thick lines represent the measured fringes.

thickness is known. If the reflectance, as given in equation (5.8), is expressed in terms of wavenumber[§] κ,

$$R \sim 1 + \cos(4\pi\kappa d) \tag{5.20}$$

the result is cosine fringes. The fundamental frequency of the cosine fringes is related to the phase difference between the waves reflected from the two surfaces surrounding the air film. This fundamental frequency is found by uniformly sampling an interpolation of the measured fringes in wavenumber, then applying a Fourier transform. The Fourier transform of a cosine function is a Dirac delta function, whose argument is related to the fundamental frequency. The result of this process is shown in Figure 5.11 where the modulus of the Fourier transform is plotted; the frequency axis has been changed to show the gap thickness. The resolution Δd in the frequency domain depends solely on the wavelength range used to measure the fringes

$$\Delta d = \frac{1}{2} \frac{\lambda_1 \lambda_2}{|\lambda_1 - \lambda_2|} \tag{5.21}$$

where λ_1 and λ_2 are the start and end wavelengths, respectively, for the scan. For the 0.55–1.05 μm range, the resolution is 0.58 μm. Although this resolution is unacceptably large for calibrating the capacitive sensors, the Fourier transform method gives a good estimate of the gap size. This estimate is used to narrow the range of gap sizes to model, so only the immediate neighborhood of the estimate must be searched for the correct gap thickness. The neighborhood is $\pm\Delta d$ around the Fourier transform estimate. This significantly reduces the time required for computation.

The time required for finding the maximum of the correlation curve is further reduced through the use of a maximization algorithm.[65] The maximum is initially

[§]Wavenumber is actually the reciprocal of the vacuum wavelength λ_0, that is, $\kappa = 1/\lambda_0$. Since we are measuring thin films of air, $\lambda_0 = n\lambda \approx \lambda$ and $\kappa \approx 1/\lambda$.

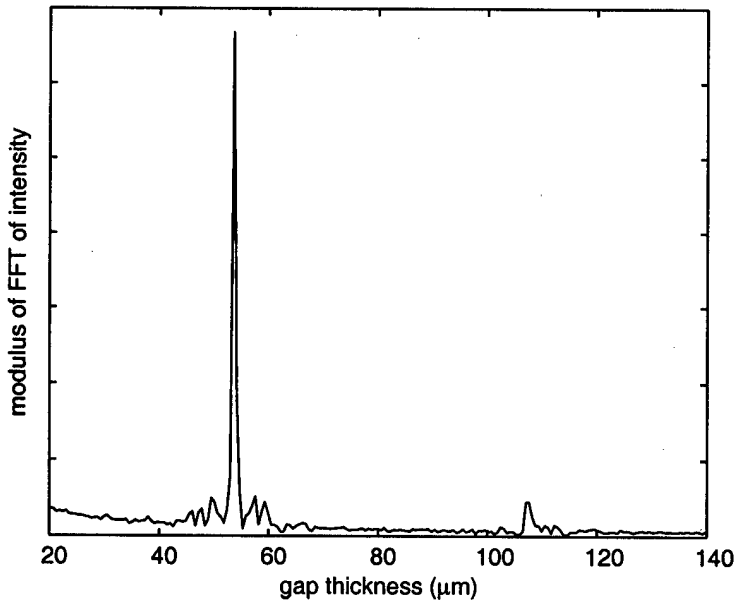

Figure 5.11 Modulus of the Fourier transform of interference fringes in wave-number space for an approximately 54 μm gap. The second harmonic at 108 μm represents the sharpening of the fringes due to multiple reflections between the chromium layers.

bracketed using standard bisection techniques. This is an important step since there are a few local maxima within $\pm\Delta d$ of the Fourier transform estimate. After the maximum is bracketed, parabolic interpolation is used to quickly find the maximum.

5.3.2 Refining the Algorithm

The precision of gap thickness measurements depends upon several factors. The accuracy of the algorithm used to model the fringes is especially important. Some of the uncertainties in the model are related to the optical properties of the chromium film; that is, the phase change associated with reflection from, and transmission through, the film. The optical properties of a semi-transparent metal film depend somewhat on how it is deposited, especially for films less than 20 nm thick.[66] For instance, the reflectance of thin silver films increases substantially with deposition rate.[67] Slowly deposited films have a more granular crystal structure which can affect the absorptance of the film. Heavens points out the pitfalls in calculating the

optical properties of semi-transparent metal films from the measured characteristics of the bulk metal. Phase errors of $\lambda/10$ have been observed between measured phase changes and calculated phase changes associated with reflection and transmission in 10 nm thick platinum films.[68] Discrepancies between measured and calculated phase changes could lead to significant errors in calculating gap thickness if similar behavior exists with chromium films. From equation (5.12) and the data given in Figure 5.7, a 7 nm thick chromium film introduces a phase thickness of $\lambda/12$ when twice traversed. Please note, the uncertainty in phase thickness is likely less than $\lambda/12$ as the uncertainty in phase thickness must be less than the uncertainty in the gap measurement.

The relative phase change upon traversing a metal film can be determined experimentally and used to improve the accuracy of the model. This can be done using polarimetry.[69] Monochromatic light is used to produce interference fringes by illuminating a system of known geometry—a highly-polished metal ball in contact with the metal film. The relative phase change can then be discerned by examining the geometry of the interference fringes. Since the effects of the film can vary with wavelength, this measurement should be repeated for different wavelengths. Phase change at intermediate wavelengths can be found through interpolation. These measurements could be made using the witness samples of the chromium film that was applied to the reference surface.

The complexity of measuring the wavelength dependent phase difference associated with the thin chromium film could be avoided by implementing a two-variable correlation. In finding the fringes with the best correlation, both the gap thickness, and the relative phase between the two reflected beams, could be varied. Several two-variable correlations could be performed using different fringe measurements and the resulting relative phases could be averaged. This should yield a measure of

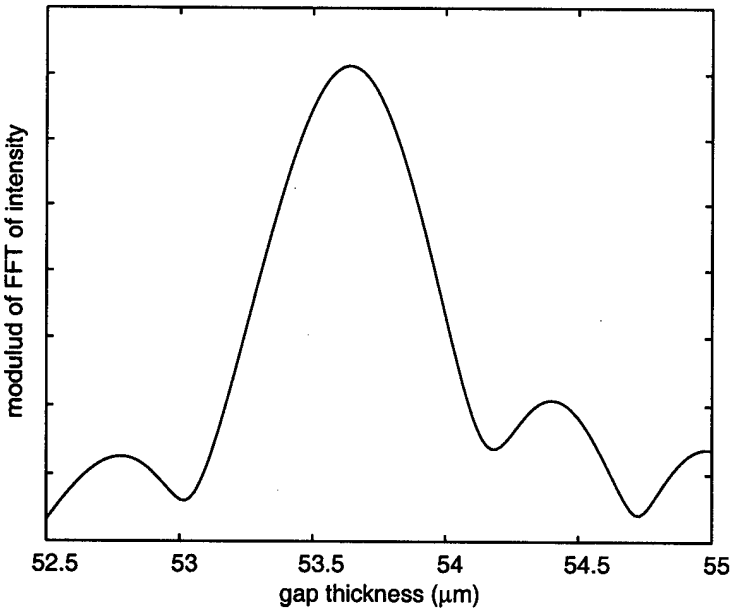

Figure 5.12 Modulus of the Fourier transform of interference fringes padded with zeros. The measured fringes were padded with zeros to increase the precision in locating the peak of the curve. The peak was estimated to lie at 53.64 μm.

the relative phase which could be used for subsequent measurements at a particular location on the secondary mirror. The accuracy of this estimate of the relative phase is limited in part by its dependence on wavelength. Again, using the data given in Figure 5.7 in equation (5.12), the phase thickness of a 7 nm chromium film varies about 0.065 radians from 0.55–1.05 μm.

If the speed and simplicity of computation is the primary concern, the best algorithm for determining gap thickness from fringe measurements uses the Fourier transform method. The location of the peak of the Fourier transform depends only on the period of the interference fringes, which corresponds to the gap thickness. The peak does not depend on the phase of the interference fringes; thus, the Fourier transform method is insensitive to a fixed relative phase between the two interfering waves. The peak of the modulus of the Fourier transform can be located with greater precision by padding the measured fringes with zeros, as illustrated in Figure 5.12.

5.4 Gap Sensor System Design

5.4.1 Gap Sensor Design Concept

There were only a few requirements or constraints that governed the design of the gap sensor system.

1. The gap sensor should measure the nominally 40 μm gap between the back of the mirror shell and the thick reference surface with an accuracy of 5 nm.
2. The measurements should be made at enough places on the mirror to allow calibration of the 336 capacitive position sensors.
3. The gap sensors should occupy a small volume on the back of the cold plate; they must fit in the 25 mm space between the actuators.

Professor Roger Angel conceived the idea to use polychromatic interference to measure the gap thickness.[50] It was decided gap measurements at 24 places on the mirror would be sufficient. Because of space limitations, light would be supplied to the gap sensors via optical fiber. The initial concept was to use a spectrometer to capture the interference fringes over a wide spectral band. The gap could be illuminated with white light and the reflected spectrum could be carried to a spectrometer over optical fiber. I soon discovered it was inefficient to couple white light into a fiber that would carry it to the gap sensor, then couple the reflected light back into the fiber. The concept was changed: illuminate the gap with light from a monochromator, then measure the reflected intensity at the gap sensor as the wavelength is varied. This concept is illustrated in Figure 5.13. I verified this concept in the laboratory by building a prototype system; then used the prototype to design and build the actual components. I designed the gap sensor optical components and wrote the data collection software and processing algorithms; G. Angeli expertly designed the detector electronics. A description of the gap sensor components is presented in the sections that follow.

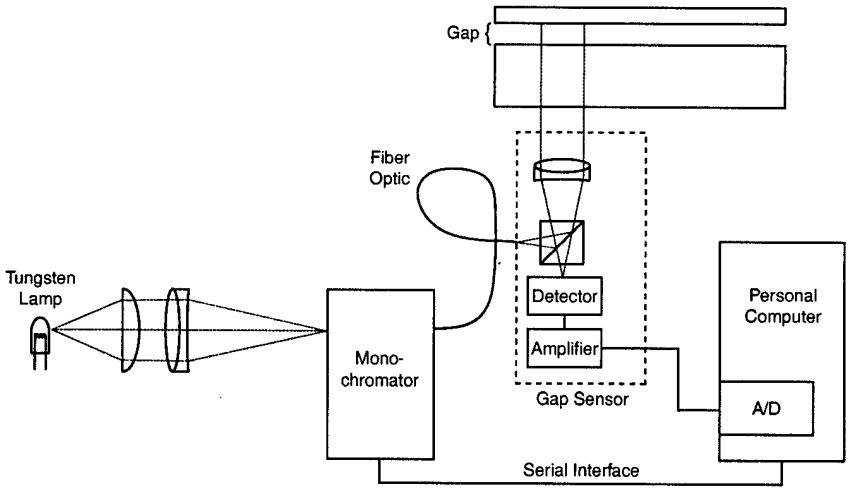

Figure 5.13 Schematic diagram of the gap sensor system. White light from an incandescent lamp is imaged onto the entrance slit of a monochromator. Monochromatic light is coupled into a multi-mode optical fiber which brings light to the gap sensor module at the back of the adaptive secondary mirror. The gap sensor module directs the light towards the gap and measures the reflected intensity with a photodiode. The photodiode output is amplified and digitized. The monochromator wavelength is changed and an entire spectrum is recorded.

White light from an incandescent lamp is imaged onto the entrance slit of a microprocessor-controlled monochromator. Quasi-monochromatic light from the monochromator is sent to 24 instruments, called gap sensor modules, via a multi-mode optical fiber bundle. Each gap sensor module consists of a cube beamsplitter, achromatic lens, silicon photodiode detector, and signal amplifier. The beamsplitter directs light from the optical fiber towards the lens. The lens collimates the light and sends it towards the gap. Light reflected from the gap is collected by the lens and is focused onto the detector. The electrical signal from the detector is amplified locally and digitized by a remote personal computer. Software in the computer commands the monochromator to change the wavelength of the light as the software reads and stores digitized intensity values. After the interference fringes are collected, the software calculates the gap thickness using the methods described in

Section 5.3. When the final system is implemented at the 6.5 m MMT, the personal computer will be replaced by a dedicated microprocessor that is a component of the adaptive mirror control system.[20]

5.4.2 Quasi-monochromatic Light Source

Quasi-monochromatic light for the gap sensors is provided by a system consisting of a white light source, condensing optics, a monochromator, and an optical fiber bundle. The layout of the components is shown in Figure 5.14. The components are mounted on a vibration-damping optical breadboard. White light is generated using a 6.5 W quartz-tungsten-halogen lamp powered by a stabilized direct current (DC) supply. This light is collected by a 35 mm focal length $f/0.7$ aspheric lens and imaged onto the entrance slit of the monochromator by a 150 mm focal length $f/3.0$ doublet. The lamp filament sits at the center of curvature of a 50 mm diameter spherical mirror. This mirror images the filament onto itself and increases light intensity at the monochromator 20 percent.

The commercial monochromator is a Czerney-Turner design with 110 mm focal length mirrors and an effective aperture ratio of $f/3.3$. The reflective diffraction grating is ruled at 1200 lines per mm and blazed at 600 nm. Output wavelength is set by rotating the small table on which the grating is mounted. A microprocessor-controlled stepper motor drives a worm gear that rotates the grating table.[70] With a slit width of 125 μm, the output bandpass of the monochromator is about 0.8 nm in wavelength. The slit width was chosen so the fringes for gaps up to 100 μm could be resolved, while still allowing enough light to pass. The monochromator is calibrated using a low-pressure argon gas discharge lamp. The output root-mean-square wavelength accuracy is about 0.2 nm, but it can be much worse if the monochromator is operated at a temperature different from that at which it was calibrated.

Light from the exit slit of the monochromator is relayed to the gap sensor mod-

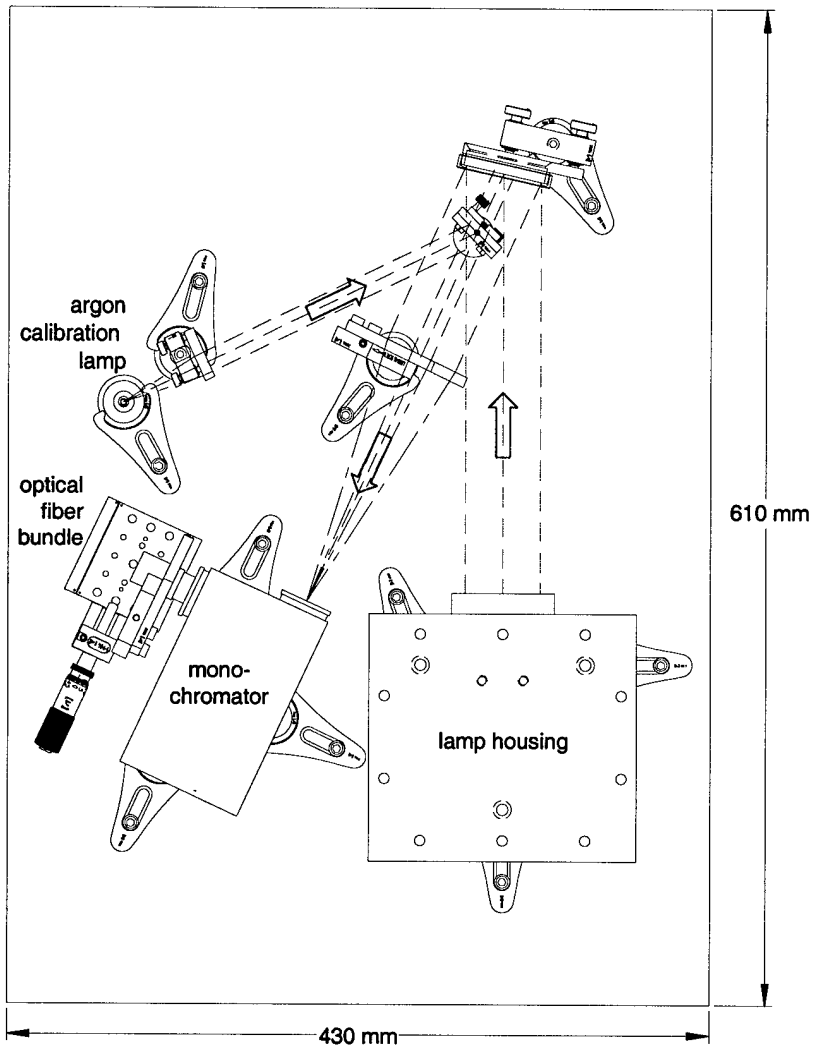

Figure 5.14 Layout of quasi-monochromatic light source. The components are mounted on an optical breadboard that is placed in a standard 19-inch rack. White light from the lamp is collimated by an aspheric lens mounted in the lamp housing. The light is then folded by a turning mirror and focused onto the monochromator entrance slit by an achromatic doublet. The smaller beam shown coming from the left is from a low-pressure argon lamp used to calibrate the monochromator. It is reflected from a flip-up mirror and is imaged onto the monochromator using the same lens as the white light beam. Light exits the monochromator and enters the fiber optic bundle which is mounted on a positioning stage.

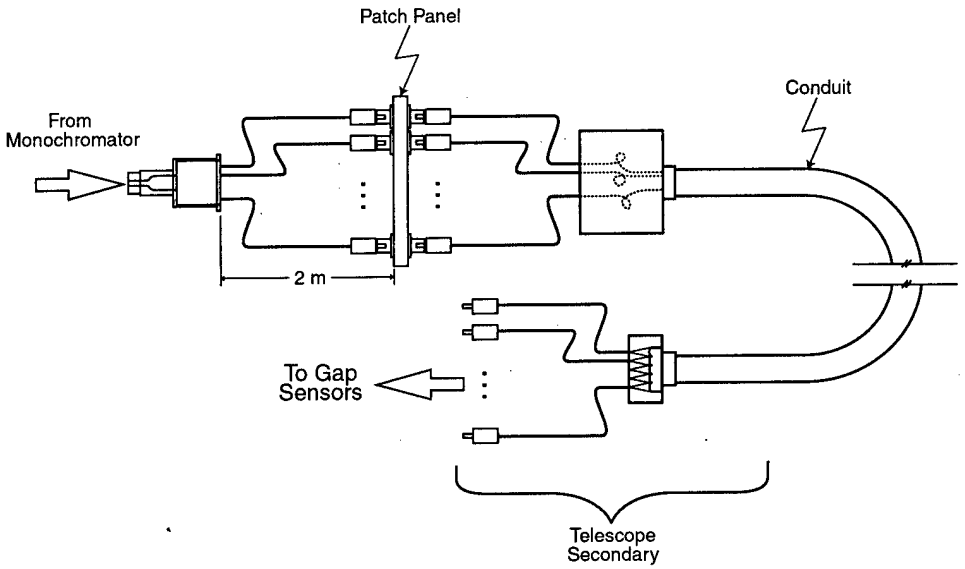

Figure 5.15 Schematic diagram of optical fiber cable assembly. Light from the monochromator enters the fibers which are held in an aluminum ferrule. The ferrule supports and protects the 30 fibers which are placed side-by-side. Attached to the rear of the ferrule is a housing to which is attached 30 lengths of kevlar-reinforced plastic tubing. Each fiber is contained within a separate 2 m length of plastic tubing that is terminated with an FC-type connector. The connector can be attached directly to a gap sensor module, or it can be connected to another FC connector through a mating connector.

ule using a multi-mode optical fiber bundle. The fiber numerical aperture is 0.22, thus it will accept up to an $f/2.3$ beam. The fiber core is 100 μm in diameter and it transmits wavelengths of 0.4–2.0 μm. I have constructed a bundle containing 30 individual fibers placed side-by-side so the 24 gap sensors can be operated simultaneously. The other ends of the fibers are terminated with FC-type connectors and both ends receive an optical polish. This bundle is adequate to support secondary mirror testing at the Mirror Laboratory. A schematic diagram of the optical fiber bundle is shown in Figure 5.15.

To get light from the 6.5 m MMT control room to the back of the secondary mirror, a much longer cable must be added. The cable must not exceed 1 cm in diameter so it can run along the back of one of the secondary mirror spider arms. The

control-room-end of the cable will be terminated with FC connectors and housed in kevlar-reinforced plastic tubing. Some provision must be made to accommodate the differential thermal expansion of the glass fiber and the plastic tubing. I propose a small metal box to which the tubing and the 1 cm diameter conduit are attached. The fiber is free to float within the plastic tubing and the steel-reinforced conduit. The telescope-end of the optical fiber cable poses more of a problem. Installation and removal of the adaptive secondary must be possible without removing the myriad of cables and hoses from the telescope. The connection must be made where the cable enters the secondary, instead of at each individual gap sensor module. This single connector must be compact and align the fiber ends with 10 μm accuracy. In his Ph.D. dissertation, M. Kenworthy describes the method he used to construct compact connectors for multiple optical fibers.[71]

5.4.3 Gap Sensor Modules

Figure 5.16 shows a drawing of a gap sensor module. The overall dimensions are only 22×30 mm. The gap sensor components are mounted in a housing machined from a solid block of aluminum. The fiber optic connector mates with the housing through a modified optical fiber coupler. Light from the fiber is folded by a 5 mm hybrid metal-dielectric beam-splitting cube. The light is then collimated by a 12.7 mm focal length $f/2.0$ achromatic doublet. Both the beam-splitting cube and the lens are anti-reflection coated and are affixed using optical cement. Light reflected from the two surfaces of the gap is collected by the lens and focused through the cube onto the detector. The position of the fiber can be adjusted along its axis, so light reflected back is imaged onto the detector. To control stray light, the interior surfaces of the gap sensor housing are coated with black paint with low reflectivity at wavelengths 0.3–2.4 μm. The gap sensor modules will be mounted to the cold plate, at the rear of the secondary mirror, about 100 mm above the gap to be measured.

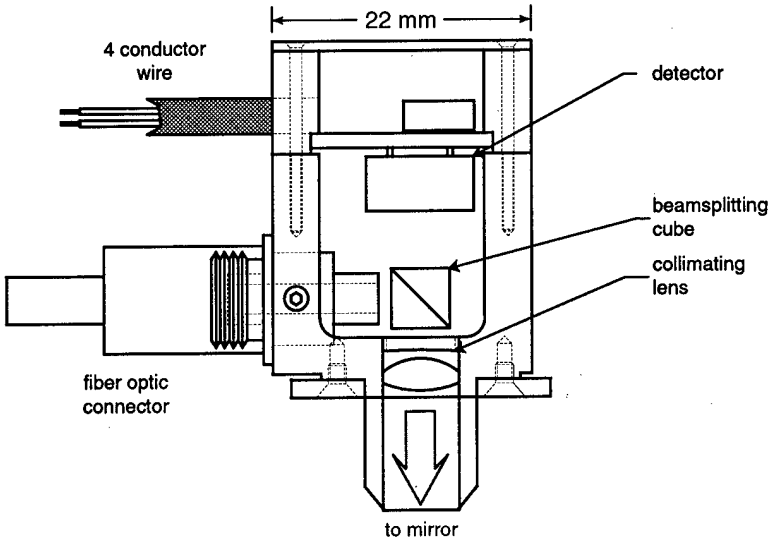

Figure 5.16 Drawing of gap sensor module.

The silicon photodiode detector has a circular active area 2.5 mm in diameter and is operated in photo-voltaic mode. Its response ranges from 0.5–1.05 μm and peaks at about 0.6 A/W at 0.9 μm wavelength. The detector is mounted on a small printed circuit board, which can easily be removed from the module. The two-stage amplifier and other electronic components are surface-mounted for compactness. Power for the electronic circuits is provided by the personal computer through a DC-DC converter. The typically 2 nA current from the detector is amplified to roughly 5 V, thus decreasing the effects of noise pick-up during transmission to the digitizer in the computer.

5.4.4 Signal Digitation and Processing

The electrical signals from the gap sensor modules are digitized by a multi-channel 12-bit analog-to-digital converter in the personal computer. Software in the computer controls the monochromator, reads digitized signal from the detector, and performs the necessary calculations to determine the gap thickness. The software

communicates with the monochromator via an RS-232 serial interface. During operation, the monochromator is commanded to step in wavelength from 550–1050 nm in increments of 0.2 nm. At each step, 64 samples are collected to reduce the effects of electronic noise. The data collection process takes about 35 seconds, in large part determined by the speed of the monochromator. The time required to calculate the gap thickness is negligible.

Gaps up to about 100 μm thick can be measured with this system. As gap thickness increases, the interference fringe spacing decreases. For gap thickness greater than 100 μm, the fringes can not be resolved over the wavelength range sensed by the silicon photodiode. Thicker gaps could be measured using a detector that is sensitive in the infrared. Another option is to use a monochromator with better spectral resolution and light throughput.

The next chapter discusses the construction, alignment, calibration, and testing of the gap sensor system. It includes tests performed on a prototype of the adaptive secondary mirror to calibrate its 36 capacitive position sensors.

Chapter 6

Gap Sensors: Construction, Calibration, and Use

6.1 Introduction

While constructing and calibrating gap sensor components, I encountered several challenges. Some of the problems discovered during construction of the gap sensor modules were solved by employing typical opto-mechanical methods; they are described here to benefit those who may repeat the process. Others problems were unexpected and more complex. Construction of the optical fiber bundle required much experimentation to find the best fabrication techniques. To handle many fragile fibers, some simple yet effective methods were developed. These methods were tested by first building a bundle with 6 optical fibers. This bundle was used with 3 gap sensor modules to test the 36 actuator prototype of the adaptive secondary mirror, P36. Later, a fiber bundle with 30 fibers was fabricated for use with the 336 actuator adaptive secondary mirror.

Calibrating the performance of the gap sensors proved to be a formidable task. To test the accuracy of the gap sensor measurements, I developed a thickness stan-

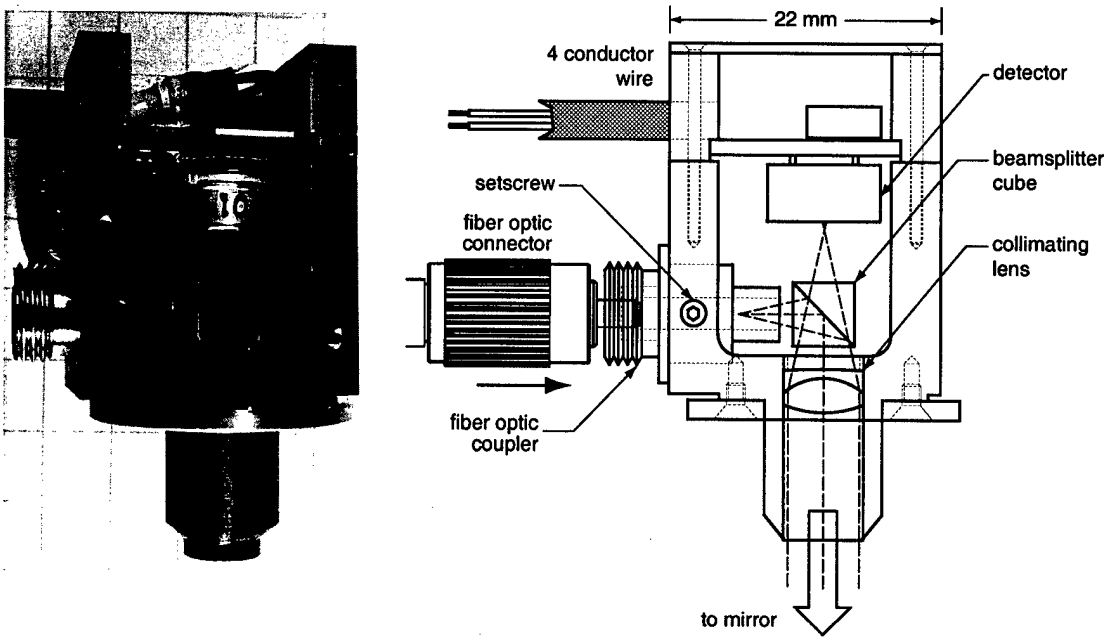

(a) (b)

Figure 6.1 Photograph and schematic diagram of gap sensor components. Light leaves the end of the optical fiber, reflects 90 degrees from the cube beamsplitter, is collimated by the lens, and is projected normal to the mirror surface. Light then reflects back from the mirror and is focused onto the detector by the lens.

dard. Glass micro-spheres were placed between two surfaces to make a gap whose thickness was relatively stable with changes in temperature. I then performed a series of tests which measured the thickness of the film of air between the surfaces of the reference standard. Measurements made with different gap sensors were compared. Various sources of error, in both the monochromator and the fiber bundle, were exposed then eliminated.

6.2 Construction and Alignment of Components

6.2.1 Gap Sensor Modules

The layout of the gap sensor components are shown in Figure 6.1. To help in the

design of the gap sensor, a simple model of the optical components was constructed to determine performance and alignment tolerances. Recall the gap sensor module is mounted on the cold plate whose surface is parallel to, and 100 mm above, the mirror shell. An optical fiber brings light to the gap sensor. A small lens in the gap sensor collimates the light leaving the fiber and projects it towards the mirror. If the fiber is not positioned correctly with respect to the optical axis of the lens, then light from the gap sensor will not be projected normal to the mirror surface; it will not reflect back to the lens. To first order, the angle α of the beam leaving the lens is related to the position of the fiber by

$$\alpha = \frac{\Delta x}{f} \tag{6.1}$$

where f is the focal length of the lens and Δx is the transverse distance between the rear focal point and the fiber. The lens focal length is 12.7 mm and its diameter is 6.35 mm. If we allow the reflected beam to be displaced by 1 mm when it reflects back to the lens, then the angle of the beam is

$$\alpha = \frac{1\,\mathrm{mm}}{2(100\,\mathrm{mm})} = 0.005\,\mathrm{rad} \tag{6.2}$$

where the beam has twice traversed the 100 mm distance to the mirror. Substituting for α in equation (6.1) yields the maximum allowed displacement of the fiber, $\Delta x = 65\ \mu\mathrm{m}$. This influences how the fiber is held in place in the gap sensor.

In anticipation of the possibility of broken optical fibers, I decided not to make the optical fiber a permanent part of the gap sensor. A coupler was used to allow the exchange of fibers. Commercially-available couplers are made to align two fiber connectors to each other with a precision of a few microns. The coupler used, shown in Figure 6.2 (a), was modified by removing some of its threads. These threads were not required, as the connector is held in place with small setscrew. The coupler contained a floating bronze sleeve into which the fiber connector slid, as shown in

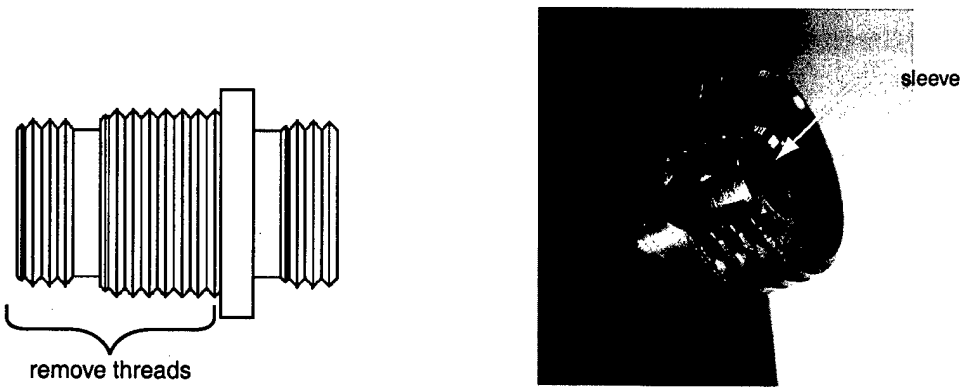

(a) (b)

Figure 6.2 Fiber optic coupler. Figure (a) shows the threads that were removed to allow axial positioning of the fiber end. The coupler is held in the gap sensor module with a small setscrew. Figure (b) shows the bronze sleeve that was secured with epoxy adhesive, preventing the fiber end from moving freely. This maintains the alignment of the optical fiber with respect to the lens in the gap sensor module.

Figure 6.2 (b). When the coupler was used to hold a single fiber connector, the floating sleeve allowed the fiber to move freely—about ±0.5 mm. To solve this problem, the sleeve was fixed in place with epoxy adhesive. A spare connector, coated with a releasing agent, was used to position the sleeve while the epoxy cured.

Before the gap sensor assembly could begin, I coated the interior of each module with a light-absorbing paint. I performed tests to show the paint effectively absorbs light from the ultraviolet through the near-infrared. The paint was essential in preventing light from going through the beamsplitter cube, scattering from the interior of the module, then reflecting from the cube directly into the detector. This scattered light would mask the light reflected from the thin film being measured. The next step in assembling the gap sensor modules was to install the optical components. Before positioning the beamsplitter cube, I installed the modified fiber coupler and the lens. The coupler is fixed in the gap sensor module with a small

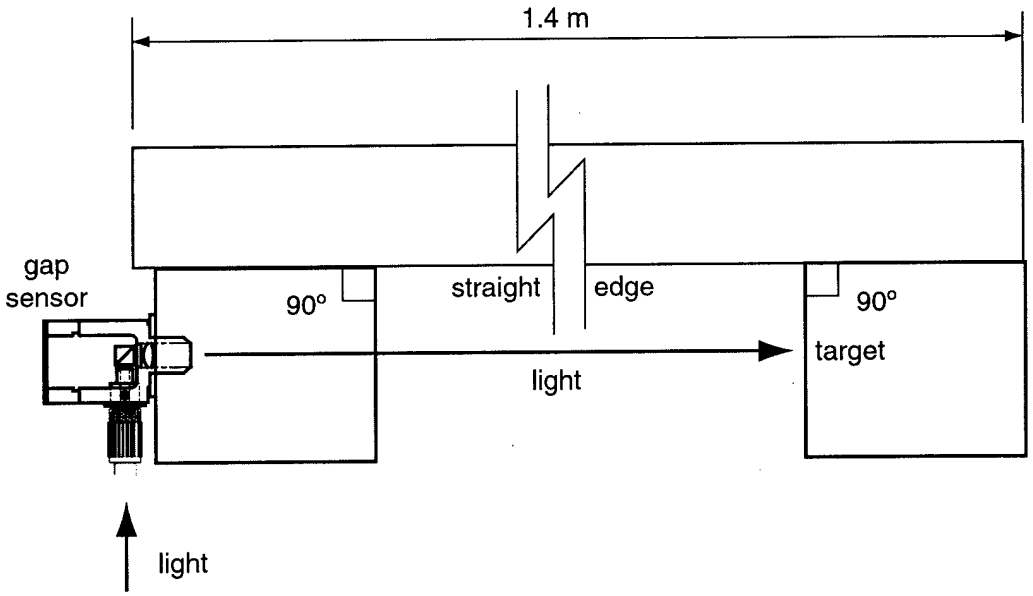

Figure 6.3 Drawing of beamsplitter cube alignment fixture.

setscrew. The lens is held in place with a retaining ring that centers the lens in its barrel.

To aid in aligning the cube to the fiber and the lens, a special alignment fixture was fabricated. Figure 6.3 is a drawing of the alignment fixture. The fixture consisted of two blocks of precision-machined aluminum; one block held a gap sensor and the other held an alignment target. The blocks placed the gap sensor and the target perpendicular to, and equidistant from, a straight edge. Optical tests confirmed the 90 degree angles in the block were accurate to better than 0.1 degrees or 0.0016 radians. The beamsplitter cube was attached to a stage that adjusted its position in six axes. Light from a helium-neon laser was sent through a fiber which was connected to the gap sensor module. I adjusted the position of the cube while observing the location of the beam on the distant target. At the same time, the fiber was adjusted axially, by moving the coupler, to collimate the light leaving the lens. Finally, the beamsplitter cube was affixed with ultraviolet-curing optical cement. This allowed ample time to position the cube before the adhesive was cured. The

position of the beam at the target was monitored while the adhesive cured to ensure shrinkage of the adhesive did not change the cube alignment.

After the optical components were installed, I inserted the detector to complete the gap sensor assembly. The detector is mounted on a tiny printed circuit board which can be removed from the gap sensor. The board slides into a small groove machined into sides of the gap sensor module. A photograph of the board with its surface-mount electronic components, and a schematic diagram of the circuit are shown in Figure 6.4. The silicon photodiode is operated in photovoltaic mode, where no bias voltage is applied. The photocurrent from the detector is measured by an operational amplifier, whose signal is amplified by another operational amplifier. Power for the amplifiers, ± 15 V, is provided through shielded cable and a compact connector. The output signal also passes through this connector. A series of tests were conducted to determine the best way to make the electronic connections between the gap sensor modules, power supply, and analog-to-digital converter. Various configurations were tested and the noise characteristics of the signal were examined for each. A description of those tests and the results follows.

To begin the noise tests, I mounted a prototype gap sensor on a large optical table; electronic isolation was maintained from the table. Light from the monochromator was sent to the gap sensor via a single multi-mode optical fiber. The 750 nm light from the gap sensor was reflected from a metal-coated mirror back into the gap sensor. Next, the signal from the gap sensor was digitized at 1000 samples per second for 9 seconds by an analog-to-digital converter in a personal computer. The five configurations tested are listed in Table 6.1; three used differential measurements and two used single-ended measurements. As shown in Figure 6.5, differential measurements were made by digitizing the signal from two inputs, the detector and the power supply common, each measured relative to a common reference. Differential

(a)

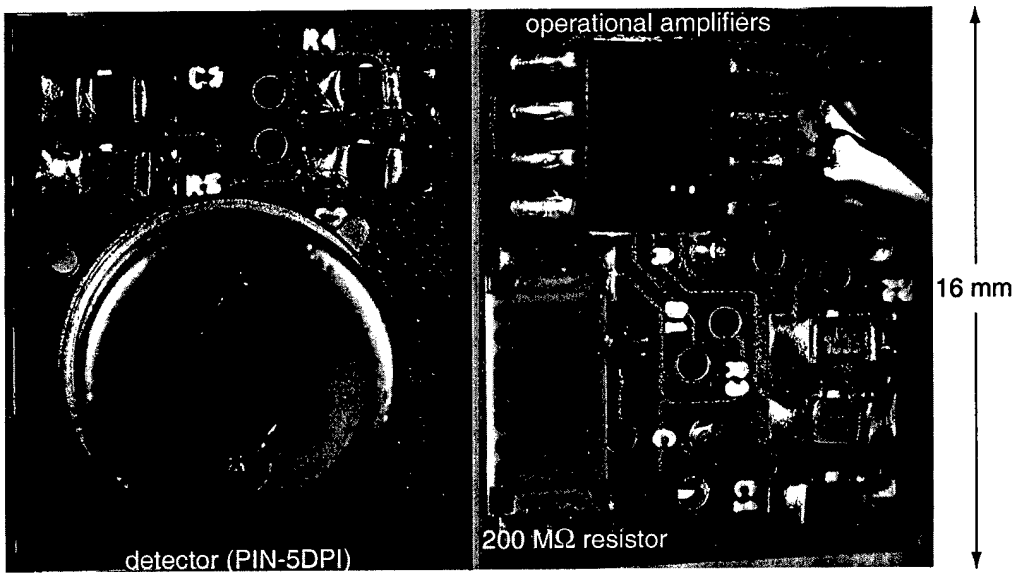

(b)

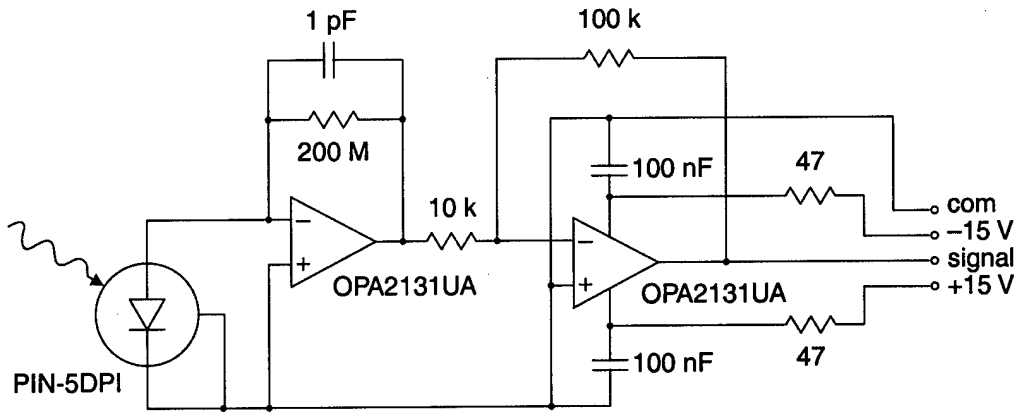

Figure 6.4 Gap sensor printed circuit board. Figure (a) is a photograph showing both sides of the board. Figure (b) is a schematic diagram of the circuit.

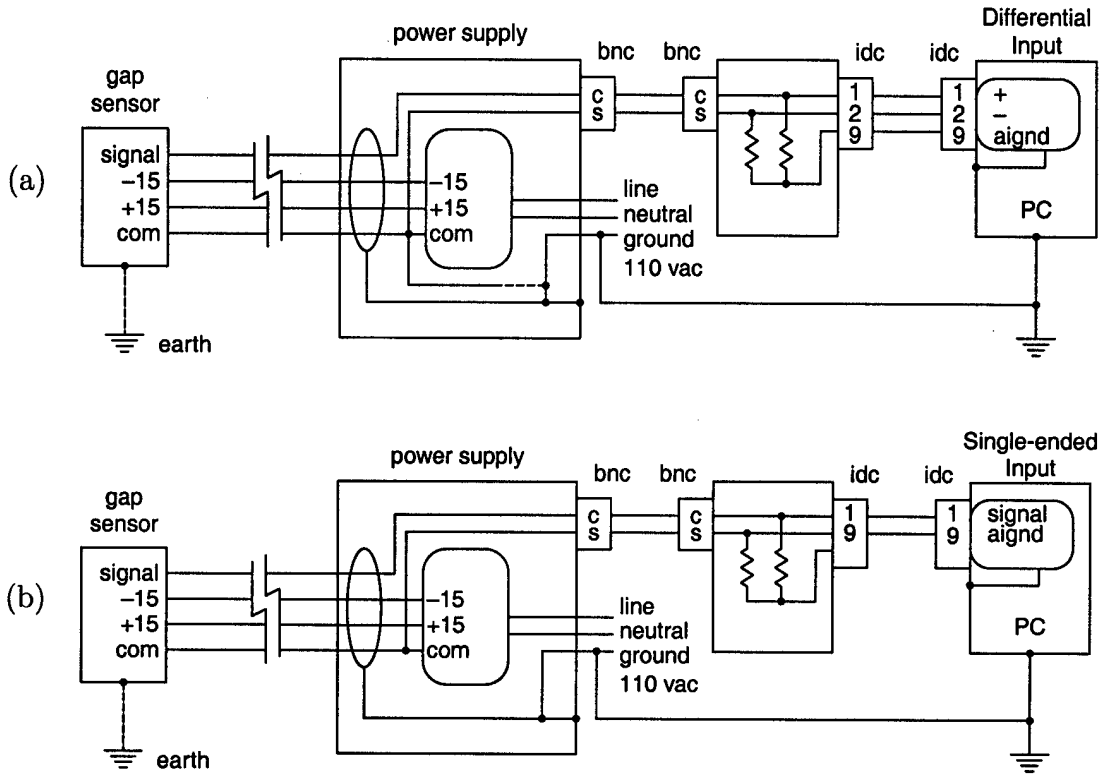

Figure 6.5 Electronic connections for gap sensor grounding test. Figure (a) is a schematic diagram showing connections for differential measurements; Figure (b) shows connections for single-ended measurements. The dotted lines represent connections that were left open in some of the tests.

config.	type[a]	connections			SNR
		shield	case	PS common[b]	
1	diff	AC ground	bldg. ground	open	1.1
2	diff	AC ground	bldg. ground	AC ground	143.4
3	diff	AC ground	open	AC ground	128.3
4	sngl	AC ground	open	AIGND	130.8
5	sngl	AC ground	bldg. ground	AIGND	138.6

[a] diff = differential, sngl = single-ended

[b] PS = power supply, AIGND = analog input ground

Table 6.1 Signal-to-noise ratio (SNR) for different grounding configurations. Because it uses fewer analog-to-digital channels, configuration 5 was chosen. Schematic diagrams of the configurations are given in Figure 6.5.

measurements have the advantage of rejecting noise that is picked-up by the long signal cable connected to each gap sensor. Single-ended measurements were made by digitizing the signal from only one input, the detector. Single-ended measurements require half the number of analog-to-digital channels of differential measurements.

After the data were collected, I calculated the signal-to-noise ratio (SNR) by dividing the mean signal by its standard deviation. The spectrum of each signal was then computed, using a Fourier transform, to discern the source of any noise. Configurations 3 and 4 displayed a very strong 60 Hz component, while configuration 1 displayed strong components at all frequencies. I implemented configuration 5—its SNR was only slightly less than configuration 2 and it required half as many analog-to-digital channels.

6.2.2 Optical Fiber Bundle

The purpose of the optical fiber bundle is to transport light from the monochromator, over a relatively long distance, to each of the gap sensor modules. The fiber

bundle consists of many fibers, placed side-by-side, with their ends aligned. It is held firmly at the exit slit of the monochromator by a mount that allows its position to be adjusted relative to the exit slit. The monochromator exit slit is 4 mm $\times$ 125 μm. The optical fiber consists of three concentric layers: a 105 μm diameter core, an 8 μm thick clad, and an 11 μm thick protective buffer. The outer diameter of the optical fiber is about 143 μm.

If the fibers are packed closely, at least 26 will fit within the length of the monochromator slit. This implies 2 fibers can be damaged, leaving 24 fibers to carry light to the gap sensors; not a large margin for error. If the buffer coating is removed, 30 fibers would fit within the monochromator slit. This would allow damage of up to 6 fibers and leave enough fibers for all the gap sensors. The polyamide buffer was, however, difficult to remove. Three methods were attempted: baking in a 400°C oven, burning with a flame, and bathing in 100°C sulfuric acid. The first two methods removed the buffer, but left the glass fiber brittle; the acid bath failed to remove the buffer. The buffer was left in place as it protected the fiber from damage in the first place. It was better to have 26 robust fibers than to have 30 brittle fibers. Actually, 30 robust fibers is best, for if a fiber at the edge of the bundle is damaged, the bundle can be moved to use a fiber from the opposite edge.

The fiber bundle components are illustrated in Figure 6.6. The fibers are held in place by two pieces of machined aluminum; the aluminum pieces were joined with screws. Plastic shims, 0.005 inches thick, were inserted between the aluminum pieces to maintain space for the fibers. An epoxy adhesive, formulated for use with optical fibers, was used to fill the voids between the fibers. Kevlar-reinforced protective tubing for each of the fibers was secured at the rear of the bundle in 3 rows of 10 tubes.

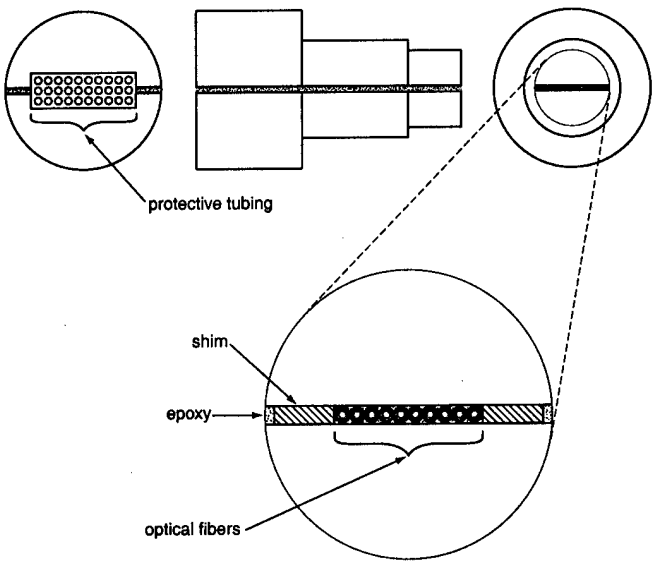

Figure 6.6 Schematic drawing of the fiber bundle. The drawing is not to scale; the fibers are enlarged for clarity. Only 10 fibers are shown; actually, there are 30 fibers in the bundle.

Figure 6.7 includes photographs showing the assembly process. First, one of the aluminum pieces was temporarily secured to a workbench. Next, I laid the fibers side-by-side and held them in place using Post-It™ Notes. The adhesive was sticky enough to hold the fibers yet still allow them to be repositioned. A thin layer of epoxy adhesive was then applied. After the epoxy cured, I threaded the fibers through the protective tubes. A second thin layer of epoxy adhesive was added, then the other aluminum piece was attached to the first, with plastic shims for spacing. A small bead of epoxy was applied to the front of the assembly, at the base of the protruding fibers. This would support the fibers during the polishing process to follow. I heated the fiber bundle to 65°C for 60 minutes to ensure a full cure of the epoxy. I then trimmed the ends of the fibers protruding from the front of the bundle using a diamond-tipped tool. Next, the fibers were polished by hand using four grades of abrasive. A special chuck was used to hold the fiber bundle perpendicular to the polishing surface. The steel chuck was fabricated to allow

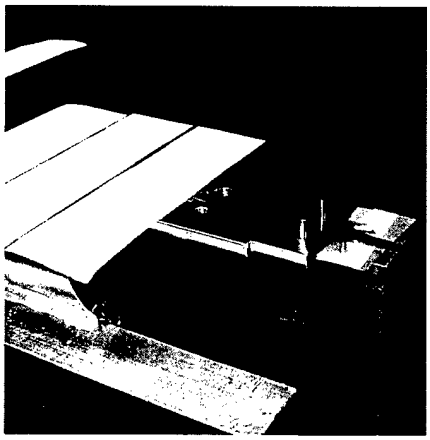

(a)

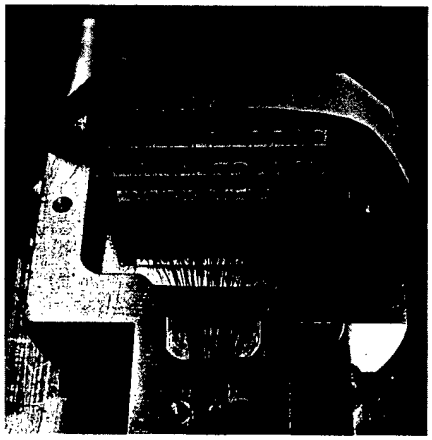

(b)

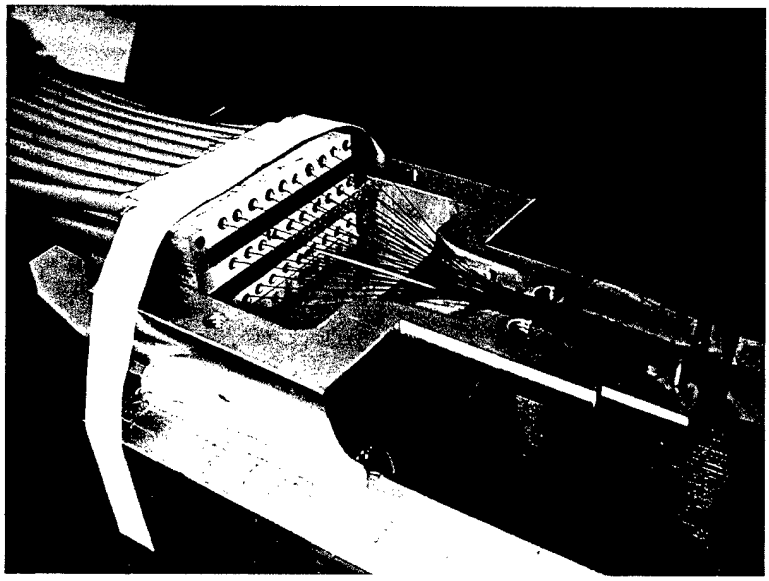

(c)

Figure 6.7 Photographs of the fiber bundle assembly process. Figure (a) shows the fibers held in place with Post-It™ Notes while the epoxy adhesive is curing. Figure (b) shows the protective tubing assembly in place after the epoxy has cured. Figure (c) is a view of the of the fiber bundle ready to receive the top aluminum piece.

control of pressure between the fiber ends and the abrasive surface during polishing. A photograph of the end of the completed fiber bundle is shown in Figure 6.8. Finally, connectors were attached to other ends of each of the individual fibers and the ends were polished using standard techniques. Figure 6.9 shows a photograph of the completed fiber bundle.

After the fiber bundle was assembled and the fibers were polished, I tested the throughput of the fibers. To start, I carefully aligned the fiber bundle to the monochromator exit slit. The fiber bundle is held in a mount that allows it to be adjusted in three translational axes and one rotational axis. First, I brought the end of the fiber bundle to the plane of the exit slit. Next, I adjusted the lateral translation, perpendicular to the slit, by maximizing the intensity from the middle few fibers. The fiber closest to the rotational axis, call it fiber r, was found by rotating the bundle and noting the fiber whose intensity changed the least. The bundle was then translated laterally, parallel to the slit, to bring fiber r to the rotational axis. I next located two fibers an equal distance on either side of fiber r. Then, the rotational angle of the bundle was set by equalizing the intensity on these two fibers. Finally, I made a small lateral translation perpendicular to the slit to maximize the intensity on fiber r. The throughput on each fiber was measured at a wavelength of 650 nm. The results are shown in Figure 6.10. If we assume the illumination was uniform, we can see the fiber bundle was probably slightly rotated; fiber number 15 was at the center of the slit. The median intensity was 7 nW with 25 fibers transmitting over 5 nW.[†] Given the exit slit is 4 mm long, the mean space between each of the 25 central fibers is about 18 μm.

[†]The gap sensor detector electronics were designed to measure a reflected intensity of 3 nW.

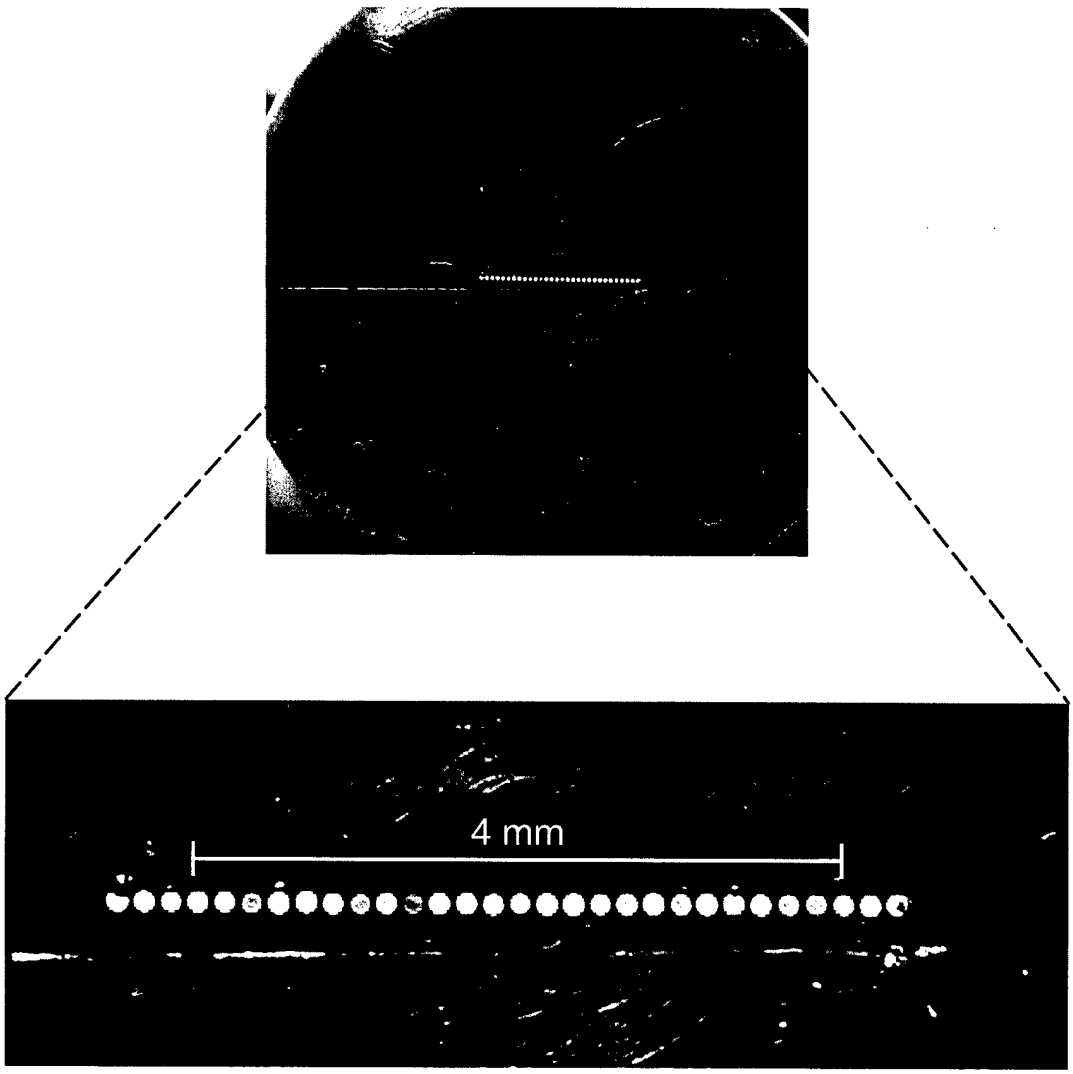

Figure 6.8 Photographs showing the monochromator end of the fiber bundle. Approximately 25 fibers fit within the 4 mm length of the monochromator exit slit.

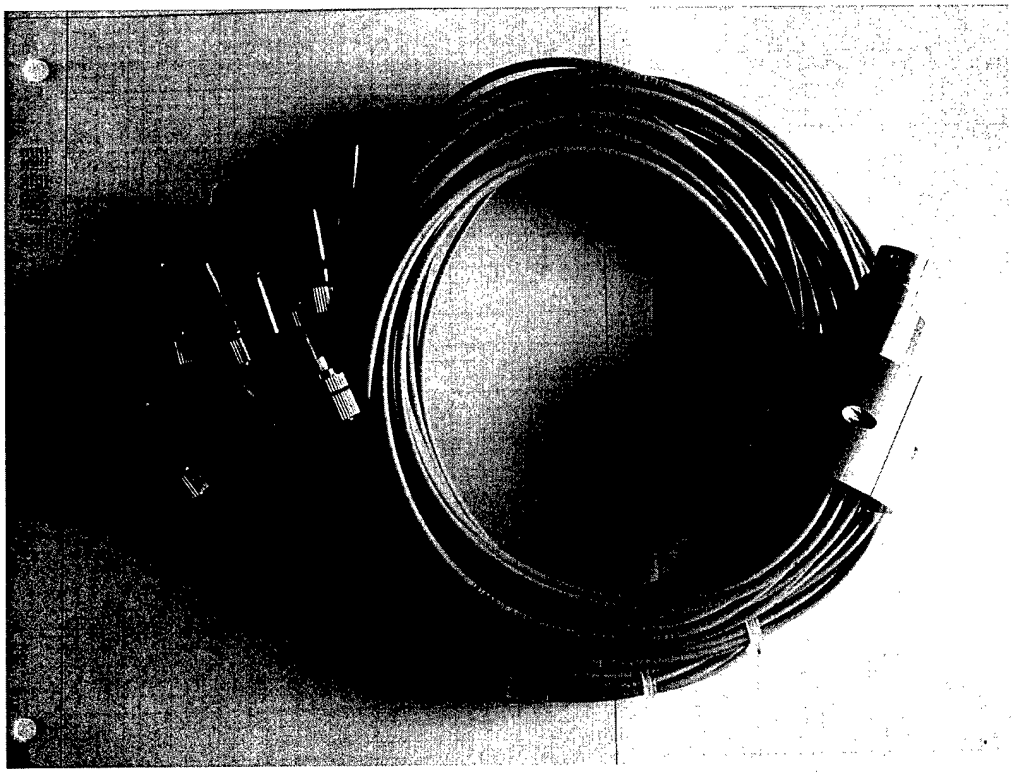

Figure 6.9 Photograph of the completed fiber bundle. A protective cover was removed from one fiber to show the connector.

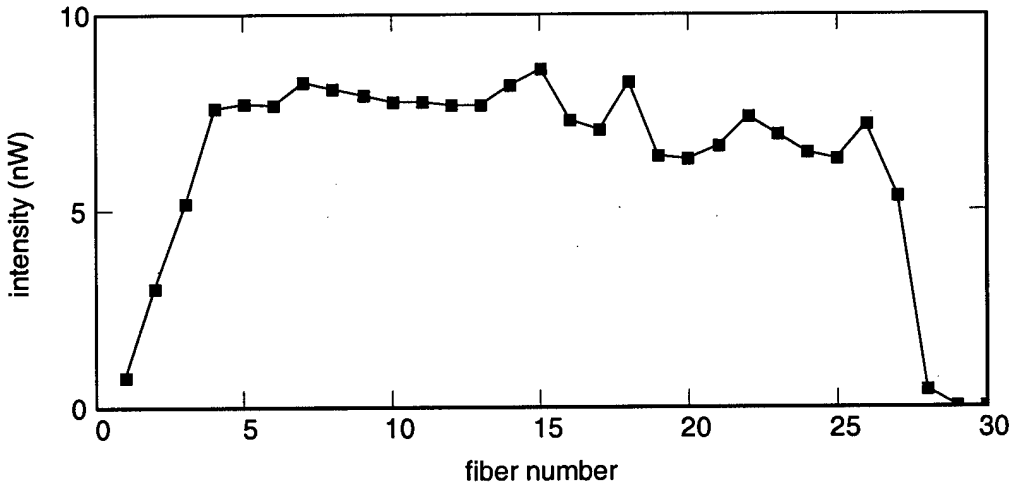

Figure 6.10 Light intensity transmitted by the 30 fiber bundle. The fiber bundle was aligned to the 4 mm long exit slit of the monochromator. The median intensity was 7 nW with 25 fibers transmitting over 5 nW.

6.2.3 Gap Thickness Standard

To test the accuracy of the gap sensor system, a nominally 40 μm thickness standard had to be procured or fabricated. An *absolute* standard, whose thickness was known to a few nanometers, would provide the best measure of gap sensor accuracy. Commercial optics firms could fabricate a stable absolute thickness standard, using techniques for making Fabry-Perot etalons, but their high cost and long lead time made them unattractive. As an alternative, a *reference* standard, whose thickness was not known, but was stable to a few nanometers, would allow the relative accuracy of the gap sensors to be determined. Measurements using different gap sensors could be compared.

I made the first reference standard by joining two fused silica windows with epoxy adhesive. The 25 mm diameter, 6.5 mm thick windows were placed in tip-tilt mounts, brought into contact, and illuminated with monochromatic light at 546 nm from a mercury source. One window was mounted on a translation stage driven by a micrometer. The vernier scale on the micrometer was marked in increments of 10 μm. I slowly increased the spacing between the windows to about 50 μm while keeping their faces parallel by observing Newton's fringes. Using a gap sensor, I verified the approximate separation between the windows. The two windows were then joined using a two-part epoxy adhesive. The coefficient of thermal expansion of the epoxy is about $45 \times 10^{-6}/°C$; thus, a temperature change of 2°C results in a change in gap thickness of about 5 nm for a 50 μm gap. This epoxy thickness standard is suitable for comparisons of gap measurements made at about the same temperature.

To make a reference standard which could be used at a greater range of temperatures, I took a different approach. Professor James Burge suggested I use glass micro-spheres to set the separation between the windows.[72] I obtained a sample

of micro-spheres which were made from boro-silicate glass with a thermal expansion coefficient of $2.8 \times 10^{-6}/°C$. The manufacturer stated 95 percent of the spheres would be less than 65 μm in diameter. The assembly process was less complicated than the assembly of epoxy standard. To more closely approximate the fringes that would be observed with the real adaptive secondary mirror, I selected windows with metal coatings. Windows with thin metal films are commercially available in the form of neutral density filters. They are typically coated with an alloy of chromium, iron, and nickel. Of course, small mirrors with thick aluminum coatings are also readily available. I mixed several thousand of the glass micro-spheres with an ultraviolet-curing adhesive. This mixture was applied to three places at the edge of the mirror; the neutral density filter was placed on top. Because the adhesive shrank as it cured, the glass micro-spheres determined the separation of the two surfaces. The surfaces were illuminated with monochromatic light to verify they were parallel. Photographs of both thickness standards are shown in Figure 6.11.

6.3 Gap Sensor Calibration

Before the reflectance fringes recorded by the gap sensors could be used to calculate the thickness of a transparent film, I applied several corrections to the measurements. This section explains how each of the corrections were implemented to improve the accuracy of the gap thickness measurements. The first correction was to account for variations with wavelength of several components: the intensity of the incandescent source, the throughput of the monochromator, and the response of the detector. Because the gap sensors were designed to measure thickness to an accuracy of a few nanometers, thermal expansion was an important factor to consider during testing. Adjustments were made to minimize the effects of thermal expansion in the monochromator and the test standards. Next, it was observed the optical fibers in

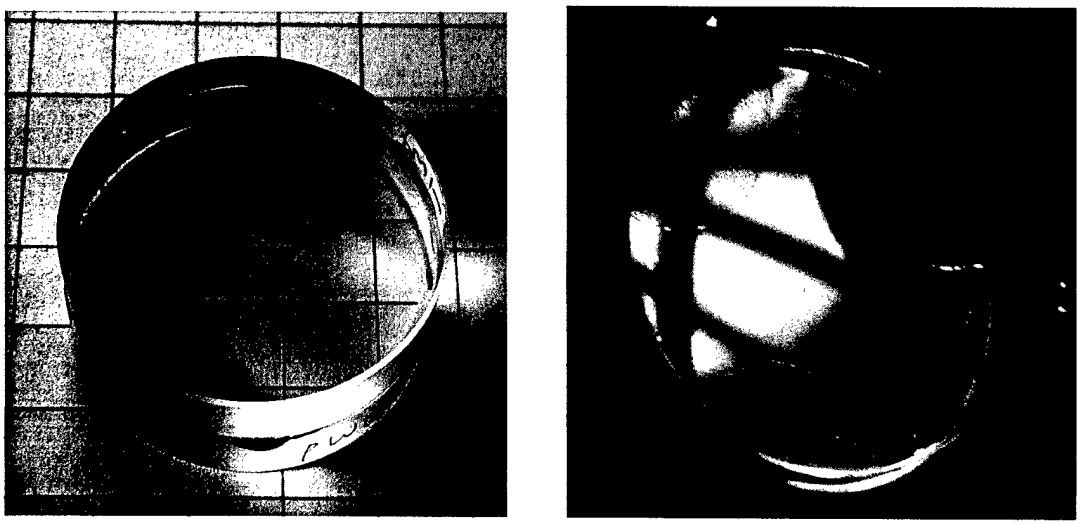

(a) (b)

Figure 6.11 Photographs of the two thickness reference standards. Figure (a) shows the reference standard made with epoxy adhesive; Figure (b) shows the reference standard made with glass micro-spheres. Both are about 25 mm in diameter.

the fiber bundle were not exactly in a line. Slight variations in their alignment to the monochromator slit caused each fiber to transmit a slightly different wavelength. This led to imprecise gap thickness measurements. I devised a method to measure the misalignment of each fiber and compensate the measurements polychromatic reflectance. These corrections reduced the largest errors in gap thickness measurement. At the end of this section, I present some minor corrections which may be explored.

6.3.1 Correction for System Efficiency

The gap sensor system contains many components whose efficiency or performance varies as the wavelength is changed. The brightness of the white light source, the transmittance of the optics, and the response of the detector all depend on wavelength. To measure the polychromatic reflectance of a thin film, a correction for these variations should be applied. This was done by first recording the signal reflected from two surfaces which were relatively widely separated—many times greater than the coherence length of the quasi-monochromatic illumination. Interference effects disappear for films much thicker than the coherence length of the illumination. The coherence length l_c is calculated from the bandwidth passed by the monochromator $\Delta\lambda$ and the wavelength λ

$$\begin{aligned} l_c &= \lambda^2/\Delta\lambda \\ &= (750\,\text{nm})^2/(0.8\,\text{nm}) \\ &\approx 0.7\,\text{mm}. \end{aligned} \tag{6.3}$$

I placed the surfaces a few millimeters apart, then I recorded the reflected intensity as the wavelength was changed. This correction is illustrated in Figure 6.12 (a). The heavy line is the polychromatic intensity recorded from a very thick gap; the thin line is the intensity recorded from a narrow gap, whose thickness is to be measured. Figure 6.12 (b) shows the result of dividing the signal recorded from the narrow gap

by the signal from the very thick gap. This quotient is directly proportional to the reflectance. By applying the methods developed in Chapter 5, I can then measure the gap thickness.

6.3.2 Compensation for Thermal Expansion

The first gap measurements revealed the effects of thermal expansion on thickness measurements at nanometer resolution. The first measurements were made with a prototype gap sensor module and the epoxy reference standard. The goal of this test was to determine the repeatability of thickness measurements made in quick succession, much as the gap sensors will be used when calibrating the capacitive sensors. I made a series of 26 measurements at intervals of about 1.5 minutes between measurements. About 35 minutes later, a short series of 5 measurements was taken. The gap thickness measurements are plotted in Figure 6.13 along with a least-squares linear fit to the first series. The root-mean-square (RMS) residual of the fit is 0.13 nm. Clearly there is a decreasing trend in the gap measurements—1.3 nm over 38 minutes.[‡] Change in the gap thickness from thermal contraction of the epoxy was probably not the cause, for the temperature of the reference standard was constant to within 0.1°C. After the system was allowed to sit idle for 35 minutes, the measured thickness returned to the values of the first series of measurements. This suggested the decreasing trend in the measurements may have been caused by heating of some component as the data were collected.

One explanation for the trend could be traced to heating in the monochromator. The steel worm gear that drives the monochromator grating was heated by the stepper motor. A lengthening of the worm gear would introduce an error in output wavelength of the monochromator proportional to the commanded wavelength.

[‡]The calibration error budget for the capacitive sensors allows a drift of 2 nm per hour in gap sensor measurements.[73]

(a)

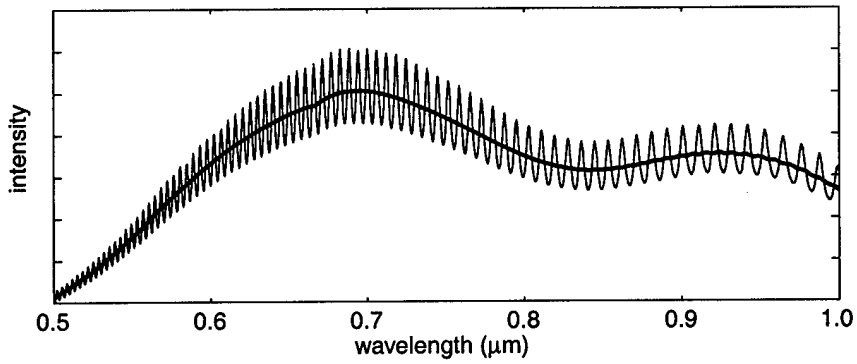

(b)

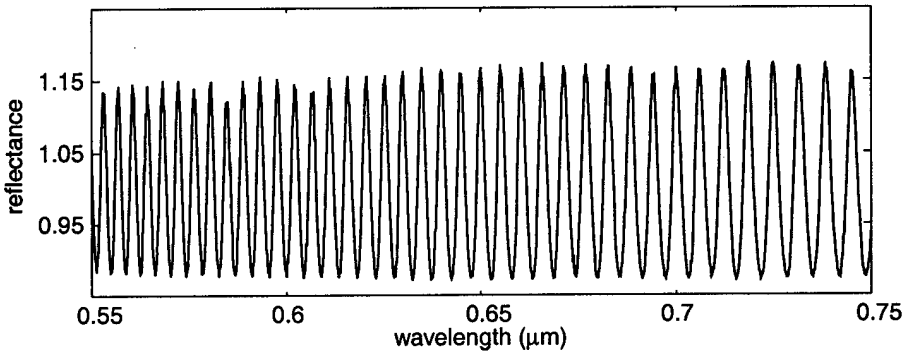

Figure 6.12 Correction of gap sensor signal for wavelength-dependent variations. Figure (a) shows the digitized intensity measured by the gap sensor. The heavy line is the polychromatic intensity recorded from a very thick gap; the thin line is the intensity recorded from a narrow gap. The peak around 700 nm in the thick curve is probably from a combination of the diffraction grating and the incandescent lamp. The grating is blazed for 600 nm; the spectral radiance curve for a 3500 kelvin blackbody has a maximum around 700 nm. The peak at 900 nm represents the peak response of the detector. Figure (b) shows the result of dividing the signal recorded from the narrow gap by the signal from the very thick gap. Only a portion of the wavelength range is shown for clarity.

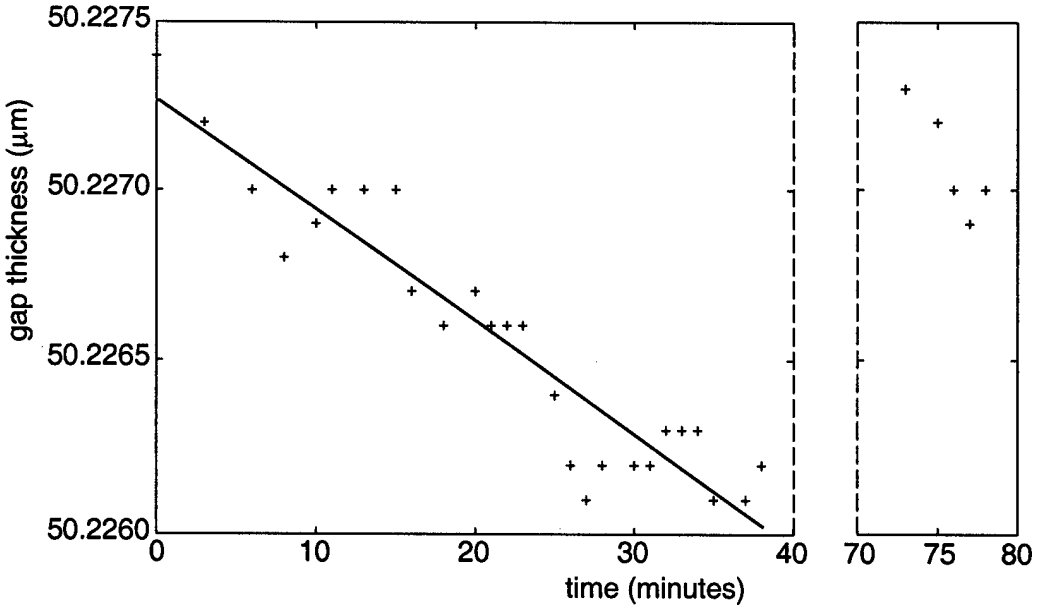

Figure 6.13 Gap thickness measurements of the epoxy reference standard. The first 26 measurements were taken in succession at 1.5 minute intervals; a second series of 5 measurements was taken about 35 minutes later. The range of the first series is about 1.3 nm. The solid line is a fit of the first series; the residual of the fit is 0.13 nm RMS.

Through modeling, I found that a linear increase in output wavelength by a factor of 3×10^{-5}, that is, 0.023 nm at 750 nm wavelength, caused a decrease in the gap measurement of 1.5 nm. To test the hypothesis that heating could cause the output wavelength to shift, I first used the monochromator, at room temperature, to measure the spectral output of an argon calibration lamp.[§] Next, the monochromator was slowly heated to 10°C above room temperature and the spectrum was again recorded. I compared this spectrum to the one recorded at room temperature. After heating of the monochromator, the argon lines shifted, towards longer wavelengths, by 0.5 nm on average. Clearly, a temperature increase much smaller than this, 0.5°C if the expansion of the worm gear is linear with temperature, could account for the trend in measured gap thickness. I later found that removing the metal cover on the

[§]Low-pressure gas discharge lamps have sharp emission lines which are stable in wavelength.

monochromator and providing ventilation with a fan helped to eliminate the drift in gap thickness measurements.

The next step in testing the gap sensors was to compare simultaneous measurements made with several gap sensors using the optical fiber bundle. Since I had only two reference standards, I could test at most two gap sensors at once. I sought to quickly build a stable reference standard which would allow testing of several gap sensors at once. I obtained two promising optical elements: a 40 mm thick, 160 × 220 mm elliptical flat mirror and a 10 mm thick, 125 × 250 mm rectangular glass window. The mirror was made of Pyrex and the window was BK7. The mirror was placed on a vibration-isolated optical table. A thin layer of thermally conducting material was placed between the table and the mirror to reduce thermal gradients in the thick mirror. Plastic shims, 50 μm thick, were positioned on the mirror and the window was placed on top. Illumination with monochromatic light from a mercury lamp, $\lambda = 546\,\text{nm}$, revealed about 8 fringes of tilt over 100 mm and a slight curvature between the two surfaces; the fringes showed astigmatism. The surfaces were concave, for the circular fringes contracted when pressure was applied to the center of the window. An aluminum plate with holes to accommodate 8 gap sensors was suspended over the window. The gap sensors were evenly spaced in 2 rows of 4 gap sensors, as shown in Figure 6.14. Since the gap was not uniform in thickness, a series of measurements would be made with each gap sensor rotated through each position, so their performance could be compared.

The thin film of air between the surfaces was measured 35 times over 70 minutes by each of the 8 gap sensors. The results are shown in Figure 6.15. The arrangement of the graphs corresponds to the arrangement of the gap sensors over the window. We see the sensors at positions 3 and 4 measured a gap 2 μm thicker than the gap measured by sensors at positions 0 and 7. This agreed with my earlier observation of

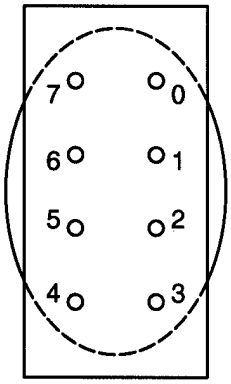

Figure 6.14 Arrangement of gap sensors for the measurements shown in Figure 6.15. The circles represent the positions of the gap sensors.

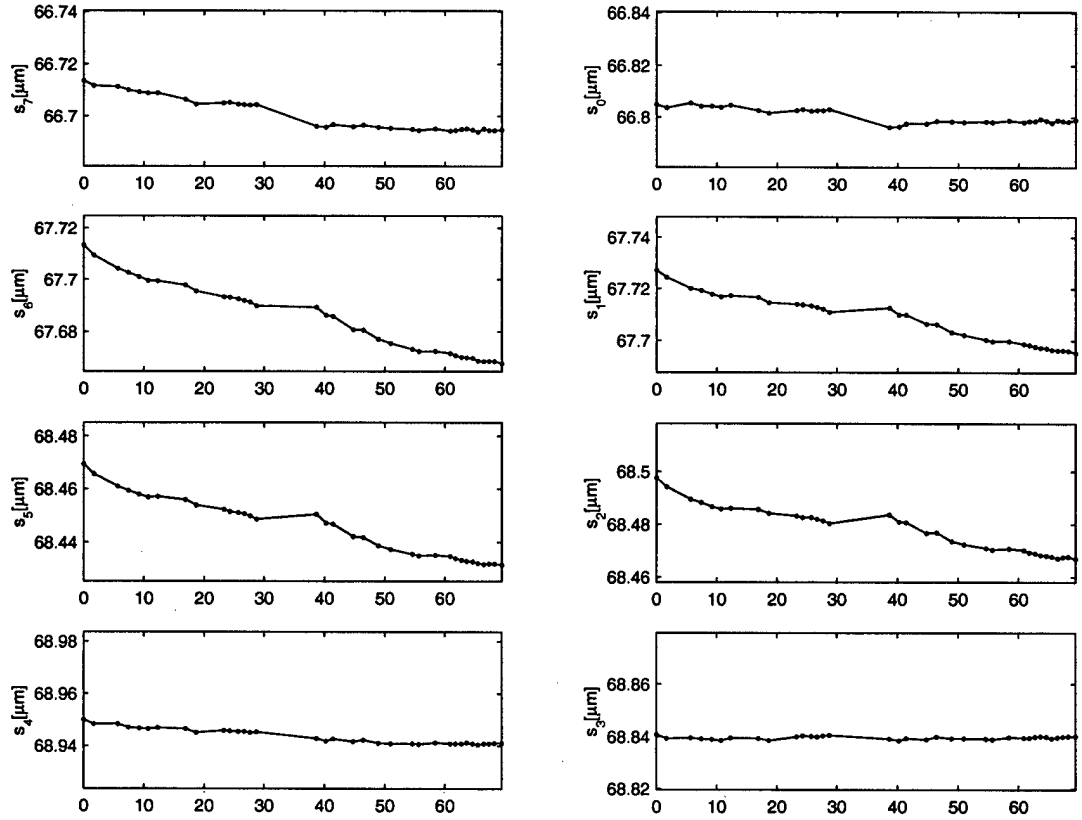

Figure 6.15 Gap thickness measurements of an air film between two surfaces. Eight measurements were repeated 35 times over 70 minutes. The horizontal axis shows time in minutes. There was about 2 μm of wedge between the surfaces. The 4 gap sensors near the center of the window measured gaps that appeared to change more quickly than the gap sensors near the ends.

8 fringes of wedge between the surfaces. More troubling, however, was the apparent change in gap thickness over time. The 4 gap sensors near the center of the window measured gaps which appeared to change more quickly than the gaps measured by the sensors near the ends. The change in thickness was about 30 nm over 70 minutes. This was much greater than the 1.3 nm drift noted in tests with the reference standard. To determine if the gap was actually changing in thickness or if the apparent change was due to some artifact of the gap sensor system, I switched the positions of some of the gap sensors. I repeated the series of measurements the next day. The results were essentially unchanged; the gap sensors measured about the same thickness at each position and the trend in the measured thickness was remarkably similar. How could I observe the same pattern of gap thickness changes the next day?

A new test was devised to determine if the gap thickness was actually changing. Instead of the monochromator, a helium-neon laser, $\lambda = 594\,\text{nm}$, was used as a light source for a gap sensor. I scanned the gap sensor over a small part of the window and noted the locations of the fringe minima and maxima. I repeated this process several times over three days. I found there was a general drift in fringe position over a day; this drift repeated the next day. Counting the number of fringes over a given distance gave the angle of wedge between the surfaces. Given the wedge angle and the distance the fringes moved, I calculated the change in gap thickness. I discovered changes in gap thickness up to 20 nm per hour. This explained the changes in gap thickness measured by the gap sensors.

The gap between the surfaces could have changed due to differential heating in the glass parts. If the glass window had a radial temperature profile, warmer at the edges than at the center, its cross-section would be similar to a very weak negative lens. Recall, Newton's fringes showed the gap between the surfaces was thicker in

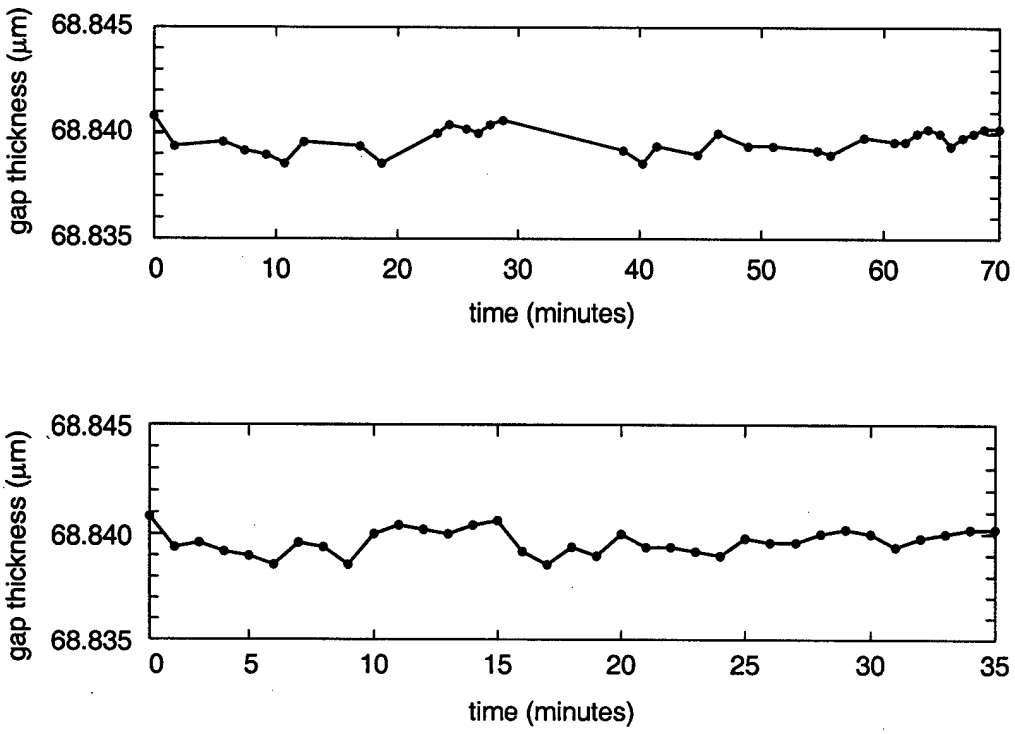

Figure 6.16 Two series of gap thickness measurements of an air film. The measurements were made on two days, with different gap sensors used each day.

the middle. The thermal expansion coefficient of BK7 is $7 \times 10^{-6}/°C$ and for Pyrex it is $3 \times 10^{-6}/°C$; thus, a 0.1°C temperature change over the surfaces yields a 16 nm change in gap thickness. Unfortunately, this arrangement could not be used to compare thickness measurements made with different gap sensors, unless the temperature was made very uniform. This test series did, however, yield some valuable information. Note the gap thickness measured at position 3. Expanded plots of thickness measurements at position 3 are shown in Figure 6.16. The measurements were made on two days with different gap sensors used each day. Position 3 was adjacent to one of the shims which separated the surfaces, hence, the gap thickness was nearly constant. The measurements range over 2 nm, but there is no trend towards decreasing gap thickness.

6.3.3 Correction for Optical Fiber Misalignment

The wavelength of light in the exit plane of a monochromator varies with position lateral to the exit slit. If the ends of the optical fibers in the fiber bundle are not exactly in a line, each fiber will transmit a slightly different wavelength. Small variations in their position relative to the monochromator exit slit will lead to imprecise thickness measurements. For the monochromator used in this work, dispersion at the exit slit is about 7 nm/mm. A fiber misalignment of 12μm will result in a wavelength error of 0.1 nm which, in turn, causes a 5 nm error in gap thickness measurement. This section describes a method to measure the misalignment of each fiber and compensate the polychromatic reflectance measurements.

Since I wanted a measurement of the wavelength of light transmitted by each fiber, measuring the relative position of each fiber in the bundle was not the most direct method. The wavelength measurement was made directly. I used a low-pressure gas discharge lamp as a source of known wavelengths. Argon gas has several bright emission lines at visible and near-infrared wavelengths. Figure 6.17 shows part of the argon emission spectrum I detected using a silicon photodiode. First, I aligned the fiber bundle to the monochromator using the method described in Section 6.2.2. Next, I calibrated the monochromator using the output of fiber number 10, which I chose arbitrarily. To reflect light back into each gap sensor, I covered the front of each module with reflective mylar film. I then imaged the argon source onto the entrance slit of the monochromator and recorded the spectrum with the 24 gap sensors. The measurements were repeated 18 times. I wrote a small program to find each of the 14 argon emission lines and note the commanded monochromator wavelength at which the peak was recorded. I repeated this for each of the 18 spectra and averaged the results for each fiber.

Figure 6.18 contains plots of the outcome. The wavelength at which the peak

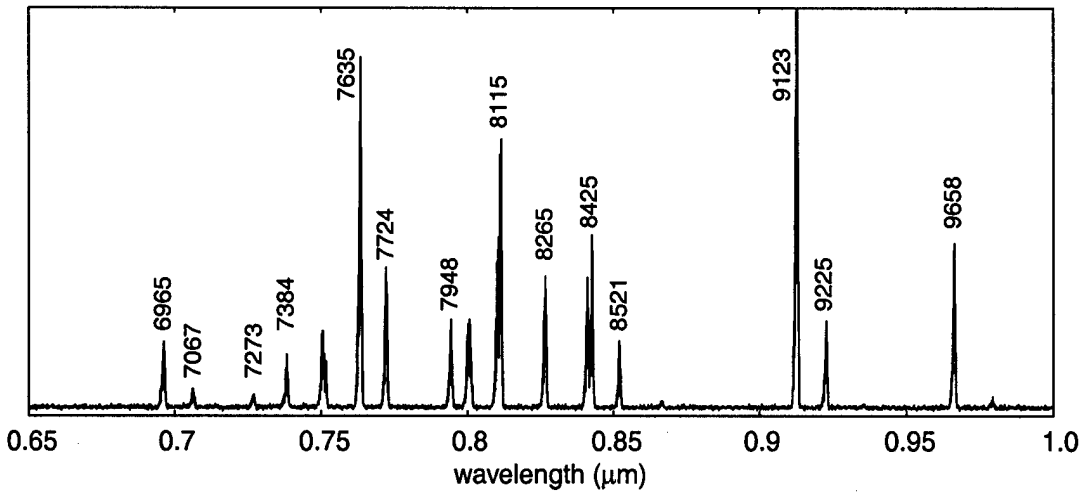

Figure 6.17 Argon emission spectrum. The wavelengths of the 14 lines I used for fiber bundle calibration are labeled in angstroms.

intensity occurred for a particular argon emission line is plotted for each fiber. There is one plot for each of the 14 emission lines; the horizontal axis labels the fiber number. The vertical axis is the commanded wavelength in angstroms; the range plotted is 2 nm. The horizontal dashed line shows the accepted wavelength for each emission line.[74] The slope of the rows of dots suggests the fiber bundle was rotated with respect to the exit slit. The deviation of the dots from a straight line represents the misalignment of each fiber. The rows of dots vary vertically with respect to the dashed lines. This indicates a cyclical error which is an artifact of the way the monochromator rotates its grating to change the output wavelength.[70] The microprocessor in the monochromator uses interpolation to determine which step corresponds to a particular wavelength. Furthermore, the stepper motor which drives the grating rotation has limited resolution.

These measurements give the wavelength error associated with each fiber due to its misalignment relative to the exit slit of the monochromator. We know the wavelength at which the monochromator is set when a particular fiber transmits the peak associated with a particular argon emission line. We can relate this commanded

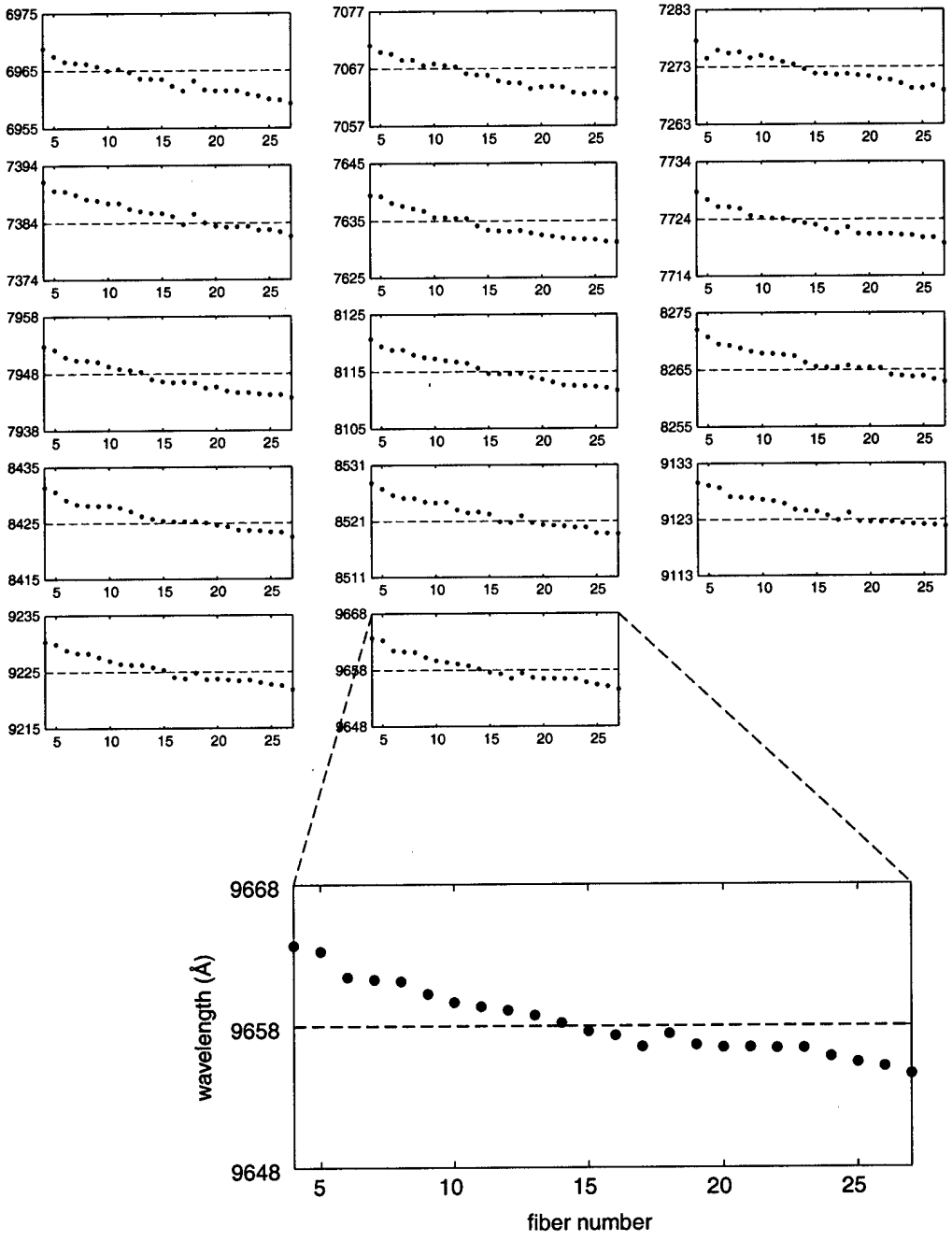

Figure 6.18 Data to calculate the actual wavelength transmitted by each fiber. The wavelength at which the peak intensity occurred for a particular argon emission line is plotted for each fiber. There is one plot for each of the 14 emission lines; the horizontal axis labels the fiber number. The dashed line shows the accepted wavelength for each emission line.

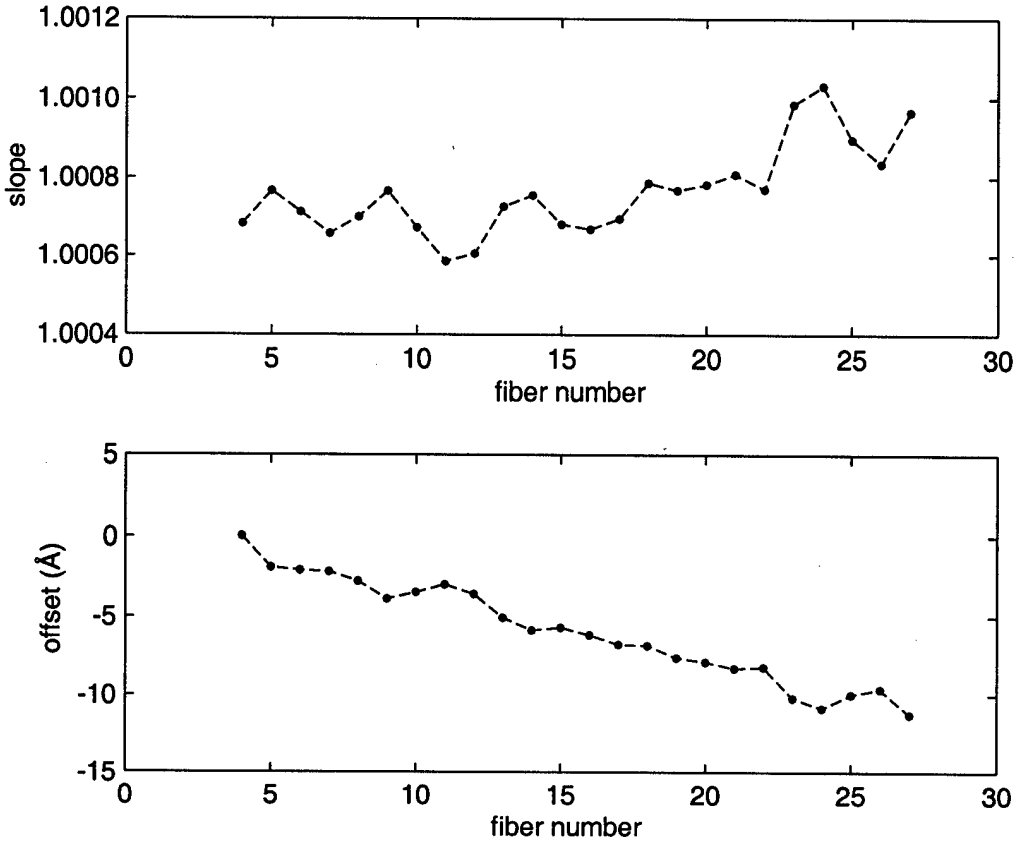

Figure 6.19 Coefficients for a linear fit of actual transmitted wavelength to commanded monochromator wavelength. The coefficients shown convert actual wavelengths λ to commanded wavelengths λ_c, that is, $\lambda_c = m\lambda + h$, where m is the slope and h is the offset. These parameters are used to correct the wavelength scale for the polychromatic reflectance fringes collected by each gap sensor.

wavelength to the actual wavelength by performing a least-squares fit for each fiber. This gives a function which can be used to correct the wavelength scale for the reflectance fringes that are collected by each gap sensor. The parameters for a linear fit to the data illustrated in Figure 6.18 are plotted in Figure 6.19. Once the wavelength scale for the reflectance fringes has been corrected, I use the actual wavelength at which each of the data points were collected in the model of the fringes. The modeled fringes are then used in the correlation algorithm to estimate the gap thickness. Figure 6.20 shows the results of applying this correction to measurements

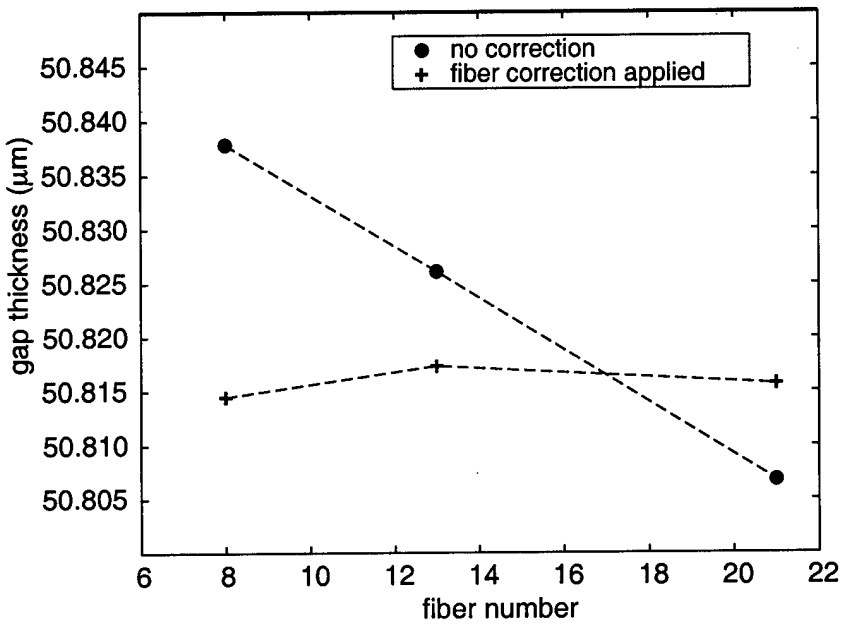

Figure 6.20 Thickness measurements of the epoxy reference standard using different gap sensors and fibers. Wavelength correction for fiber misalignment has been applied to produce the measurements noted by the crosses. The circles show the gap measurement with no correction for wavelength applied.

of the epoxy reference standard. Gap thickness was measured using three fibers: numbers 8, 13, and 21. The circles show the gap thickness calculated without the wavelength correction applied; the crosses show the gap thickness measured with the wavelength correction applied. The range of measurements went from 30 nm to less than 3 nm. This is within the error budget of 5 nm for inter-gap sensor accuracy when they are used for calibrating the capacitive sensors.[73]

When this method was used to correct measurements made with the 6 fiber bundle prototype, a curious pattern emerged as is shown in Figure 6.21. The measurements are plotted by fiber number, not the order in which the measurements were made. There is obviously some other effect that I have not corrected. For the type of monochromator used in this work, the lines of constant wavelength are actually slightly curved in the plane of the exit slit. For the same wavelength to

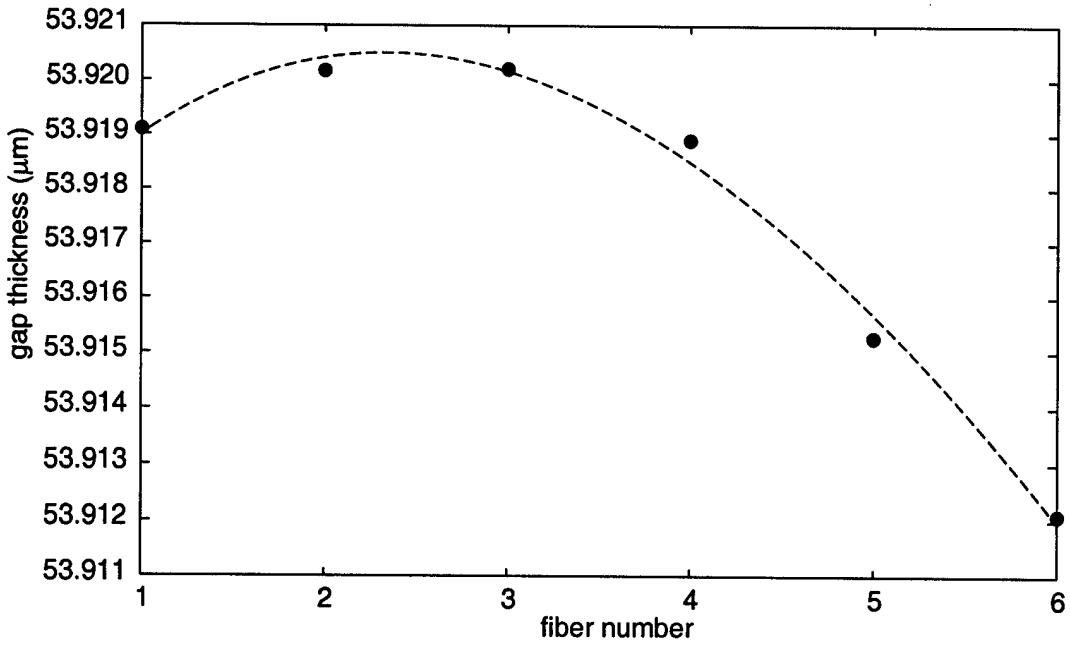

Figure 6.21 Thickness measurements of the glass micro-sphere reference standard using different gap sensors and fibers. The solid line is a parabola fit to the data.

appear at all parts of the exit slit, the exit slit would have to be curved, not straight. This effect should be measurable using the same methods described earlier in this section. Perhaps a parabolic fit should be used instead of a linear fit to correct the wavelength scale.

6.4 Use of Gap Sensors to Calibrate Capacitive Sensors

The fundamental purpose of the gap sensors is to measure the thickness of thin transparent films. The primary application for which they were developed is the calibration of the capacitive sensors used to control the force actuators on adaptive secondary mirrors. I planned to install the gap sensors on the adaptive secondary mirror and use them to calibrate the capacitive sensors. This work would have occurred on the adaptive optics test tower, where a phase shifting interferometer is available to assess the performance of the gap sensors. Because of delays in

development and fabrication, the secondary mirror was not ready to receive the gap sensors. An alternative plan was implemented; the gap sensors were installed on the 36 actuator prototype mirror, P36. Although P36 is much smaller and has fewer actuators, its structure is similar to that of the full-size secondary, which was described in Section 5.1. One significant difference is P36 is a concave sphere instead of a convex paraboloid; thus, its shape can be measured without an elaborate optical apparatus.

6.4.1 Gap Sensor Measurements on P36

P36 was built to test many new concepts for building adaptive secondaries. It was designed to use 6 gap sensors, but, because of a manufacturing snafu, it could accommodate only 3 gap sensors. This meant the gap sensors could only sense the rigid body motion of the mirror shell and not measure the shape of the shell. Since P36 is a concave mirror, its shape can be readily measured using a basic phase shifting interferometer. A method had been developed to calibrate the capacitive sensors by measuring small displacements of the mirror with a phase-shifting interferometer.[75] The plan was to calibrate the capacitive sensors using the small displacement method, using both gap sensor and interferometer measurements. These tests were especially important as they used the gap sensors in a setting virtually identical to that of the full-size secondary mirror.

The tests with P36 were conducted at the *Osservatorio Astrofisico di Arcetri* in Florence, Italy during October 2000. G. Brusa and A. Riccardi of Arcetri were instrumental in obtaining the results I present here. We installed three gap sensors on the adaptive mirror; Figure 6.22 shows one gap sensor mounted to the cooling plate. Using the gap sensors and the interferometer, we measured small displacements of the P36 mirror shell. The next section briefly explains the small displacement method of calibrating the capacitive sensors. Finally, I compare measurements of

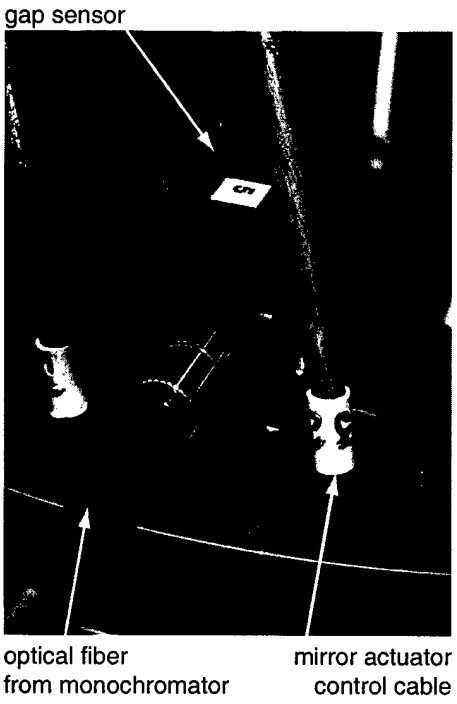

Figure 6.22 Gap sensor mounted to the cooling plate of P36.

mirror displacements made with the gap sensors and an interferometer.

6.4.2 Capacitive Position Sensor

Each electromagnetic actuator of the adaptive mirror has associated with it a capacitive position sensor. One plate of each capacitor is formed by an annular ring of metal film deposited on the reference surface around each actuator. The other plate, formed by a continuous metal coating applied to the back of the mirror shell, is common to all the capacitors. Each capacitor has a small electronic circuit which allows local closed-loop control of the actuator's position. This permits fast local control of the flexible mirror dynamics while the mirror is driven in closed-loop by the adaptive optics system, which uses the slower wavefront sensor. The capacitive sensors also permit control of the mirror figure without using the adaptive optics system, that is, without using the wavefront sensor.

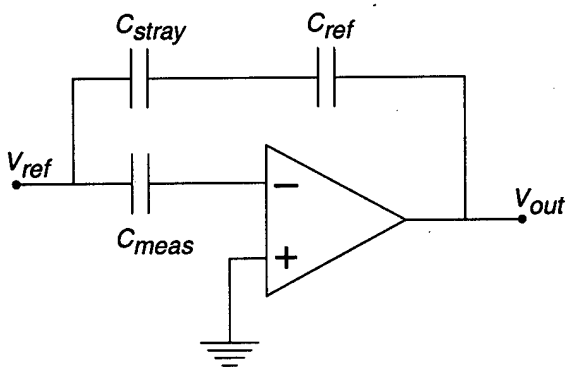

Figure 6.23 Simplified diagram of the capacitive position sensor electronics.

A simplified diagram of the capacitive sensor electronics is shown in Figure 6.23. A reference signal, with a 40 kHz modulation frequency, is applied to the circuit at V_{ref}.[75,76] This signal flows through the capacitive sensor C_{meas}, is amplified, and is presented at V_{out}. A separate path through the circuit board is represented by C_{stray}. The normalized output voltage, defined as $v \equiv V_{out}/V_{ref}$ is

$$v = \frac{g_0}{g} + c \tag{6.4}$$

where g_0 depends on the reference capacitance, g is the gap to be measured, and c is the ratio C_{stray}/C_{ref}. Specifically, g_0 and g are defined as

$$g_0 = \frac{\epsilon_0 S}{C_{ref}} \tag{6.5}$$

$$g = \frac{\epsilon_0 S}{C_{meas}} \tag{6.6}$$

where S is the area of the respective capacitor. In summary, the goal of calibrating the capacitive sensors is to determine g_0 and c, so that measurements of v will yield g. Actually, the small displacement calibration procedure seeks to measure the local slope $\partial v/\partial g$ at different normalized output voltages v. The two parameters of interest, g_0 and c are then found by a linear fit to the equation

$$v = \sqrt{g_0}\sqrt{-\frac{\partial v}{\partial g}} + c. \tag{6.7}$$

This allows relative displacements, which can be measured with the interferometer, to be used to find the parameters g_0 and c.

6.4.3 Comparison of Gap Sensor and Interferometer Measurements

We used the following procedure to measure the local slope $\partial v/\partial g$ and the normalized voltage v:[75]

1. Three actuators, separated by 120 degrees, are used in closed-loop to set the mirror in an isostatic position; interferometer, gap sensor, and voltage measurements are then taken.
2. One actuator is displaced slightly, while the other two remain fixed, to introduce a tilt; the interferometer, gap sensor, and voltage measurements are repeated.
3. The first two steps are repeated for the other two actuators.
4. The first three steps are repeated for several values of v, that is, gap thickness.

The data collection process took a few hours to complete the first three steps. Because of unforseen hardware problems, we could not complete step 4 of the calibration process.[¶] We used the phase-shifting interferometer measurements directly to determine the local displacement at each actuator. Since there were only three gap sensors on P36, only the mirror's rigid-body motion could be measured. The displacement at each actuator was inferred from the mirror tilt. The fringes measured by the gap sensors were processed using only the Fourier transform method described in Section 5.3.2. Furthermore, since we were interested in measuring only relative displacements, not absolute gap thickness, the correction for optical fiber misalignment was not applied to the polychromatic fringes.

The local displacement for each actuator is plotted in Figure 6.24 (a) for a nominal gap thickness of 40 μm. Interferometer and gap sensor measurements are both

[¶]The thin mirror shell was cracked by accident.

illustrated. Unfortunately, when we tilted the thin mirror, it flexed. This introduced some low-order distortion of the mirror surface, dominated by astigmatism. The departure from pure rigid-body motion, as measured by the interferometer, was used to correct the gap sensor measurements. The corrected gap sensor measurements are shown in Figure 6.24 (b). On average, the interferometer measurements of displacement agree with the corrected gap sensor measurements to better than 2 percent of the displacement. With more gap sensors, the flexure of the mirror could be measured directly without the need for interferometer measurements. Calibration of the capacitive sensors with the gap sensors alone has the advantage of not requiring time-consuming tilting of the mirror. Absolute gap thickness measurements can be used directly to perform a fit to equation (6.4).

(a)

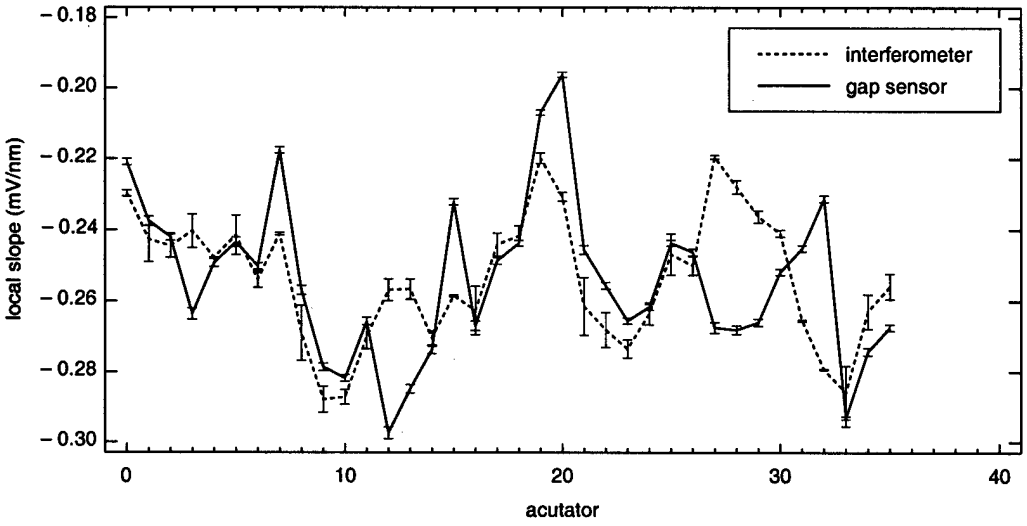

(b)

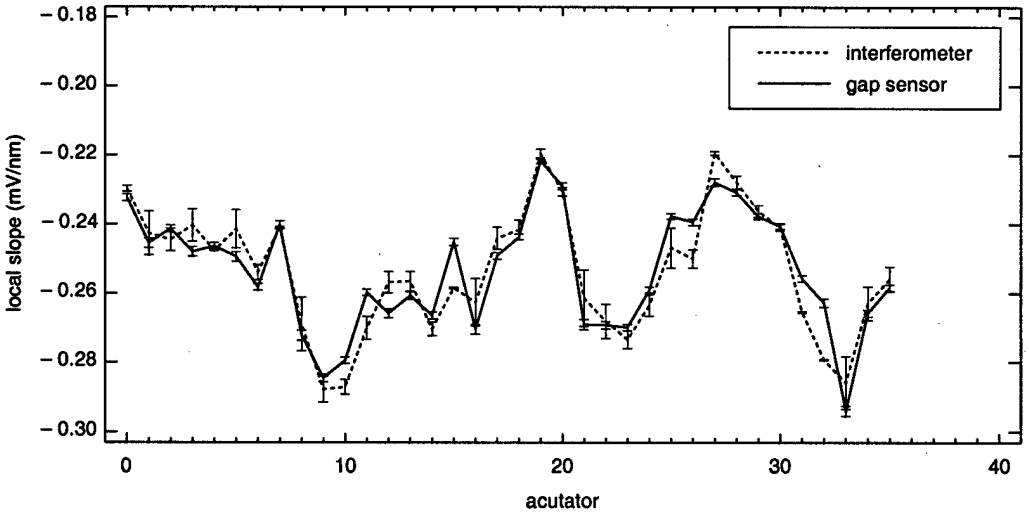

Figure 6.24 Local displacement for each P36 actuator as measured using an interferometer and three gap sensors. Figure (a) shows the uncorrected gap sensor measurements; Figure (b) shows the gap sensor measurements corrected for the flexure of the mirror.

APPENDIX A

ALIGNING THE SHIMULATOR

A.1 Introduction

This appendix presents a concise description of the alignment procedure for the apparatus used to test the 6.5 m MMT adaptive optics system: the shimulator. Aligning the shimulator is a formidable task; there are more than 20 optical elements, ranging in diameter from 5 μm to 700 mm, which must be aligned to precise tolerances over a 10 m optical path. Careful alignment is necessary to the operation of the adaptive optics system. Of course, an adaptive system should be able to compensate for aberrations caused by minor misalignments. Correct mapping of the pupil through the shimulator to the wavefront sensor, however, is critical. Misalignments which affect this mapping will seriously degrade the performance of the system. Special care should be taken to minimize errors which affect the mapping of the adaptive secondary to the wavefront sensor.

Before describing the alignment procedure, I first state a few important assumptions. The reader should be familiar with basic procedures for handling delicate optical elements. Many of the optics, the adaptive mirror and computer-generated hologram (CGH) in particular, are easily damaged and are difficult to replace. The

reader should also be proficient in using standard optical metrology instruments: the auto-collimating alignment telescope, the theodolite, and the phase-shifting interferometer. Also, a basic practical understanding of mechanical and electronic principles will prove to be indispensable.

The reader should understand the basic design of the shimulator and the function of each of its elements. Chapter 3 gives an overview of the shimulator; the references should provide a more detailed understanding. In particular, the paper by R. Sarlot and J. Burge presents the design of the shimulator[39], while the paper by M. Lloyd-Hart, et al., explains the development of the major shimulator components.[77] Much of the procedure presented here evolved from an alignment procedure developed by R. Sarlot[78] and C. Bresloff[79]; it was extensively modified and adapted by H. Martin, R. Allen, and me. The following list provides a rough outline of the various phases of the alignment process.

1. Install the secondary mirror and the large lenses in the shimulator tower; center them and set their relative spacings.
2. Adjust the tilt of the two large fold mirrors so the mechanical axis of the top-box is roughly aligned to the secondary.
3. Use an alignment telescope to locate and adjust the optical axis of the large lenses.
4. Use the alignment telescope to place the smaller doublet and the secondary mirror on the optical axis.
5. Assemble and align the source fiber and computer-generated hologram on the source table; align the source table to the optical axis using the special alignment marks generated by the hologram.
6. Use a theodolite to measure and set the distance between the large lenses and the smaller doublet.

elements	distance
M2–L1	25.7
L1–L2	25.0
L2–L3	8075.6
L4–CGH	562.9

Table A.1 Nominal spacings between optical surfaces in the shimulator. Distances are in millimeters. The distance from the CGH substrate to the diverging lens is about 292 mm, depending on the thickness of the acrylic compensator plates.

A.2 Shimulator Alignment Procedure

In the following sections, I explain each step of the list above. Nearly all of the procedures presented here will proceed more quickly with two people, one to adjust while the other directs the adjustments using some alignment aid. I assume none of the optical elements have been installed until they are mentioned in the procedure. Where appropriate, I present a brief description of each optical mount. The adjustable degrees of freedom, which are used to position each optical element, are listed in Table 3.4. The nominal spacings between the elements are listed in Table A.1. The distances in the table are taken from a design which was optimized to account for the as-built specifications of the two doublets; hence, they depart slightly from the nominal design.

A.2.1 Install Secondary Mirror and Large Lenses

The first step is relatively straightforward and, although great care is required in handling the large optics, special alignment techniques are not required. The secondary mirror is mounted to a hexapod which controls its position with five degrees of freedom. The two large 700 mm diameter lenses, L1 and L2, are collectively called the large doublet. L1 is the plano-convex lens which is mounted closest to

the secondary mirror; L2 is biconvex and has been scribed to mark its optical axis. These lenses have been installed in a lens cell which maintains their mutual separation and alignment.[79] The lens cell is suspended below the secondary mirror from three threaded rods. The rods are somewhat flexible, thus, adjustable actuators limit the lateral movement of the lens cell. Although the position of the large doublet is adjustable, because of the coarseness of its adjustments, the rest of the optical system is aligned to it. Position the lens cell so that it is level and roughly centered on the secondary mirror.

A.2.2 Adjust Tilt of Two Fold Mirrors

In this step, the tilts of the two fold flats are roughly adjusted, the alignment telescope is installed, and the fold flats are carefully tilted to locate the optical axis of the large doublet in the alignment telescope. First, install two sets of cross-hairs to locate the center of the top-box floor and the center of the mount platform for the smaller doublet, as sketched in Figure A.1. Next, attach a small plumb bob to the cross-hair on the smaller doublet platform. Adjust the position of the platform to align it with the cross-hair at the center of the top-box floor. This defines a vertical mechanical axis perpendicular to the surface of the top-box floor, that is, if the top-box floor is level. Remove the plumb bob. From well below the lower cross-hair, sight along this axis and carefully place a small paper marker on the small fold flat, F2. A small circle punched from a brightly-colored Post-It note works well. Use this temporary marker to adjust the tilts of the two fold flats as you sight along the cross-hairs from below. Tilt the flats to bring the center of the large doublet roughly in line with the vertical mechanical axis of the top-box.

Place the alignment telescope in its v-block mount and attach the mount to a translation stage. The translation axis of the stage should be perpendicular to the longitudinal axis of the alignment telescope. The v-block mount has controls to

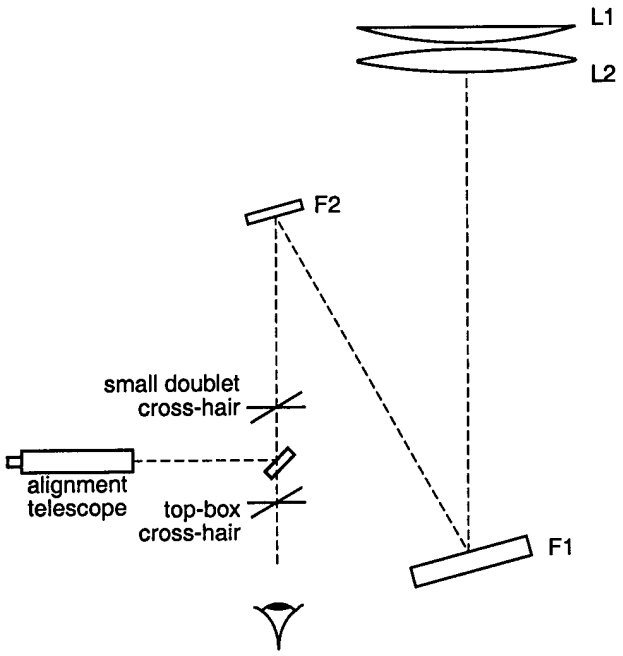

Figure A.1 Sketch showing placement of cross-hairs and alignment telescope. The drawing is not to scale.

adjust the tilt of the telescope. Mount the translation stage and alignment telescope at the outer edge of the top-box floor with the telescope pointed towards the center of the top-box. Install a 3-inch diameter fold mirror, tilted at 45 degrees, between the two cross-hairs as shown in Figure A.1. This fold mirror should be placed in a gimbal mount which is adjustable in tilt and is mounted to a vertical translation stage. It folds the optical axis into the alignment telescope. You may place the alignment telescope and fold mirror on an optical table below the top-box, if an optical table is available.

Focus the telescope on the small doublet cross-hair. Adjust the translation of the small fold mirror and the translation of the alignment telescope to center the cross-hair in the telescope. Then focus on L2 and adjust the tilt of the fold mirror to align the telescope to the scribe on L2. Re-focus on the cross-hair to check if it is still centered. You may have to iterate between the cross-hair and the scribe on

L2 to get the telescope aligned with the mechanical axis. This alignment does not have to be perfect.

The next adjustment is to tilt the large fold flats to align the telescope to the optical axis of the large doublet. First, carefully place a 3-inch diameter flat mirror face down on L1. Use this mirror with the alignment telescope in auto-reflection mode to tilt F2 to adjust the *angle* to the optical axis. Then tilt F1 with the alignment telescope focused on the L2 scribe mark to adjust the *translation* to the optical axis. Again, you will alternate between adjusting the angle to the optical axis using F2 and adjusting the translation to the optical axis using F1. Once this step is complete, you have determined the optical axis of the large doublet with the alignment telescope.

A.2.3 Install and Align Smaller Doublet

The two lenses of the smaller doublet, L3 and L4, are held in a lens cell which has three actuators to control its tilt. The ends of the actuators fit into three v-grooves fixed to the mount platform; this kinematically positions the doublet. The platform can be moved in three axes with micrometer-actuated stages. L3 has two concentric scribe marks on its upper surface to indicate its optical axis. Place the smaller doublet lens cell on the platform with the actuators in the v-grooves. Focus the alignment telescope on the upper surface of L3. Center the L3 scribe mark in the alignment telescope by translating the platform laterally. Then, refocus the telescope to see the auto-reflection image from the smaller doublet. You may cover the doublet with some light-weight dark cloth to help see the auto-reflection image. Adjust the tilt of the doublet to align its optical axis to that of the telescope and the large doublet. After the smaller doublet is aligned, carefully remove it from the platform in preparation for aligning the secondary mirror.

A.2.4 Align Secondary Mirror to Large Lenses

The next step is to align the secondary mirror to the optical axis defined by the alignment telescope. First, set the distance between the secondary mirror and L1, then adjust the mirror translation and tilt. The procedure is similar to aligning the smaller doublet. Focus on the center of the mirror and adjust the mirror translation; focus on the auto-reflection target and adjust the mirror tilt. Make adjustments to the mirror position by manipulating the hexapod. B. Martin has crafted a spreadsheet which calculates the proper hexapod adjustments to yield a particular motion of the secondary mirror.[17]

A.2.5 Install and Align Source and CGH

In addition to correcting spherical aberration in the shimulator, the CGH projects five sets of patterns to aid in alignment. Consult the R. Sarlot memorandum for a complete description of these patterns.[80] To prevent confusion between the patterns, make a mask from stiff paper to block all but the relevant pattern for a particular alignment task. First, assemble the source table including the four acrylic compensator plates. Make sure you have the correct CGH for the secondary mirror you are testing.

Next, set the approximate distance between the CGH and the diverging lens. Attach the optical source fiber and observe the reflected alignment pattern. Center this pattern on the diverging lens by tilting the CGH. Then, use the mask to select the correct pattern for collimation. Set the distance between the diverging lens and the CGH by making the collimation pattern marks 69.13 mm apart at the outer edges. Do this over a long path to increase accuracy. Note the setting of the micrometer. Adjust the transverse position of the diverging lens such that when the lens is translated longitudinally relative to the CGH, the collimation pattern does not translate. Once the transverse position is set, readjust the tilt of the CGH as

before. Reset the micrometer to the proper longitudinal position and re-check the collimation.

Finally, install the source table in the top-box and align the source table axis to the optical axis defined by the scribe marks on the two doublets. First, install the beamsplitters, B1 and B2. Use the mask to select the appropriate CGH alignment pattern. Adjust the transverse position of the table while observing the alignment marks on the smaller doublet. Use a 75 × magnifier on top of L3 to precisely adjust the source table. Then, adjust the tilt of the beamsplitter while observing the alignment marks on the large doublet. Alternate between these two adjustments until the optical axes are aligned.

The spacing between the CGH and the small doublet can be set by adjusting the longitudinal position of the source table so the appropriate alignment pattern converges at the lower surface of L4. This spacing can also be measured by using an inside micrometer. Place the long face of a large right angle prism on the beamsplitter so the short faces are perpendicular to the beam. Then measure the distance to the short faces directly using the micrometer.

The spacing between the small doublet and the large doublet is more difficult to measure and adjust. A theodolite measures the distance to an object by measuring the angle subtended by an known length on the object. Mount the theodolite in the top-box and measure the distance to L2 by measuring the angle between two rulers which are mounted to the lens cell. You must measure directly the distance from the rulers to L2 in addition to the distances from the theodolite to the CGH and from the CGH to L4. The thickness of the doublet is 48 mm.

The shimulator should now be aligned well enough to see fringes on the interferometer. Install interferometer in the top-box. Adjust the position of the pupil imaging lens and video camera to get a sharp image of the secondary mirror. Install

a mask near the $f/15$ focus to eliminate the unwanted orders of the CGH. Install and adjust the position of the reference source to get fringes in the interferogram. Minimize the density of fringes by adjusting the translation of the reference fiber and adjusting the secondary mirror tilt. The next appendix gives a short description of how to align the adaptive optics system: the top-box and wavefront sensor.

Appendix B

Aligning the Top Box and Wavefront Sensor

B.1 Overview

The alignment of the top-box and wavefront sensor, while less difficult than the alignment of the shimulator, is by no means less critical to the proper operation of the adaptive optics system. Just as with the shimulator, correct mapping of the pupil to the wavefront sensor is important. Misalignments which affect this mapping will seriously degrade the performance of the adaptive optics system. The same caveats made in Appendix A, regarding the skill and knowledge of the reader, apply when aligning the wavefront sensor. The basic design of the top-box and wavefront sensor is described in Chapter 2. The wavefront sensor for the 6.5 m MMT is unusual in that the lenslet array is bonded directly to the chip carrier of the detector array. This fortunate design detail makes the task of aligning the wavefront sensor much easier.

B.2 Alignment Procedure

The top-box alignment procedure is quite simple. As described in Section 2.2, the lateral positions of all the optical elements are precisely fixed. The process is uncomplicated; the only adjustments to be made are to the tilt of each mirror. Starting with the first fold mirror before the $f/15$ focus, tilt each mirror in turn, so the light strikes the center of the next mirror. To locate the center of the elements, custom masks have been made for each mirror cell with small holes in the center.

Alignment of the wavefront sensor is more difficult. The top-box is mounted to the telescope instrument derotator. Since the relationship between the adaptive secondary mirror and the wavefront sensor must remain constant, the wavefront sensor is rotated to counteract the motion of the instrument derotator. This rotation must not affect the alignment of the wavefront sensor to the top-box. Thus, the optical axis of the wavefront sensor must be made to coincide with the rotation axis of its mount. Two other alignments must be made: the pupil must be imaged onto the correct lenslets and the nominal wavefront must be free of tilt at the lenslet array.

First, rotate the wavefront sensor and note the motion of the pupil. The motion of the pupil can be observed as different subapertures are illuminated as the wavefront sensor is rotated. If the pupil orbits about some point, OAP1 and OAP2 should be tilted, in opposite directions by the same amount, to move the pupil to the center of its orbit. This aligns the pupil to the rotational axis. To align the rotational axis to the optical axis, which is defined as the center of the detector array, translate the wavefront sensor within its rotational stage, until the center of the pupil orbit coincides with the center of the detector array.

Tilt in the wavefront is discerned by observing the motion of individual spots as the wavefront sensor is rotated. Tilt is removed from the wavefront by simply

tilting the pupil steering mirror the appropriate amount while observing the spots with the detector array. These adjustments to the pupil location and wavefront tilt are iterated until the misalignment is eliminated. Finally, test the quality of the top-box alignment by placing an optical fiber a the $f/15$ focus to act as a source of nearly perfect wavefronts. The transmitted wavefront is measured by the wavefront sensor.

REFERENCES

[1] J. W. Goodman, *Statistical Optics*, Wiley, New York, 1985.

[2] M. C. Roggemann and B. Welsh, *Imaging Through Turbulence*, CRC Press, New York, 1996.

[3] J. M. Beckers, "Adaptive optics for astronomy: principles, performance, and applications," *Annu. Rev. Astron. Astrophys.* **31**, pp. 13–62, 1993.

[4] J. R. P. Angel and N. Woolf, "The Large Binocular Telescope: a unique scientific and technology precursor to Planet Finder," in *Planets Beyond the Solar System and the Next Generation of Space Missions*, D. Soderblom, ed., *Astronomical Society of the Pacific Conference Series* **119**, pp. 207–222, 1997.

[5] P. M. Hinz, J. R. P. Angel, W. F. Hoffman, D. W. M. Jr., P. C. McGuire, M. Cheselka, J. L. Hora, and N. J. Woolf, "Imaging circumstellar environments with a nulling interferometer," *Nature* **395**, pp. 251–253, 1998.

[6] H. W. Babcock, "The possibility of compensating astronomical seeing," *Pub. Astr. Soc. Pac.* **65**, pp. 229–236, 1953.

[7] D. L. Fried, "Statistics of a geometric representation of wavefront distortion," *J. Opt. Soc. Am.* **55**, pp. 1427–1435, 1965.

[8] P. C. McGuire, M. P. Langlois, M. Lloyd-Hart, T. A. Rhoadarmer, and J. R. P. Angel, "Measurement of atmospheric turbulence with a Shack-Hartman wavefront sensor at the new MMT's prime focus," in *Advanced Technology Optical/IR Telescopes VI*, P. Wizinowich, ed., *SPIE Conference on Adaptive Optics Systems and Technology* **4007**, 2000.

[9] D. P. Greenwood, "Bandwidth specification for adaptive optics systems," *J. Opt. Soc. Am.* **67**, pp. 390–393, 1977.

[10] R. V. Shack and B. C. Platt, "Production and use of a lenticular Hartmann screen," *J. Opt. Soc. Am.* **61**, p. 656, 1971.

[11] R. Foy and A. Labeyrie, "Feasibility of adaptive telescopes with laser probe," *Astr. Astrophys.* **152**, pp. 129–131, 1985.

[12] R. Q. Fugate, B. L. Ellerbroek, C. H. Higgins, M. P. Jelonek, W. J. Lange, A. C. Slavin, W. J. Wild, D. M. Winker, J. M. Wynia, J. M. Spinhirne, B. R. Boeke, R. E. Ruane, J. F. Moroney, M. D. Oliker, D. W. Swindle, and R. A. Cleis, "Two generations of laser guide star adaptive optics experiments at the Starfire Optical Range," *J. Opt. Soc. Am. A* **11**, pp. 310–324, 1994.

[13] D. P. Greenwood and C. A. Primmerman, "Adaptive optics research at Lincoln Laboratory," *MIT Lincoln Laboratory Journal* **5**, pp. 3–24, 1992.

[14] H. M. Martin and D. S. Anderson, "Techniques for optical fabrication of a 2-mm-thick adaptive secondary mirror," in *Adaptive Optics*, M. Cullum, ed., *ESO Conf. Proc.* **54**, (European Southern Observatory, Garching, Germany), 1995.

[15] H. M. Martin, J. H. Burge, C. D. Vecchio, L. R. Dettmann, S. M. Miller, B. Smith, and F. Wildi, "Optical fabrication of the MMT adaptive secondary mirror," *SPIE Conference on Adaptive Optical Systems Technology* **4007**, (Munich), 2000.

[16] M. Lloyd-Hart, "Thermal performance enhancement of adaptive optics by use of a deformable secondary mirror," *Accepted by Publications of the Astronomical Society of the Pacific* , 2000.

[17] H. M. Martin. Steward Observatory Mirror Laboratory, University of Arizona, private communication.

[18] M. Lloyd-Hart, R. Angel, D. G. Sandler, T. K. Barrett, P. C. McGuire, T. A. Rhoadarmer, D. G. Bruns, S. M. Miller, D. W. McCarthy, and M. Cheselka, "Infrared adaptive optics system for the 6.5 m MMT: system status and prototype results," in *Adaptive Optical System Technologies*, D. Bonaccini and R. K. Tyson, eds., *Proc. SPIE* **3353**, pp. 82–93, 1998.

[19] J. C. Shelton, "The 6.5 m MMT adaptive optics top box." Steward Observatory Technical Memorandum, October 1997.

[20] G. Z. Angeli, B. C. Fitz-Patrick, and M. Lloyd-Hart, "Design and realization of ancillary control loops for the MMT adaptive optics system," in *SPIE Conference on Telescope Structures, Enclosures, Controls, Assembly/Integration/Validation, and Commissioning*, T. A. Sebring and T. Andersen, eds., *Proc. SPIE* **4004**, (Munich), 2000.

[21] W. J. Smith, *Modern Optical Engineering*, McGraw Hill, Boston, 2nd ed., 1990.

[22] D. Fabricant, B. McLeod, and S. West, "Optical specifications for the MMT conversion, version 7." http://cfa-www.harvard.edu/~bmcleod/mmt_conv7.ps, December 1999.

[23] A. Beach, "Test Report Nos. 301026 and 301027." Optical Surfaces Ltd, Kenley, Surrey, England, April 1999. Job No. 81211.

[24] M. Born and E. Wolf, *Principles of Optics*, Cambridge University Press, Cambridge, 6th ed., 1980.

[25] M. Lloyd-Hart, "Expected system performance." Internal Technical Review of the 6.5 m Adaptive Optics System, June 1998. Center for Astronomical Adaptive Optics, Steward Observatory, University of Arizona.

[26] R. J. Sarlot, "MMT AO top box—optical requirements." Steward Observatory Technical Memorandum, August 1998.

[27] A. Ghedina and R. Ragazzoni, "Optimum configurations for two off-axis parabolae used to make an optical relay," *J. Mod. Opt.* **44**, pp. 1259–1268, 1997.

[28] T. A. Rhoadarmer, *Construction and Testing of Components for the 6.5 m MMT Adaptive Optics System.* PhD thesis, University of Arizona, Optical Sciences Center, 1999.

[29] Adaptive Optics Associates, Cambridge, Mass., "Epoxy on glass lens array." http://www.aoainc.com, August 2000.

[30] M. A. Kenworthy. Center for Astronomical Adaptive Optics, Steward Observatory, University of Arizona, private communication.

[31] T. Roberts and J. Sasian, "A simple method of measuring positive lens focal length." unpublished work, October 1998.

[32] R. V. Shack, "Class notes: Introduction to aberrations." Fred A. Hopf Library, Optical Sciences Center, University of Arizona, January 1999.

[33] M. Lloyd-Hart, G. Angeli, R. Angel, P. McGuire, T. A. Rhoadarmer, and S. Miller, "Infrared adaptive optics system for the 6.5-m MMT: system status," in *Astronomy with Adaptive Optics – Present Results and Future Programs*, D. Bonaccini, ed., *ESO Conf. Proc.* **56**, pp. 585–592, (European Southern Observatory, Garching, Germany), 1999.

[34] A. Offner and D. Malacara, *Optical Shop Testing*, ch. Null Tests Using Compensators, pp. 427–454. Wiley Series in Pure and Applied Optics, John Wiley & Sons, New York, 2nd ed., 1992.

[35] J. H. Hindle, "A new test for cassegrainian and gregorian secondary mirrors," *Mon. Not. R. Astron. Soc.* **91**, p. 592, 1931.

[36] F. A. Simpson, B. H. Oland, and J. Meckel, "Testing convex aspheric lens surfaces with a modified hindle arrangement," *Opt. Eng.* **13**, p. 101, 1974.

[37] R. E. Parks and L. Z. Shao, "Testing large hyperbolic secondary mirrors," *Opt. Eng.* **27**, pp. 1057–1062, 1988.

[38] Kingslake, *Lens Design Fundamentals*, Academic Press, New York, 1978.

[39] R. J. Sarlot and J. H. Burge, "Optical system for closed-loop testing of adaptive optic convex mirror," in *Novel Optical Systems and Large-Aperture Imaging*, K. D. Bell, M. K. Powers, and J. M. Sasian, eds., *Proc. SPIE* **3430**, pp. 126–135, 1998.

[40] J. H. Burge, "A null test for null correctors: Error analysis," in *Quality and Reliability for Optical Systems*, J. W. Bilbro and R. E. Parks, eds., *Proc. SPIE* **1993**, pp. 86–97, 1993.

[41] J. H. Burge, "Measurement of large convex aspheres," in *Optical Telescopes of Today and Tomorrow*, A. L. Ardeberg, ed., *Proc. SPIE* **2871**, pp. 362–373, 1997.

[42] R. E. Fischer and K. L. Mason, "Spherical aberration–some fascinating observations," in *Recent Trends in Optical Systems Design, Proc. SPIE* **766**, p. 53, 1987.

[43] K. Creath and J. C. Wyant, *Optical Shop Testing*, ch. Holographic and Speckle Tests, pp. 599–651. Wiley Series in Pure and Applied Optics, John Wiley & Sons, New York, 2nd ed., 1992.

[44] B. L. Stamper, "Shimmulator interferometer laser source for the Multiple Mirror Telescope upgrade." Steward Observatory Technical Memorandum, June 1999.

[45] J. E. Greivenkamp and J. H. Bruning, *Optical Shop Testing*, ch. Phase Shifting Interferometry, pp. 501–598. Wiley Series in Pure and Applied Optics, John Wiley & Sons, New York, 2nd ed., 1992.

[46] C. Zhao, "Description of the AO interferometer." Steward Observatory Technical Memorandum, May 1999.

[47] P. Hariharan, B. F. Oreb, and T. Eiju, "Digital phase-shifting interferometry: A simple error-compensating phase calculation algorithm," *Appl. Opt.* **26**, p. 2504, 1987.

[48] R. J. Sarlot, "Shimulator tolerancing analysis." Steward Observatory Technical Memorandum, July 2000.

[49] R. G. Allen. Steward Observatory Mirror Laboratory, University of Arizona, private communication.

[50] J. R. P. Angel. Center for Astronomical Adaptive Optics, Steward Observatory, University of Arizona, private communication.

[51] W. H. Southwell, "Wave-front estimation from wave-front slope measurements," *J. Opt. Soc. Am. A* **70**(8), pp. 998–1006, 1980.

[52] J. W. Goodman, *Introduction to Fourier Optics*, McGraw-Hill, New York, 2nd ed., 1996.

[53] M. C. Roggemann and T. J. Schulz, "Algorithm to increase the largest aberration that can be reconstructed from Hartmann sensor measurements," *Appl. Opt.* **37**, pp. 4321–4329, 1998.

[54] Marconi Applied Technologies, Chelmsford, Essex, England, "CCD39-01 Back Illuminated High Performance CCD Sensor." http://www.marconitech.com, January 2000.

[55] H. A. Macleod, *Thin Film Optical Filters*, McGraw-Hill Publishing Company, New York, 2nd ed., 1989.

[56] J. W. Hardy, *Adaptive Optics for Astronomical Telescopes*, Oxford University Press, Oxford, 1998.

[57] D. L. Fried, "Least-squares fitting a wave-front distortion estimate to an array of phase difference measurements," *J. Opt. Soc. Am. A* **67**, pp. 370–375, 1977.

[58] R. H. Hudgin, "Wave-front reconstruction for compensated imaging," *J. Opt. Soc. Am.* **67**, pp. 375–378, 1977.

[59] R. J. Noll, "Zernike ploynomials and atmospheric turbulence," *J. Opt. Soc. Am.* **66**, pp. 207–211, 1976.

[60] H. H. Barrett and K. J. Myers, *Foundations of Images Science*, whoknows, whoknows, 1999.

[61] J. D. Gaskill, *Linear Systems, Fourier Transforms, and Optics*, J. Wiley and Sons, New York, 1978.

[62] G. Brusa, A. Riccardi, S. Ragland, S. Esposito, C. D. Vecchio, L. Fini, P. Stefanini, V. Biliotti, P. Ranfagni, P. Salinari, D. Gallieni, R. Biasi, P. Mantegazza, G. Sciocco, G. Noviello, and S. Invernizzi, "Adaptive secondary P30 prototype: laboratory results," in *Adaptive Optical System Technologies*, D. Bonaccini and R. K. Tyson, eds., *Proc. SPIE* **3353**, pp. 764–775, 1998.

[63] V. Biliotti, R. Biasi, G. Brusa, D. Gallieni, R. Spairani, and R. Aiello, "High accuracy capacitive displacement transducer for the position local control loops at the adaptive secondary," in *Adaptive Optics*, M. Cullum, ed., *ESO Conf. Proc.* **54**, pp. 213–219, (European Southern Observatory, Garching, Germany), 1995.

[64] C. Fabry and A. Perot, "Théorie et applications d'une nouvelle méthode de spectroscopie interférentielle," *Ann. Chim. Phys.* **16**, pp. 115–144, 1899.

[65] W. H. Press, S. A. Teukolsky, W. T. Vettering, and B. P. Flannery, *Numerical Recipes in C: The Art of Scientific Computing*, Cambridge University Press, Cambridge, 2nd ed., 1992.

[66] A. Vašíček, *Optics of Thin Films*, North-Holland Publishing Company, Amsterdam, 1960.

[67] O. S. Heavens, *Optical Properties of Thin Solid Films*, Dover, New York, 1965.

[68] O. S. Heavens, *Optical Properties of Thin Solid Films*, Butterworth Scientific Publications, London, 1955.

[69] M. Hartl, I. Křupka, and M. Liška, "Differential colorimetry: tool for evaluation of chromatic interference patterns," *Opt. Eng.* **36**, pp. 2384–2391, 1997.

[70] T. M. Niemczyk and G. W. Gobeli, "Characteristics of a direct grating drive," *Appl. Spectroscopy* **42(5)**, pp. 792–796, 1988.

[71] M. A. Kenworthy, *Development of New Techniques for Integral Field Spectroscopy in Astronomy.* PhD thesis, Cambridge University, Institute of Astronomy, 1998.

[72] J. H. Burge. Center for Astronomical Adaptive Optics, Steward Observatory, University of Arizona, private communication.

[73] F. Wildi, "Calibration plan and procedures for the WFS, DM, and AO system." Center for Astronomical Adaptive Optics, Steward Observatory, University of Arizona, internal technical document, August 1999.

[74] R. C. Weast, ed., *CRC Handbook of Chemistry and Physics*, CRC Press, Boca Raton, Florida, 66th ed., 1986.

[75] G. Brusa. Osservatorio Astrofisico di Arcetri, Florence, Italy, private communication.

[76] A. Riccardi. Osservatorio Astrofisico di Arcetri, Florence, Italy, private communication.

[77] M. Lloyd-Hart, F. Wildi, H. Martin, P. McGuire, M. Kenworthy, R. Johnson, B. Fitz-Patrick, G. Angeli, S. Miller, and R. Angel, "Adaptive optics for the 6.5 m MMT," *SPIE Conference on Adaptive Optical Systems Technology* **4007**, (Munich), 2000.

[78] R. J. Sarlot, "Shimulator optical alignment procedure." Steward Observatory Technical Memorandum, March 1998.

[79] C. Bresloff, "Shimulator optical alignment procedure." Steward Observatory Technical Memorandum, May 2000.

[80] R. J. Sarlot, "CGH design patterns for shimulator test." Steward Observatory Technical Memorandum, June 2000.